BEATS

Workpackage 4

Beamline Technical Design and Instrumentation Procurement

BEATS Technical Design Report

D 4.1

August 2020

Funded by the EU's H2020 framework programme under grant agreement n°822535

PROJECT DETAILS

PROJECT ACRONYM
BEATS

PROJECT TITLE
BEAmline for Tomography at SESAME

GRANT AGREEMENT NO:
822535

THEME

START DATE
01/01/2019

DELIVERABLE DETAILS

WORK PACKAGE
04

EXPECTED *DATE*
31/08/2020

WORK PACKAGE TITLE
Beamline Technical Design and instrumentation procurement

DELIVERABLE TITLE
BEATS Technical design Report

WORK PACKAGE LEADER
ESRF

DELIVERABLE DESCRIPTION
Report

DELIVERABLE ID
D4.1

PERSON RESPONSIBLE FOR THE DELIVERABLE
Gianluca Iori

NATURE

☒ R - Report ☐ P - Prototype ☐ D - Demonstrator ☐ O - Other

DISSEMINATION LEVEL

☒ P - Public
☐ PP - Restricted to other programme participants & EC:
☐ RE - Restricted to a group
☐ CO - Confidential, only for members of the consortium

REPORT DETAILS

VERSION
1.0

DATE
31/08/2020

NUMBER OF PAGES
145

DELIVERABLE REPORT AUTHOR(S)
G. Iori et al.

FOR MORE INFO PLEASE CONTACT
gianluca.iori@sesame.org.jo

STATUS

☐ Template ☐ Draft
☒ Final ☒ Released to the EC

Contents

1 Introduction

The overall objective of the project Beamline for Tomography at SESAME (BEATS) is to pave the way for an efficient and sustainable operation of the Synchrotron light for Experimental Science and Applications in the Middle East (SESAME) research infrastructure. The project builds upon the OPEN SESAME project, and has the following key objectives:

- Develop and consolidate the scientific case and build up a science community, paying particular attention to the R&D and technology needs of the SESAME Members and beyond;
- Design, procure, construct, and commission a beam line for hard X-ray full-field tomography at SESAME;
- Foster collaborations among the project partners in all aspects of the technical work to ensure that a comprehensive transfer of knowledge to SESAME staff is accomplished within the lifetime of the project;
- Address the issue of sustainability of operation by preparing medium- to long-term funding scenarios for the tomography beamline and the facility.

The BEATS consortium is a blend of leading research facilities in the Middle East (SESAME and the Cyprus Institute), well established European synchrotron radiation facilities and high-energy laboratories (DESY, ELETTRA, ESRF, INFN and PSI) with a decades-long experience in synchrotron radiation research and technology, and more recently founded synchrotron laboratories (ALBA and SOLARIS).

The preparation of this **T**echnical **D**esign **R**eport (TDR) for the BEATS beamline at SESAME has been a truly collaborative effort of BEATS partners with an important know-how share and transfer to SESAME staff. SESAME colleagues worked together with ALBA and INFN on the definition of the x-ray source, with ALBA and Elettra on the front end design, with Elettra and ESRF on the beamline design, with ALBA on the radioprotection, and with the Cyprus Institute and ESRF on the IT and data management. It was a fortunate coincidence that works on the ALBA tomography beamline FAXTOR started at the same time and that the project for a hard x-ray tomography beamline at SOLARIS (POLYX) was recently approved, thus allowing the further enhancement of know-how transfer. Within this context the present TDR contains in the Annex as well the description of the FAXTOR and the SOLARIS tomography beamlines.

The TDR follows a template, developed at the ESRF in the frame of its upgrade programme. It comprises a short description of the science case (Chapter 3; fully elaborated in deliverable D2.1 of the BEATS project), the expected day one operation features (Chapter 4), and the description of the SESAME infrastructure (Chapter 5). This is followed by chapters on the general layout of the beamline (Chapter 6) and all the beamline components, including their simulated performance (Chapters 7 - 9). Chapter 10 deals with the beamline control, data acquisition and management, and the subsequent chapters cover radiation safety, risk analysis, the time line, and the budget. This is followed by a set of technical annexes, and, as already mentioned above, a description of the tomography beamlines at SOLARIS and ALBA.

2 Contributors

Abbadi, Anas (SESAME)
Aljamal, Basil (SESAME)
Al'Kailani, Omar (SESAME)
Al'Najdawi, Mohammad (SESAME)
Altissimo, Matteo (ELETTRA)
Attal, Maher (SESAME)
Alzu'bi, Mustafa (SESAME)
Bartolini, Riccardo (SESAME, moved to Diamond)
Campmany, Josep (ALBA)
Chrysostomou, Charalambos (CyI)
Cudin, Ivan (ELETTRA)
Ferrero, Claudio (†) (ESRF)
Font Massot, Narcís (ALBA)
Garcia-Fusté, Maria-José (ALBA)
Ghigo, Andrea (INFN)
Guiducci, Susanna (INFN)
Hamad, Adli (SESAME)
Iori, Gianluca (SESAME)
Kaprolat, Axel (ESRF)
Kołodziej, Tomasz (SOLARIS),
Korecki, Pawel (SOLARIS)
Krisch, Michael (ESRF)
Lausi, Andrea (SESAME)
Marcos, Jordi (ALBA)
Matalgah, Salman (SESAME)
Mittone, Alberto (ALBA)
Momani, Yazeed (SESAME)
Morawe, Christian (ESRF)
Nemoz, Christian (ESRF)
Paolucci, Giorgio (SESAME, moved to ELETTRA)
Rack, Alexander (ESRF)
Reyes-Herrera, Juan (ESRF)
Sabbatini, Lucia (INFN)
van Vaerenbergh, Pierre (ESRF)
Wawrzyniak, Adriana (SOLARIS)
Zahran, Iyad (SESAME)

3 The Scientific Case

The BEATS science case constitutes deliverable 2.1 – "Report on the Scientific Case for Micro-Tomography", which was submitted to the EC on July 31, 2020 (Lorentz et al. 2020). It reflects the increasing need for the hierarchical characterisation of the three-dimensional microstructure in materials, objects, and organisms. 3D images allow architectural and topological information to be retrieved about a specimen such as the shape, composition, orientation and size of its individual internal constituents, as well as the connectivity and correlations between these. **S**ynchrotron x-ray **C**omputed **T**omography (SRCT) developed rapidly since the middle of the 1980s with the advent of dedicated synchrotron x-ray sources, tremendous improvements in detector technology, data storage and processing capabilities. This has led to a boost of high-end synchrotron tomography with a wide range of different applications. Spatial resolutions from 50 μm^3 voxel size down to 0.2 μm^3 are routine, and the most advanced nano-imaging experimental stations (beamlines) provide resolutions down to 10 nm^3. Furthermore, the high brilliance of synchrotron x-rays allows time-resolved tomographic studies, typically with a few Hz up to a few hundred Hz acquisition rates, and the recording of single projection images with nanosecond resolution. The contrast of the images is either generated via the difference in the photo-electric absorption (absorption contrast) or electron density (phase contrast) of the constituent elements. Further contrast enhancement can be achieved via tuning of the x-ray energy to an absorption edge of one of the constituent elements or by using contrast agents.

The science case areas of the BEATS beamline (Figure 1) are based on close interactions with the scientific communities of current and potential synchrotron users in the SESAME region and on broad consultations with international experts. Therefore, special emphasis is given to the regional relevance of the presented scientific examples taking stock of existing research contributions from the region. The report addresses also user community building, support and coordination activities as well as future plans and targeted actions. Together with the documented science case, the report presents a full scientific agenda with the immense potential to create positive social, economic and health benefits for the region in the medium and long term.

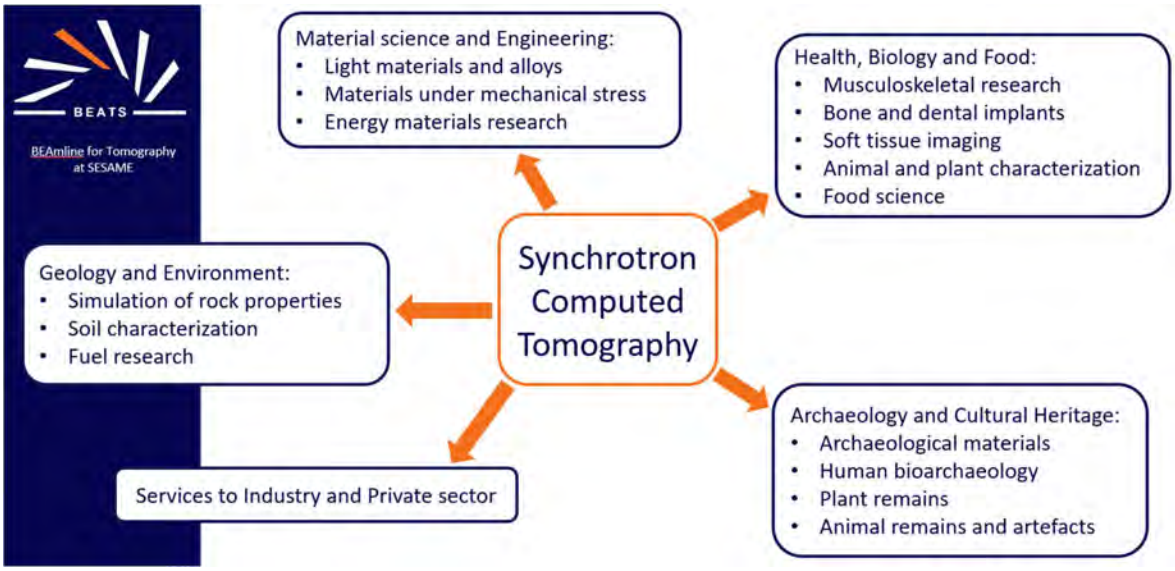

Figure 1: Areas of application of synchrotron computed tomography at BEATS.

Among the large diversity of applications, the following four science drivers of relevance were identified:

- Archaeology and Cultural Heritage – This includes the study of archaeological materials such as human, plant or animal remains and artefacts of animal bone, antler and teeth.
- Health, Biology & Food – Research in bone and dentistry; in vitro imaging of the brain vascular and neuronal network and of other organs such as the eye, heart, lung and liver; musculoskeletal and soft tissue imaging; bio mineralisation; entomology; food science.
- Material science and Engineering – Study and development of light and composite materials for construction and transport engineering; energy materials research.
- Geology and Environment – Research in soil and rock characterization; petroleum science and engineering.

It should be noted that applications within other domains as well as the possibility to provide services to industrial and private sector users are also envisaged, and that these four domains simply identify key areas for the scientific case for BEATS in the SESAME region as viewed currently.

4 Day One Operation

The BEATS beamline will operate an x-ray micro tomography station to serve and react to the diverse needs of a broad user community. Hard x-ray imaging in general can be applied to numerous scientific areas as outlined in chapter 3 of this TDR. Examples of potential day-1 applications of BEATS range from high-resolution phase-contrast tomography scans of biological specimens (e.g. insect morphology) and engineering materials (e.g. dendrite structure in alloys, lightweight metal foams, concrete or scaffolds for biological tissue repair), rapid scans of dynamical phenomena at medium resolution (e.g. liquid flow in porous materials) to strictly low-dose applications in biomedical imaging (e.g. soft tissue, bone and implant specimens) and cultural heritage (unique artefacts made from organic materials). Accordingly, the setup of BEATS will allow operating the beamline in different modalities, giving the opportunity to tune size, energy and total flux of the beam to the specific application.

4.1.1 Pink beam modality

The first modality being commissioned and available to users will be the beamline operation with filtered white beam (so called pink beam). In this configuration, the sample is positioned at approximately 43 m from the photon source and is illuminated with the direct beam emitted by the wiggler, without the use of a monochromator. The expected flux delivered through 1 mm^2 at the sample position can be as high as 1×10^{10} Ph/s/mm^2 in 0.1% of the source bandwidth (Figure 2A), for a maximum usable beam size of 42×15 mm^2 (Figure 2B). Dense materials such as rocks can be scanned, and fast experiments performed in this modality. Due to the electron beam properties in the SESAME storage ring generating an x-ray source almost 2 mm in horizontal size, the beam will have low transverse coherence (< 1 µm) in this configuration. For pink-beam propagation-based phase contrast tomography requiring higher coherence length, in-vacuum slits in the beamline front end will be closed to generate a horizontal aperture down to 500 µm in size. This pinhole will act as a smaller and partially coherent secondary photon source. The reduction in photon flux density at the sample position when the slits are closed to 500 µm is estimated to be around 70% (Figure 2A). Due to the concurrent reduction of the beam size, the field of view for phase contrast imaging will be limited to 10 mm or less. For both slits open and slits closed configurations, it will be possible to tailor the energy spectrum and particularly filter the low energies of the white beam with several attenuators installed in the front end (Figure 2A).

Versatile and high-precision sample positioning and rotation stages based on air-bearing technology will allow the 3D imaging of a variety of objects in pink beam, with microscopic as well as macroscopic resolution. Indirect x-ray detectors with shielded and interchangeable objective lenses for operation in pink beam will be installed, achieving object pixel sizes in the range from 6.50 µm down to 0.65 µm. The detector systems foreseen for day-1 will allow recording radiographic images with frame rates up to 100 fps when the full camera sensor is used or even higher reducing the acquired field of view. The reader can find numerous examples of the application of synchrotron computed tomography with pink beam (both absorption and propagation-based phase contrast) in the report on the BEATS scientific case (Lorentz et al. 2020).

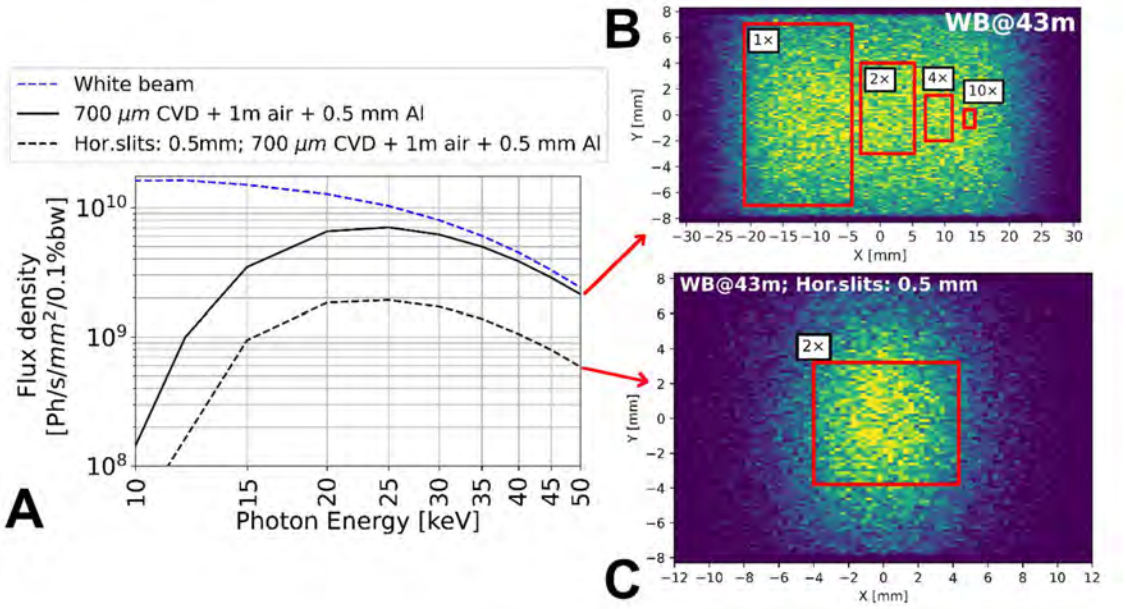

Figure 2: expected day-1 performance in pink beam mode. (A) Plot of the expected photon flux through 1 mm² at the sample position (43 m from source) with primary slits open (solid line; high flux mode) and with primary horizontal slits closed to 0.5 mm forming a secondary source with improved coherence (dashed line; high sensitivity mode for phase-contrast applications). The plot considers attenuation from two diamond windows (0.7-mm-thick in total), from 1 m of propagation in air after the last window as well as from a 0.5-mm-thick aluminium foil to reduce low energy contributions. The drop in photon flux density when the horizontal slits are closed to 0.5 mm is approximately 70%. White beam flux density (dashed blue line) shown for comparison. (B) Pink beam size available at the sample position in high flux mode. Red boxes indicate the field of view available with different objective magnifications. (C) Pink beam size at the sample position in high sensitivity mode (horizontal primary slits closed to 0.5 mm). Field of view with a 2× microscope lens (3.25 µm object pixel size) indicated in red for comparison with B.

4.1.2 Monochromatic beam

The second modality and first major upgrade being commissioned will be the monochromatic beam mode for photon energies between 8 keV and 50 keV. A double multilayer monochromator will be installed in a dedicated optics hutch. Two multilayer stripes coated on a common Si substrate will be installed for operation at the low (8 to 20 keV) and high (>20 keV) regions of the available energy spectrum. The expected energy resolution of the monochromatic beam will be between 2% and 4%. Figure 3 shows two plots of the monochromatic photon flux expected through 1 mm² at the sample position with both multilayer stripes. Applications requiring low dose as well as high-resolution imaging will be possible by using the monochromatic beam.

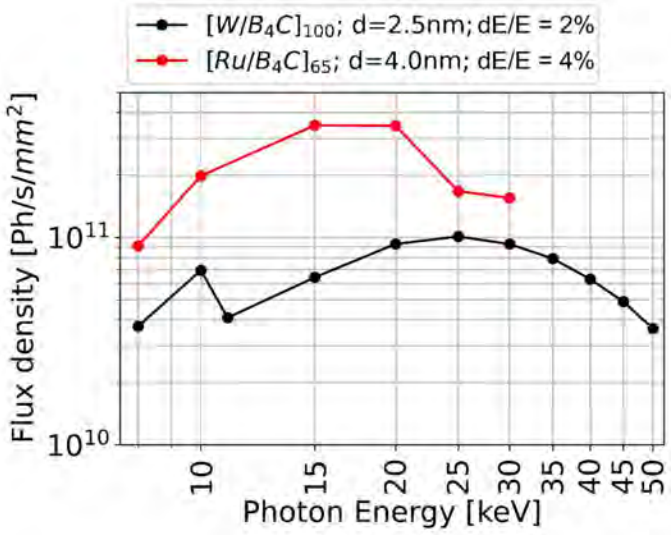

Figure 3: Flux density of the BEATS beam monochromatized by a double multilayer monochromator when the sample is positioned at 43 m from the source. Red and black plots show the expected photon flux density when multilayer coatings for low and high energies are used, respectively. A Ru/B_4C coating with d=4 nm and 4% resolution is considered for low energies (red), while a W/B_4C with d=2.5 nm and expected resolution of 2% will be used at higher energies (black).

4.1.3 Sample environment and future upgrades

The beamline layout and day-1 equipment will allow the installation of different devices for controlling the sample environment during *in-situ* studies. The installation of a mechanical testing device for *in-situ* tomography of materials while applying tensile and compressive loads is foreseen. Sample stages for temperature (e.g. furnace, cryo or Peltier systems) or pressure control are also envisioned for future upgrades of the beamline, together with the installation of large field of view detector system allowing to exploit the entire 45-mm-wide beam size at the sample position and high-speed cameras for fast-tomography applications with scan time below 1s.

Thanks to the properties of the BEATS photon source, to the versatile layout of the experimental station and to the possibility to work with filtered white beam, the beamline can be utilized for experiments in the hard x-ray regime other than tomography and radiography. One such example is diffraction topography (also called Bragg-Diffraction imaging): a technique well suited to study dislocations and defects in single crystals. Contrary to classical radiography, diffraction topography exploits the beam diffracted by the sample instead of photons directly transmitted through it. The technique can produce maps of crystalline perfection acquired in a single-shot manner. Contrast is given by crystal defects violating Bragg's law and leading to intensity modulations in the diffracted beam which can be recorded by an area detector. Compared with techniques such as electron microscopy, the advantage of diffraction topography consists in the high sensitivity to dislocations occurring at atomistic length-scales over fields of view that can easily span 10 mm × 10 mm. Classical applications of diffraction topography are the study of wafers (formerly Si wafers), nowadays targeting on novel crystalline materials for semiconductor technology such as SiC or GaAs. A possible further upgrade of the beamline optical configuration includes the installation of a Bragg or Laue beam expander to increase the vertical available field of view.

5 The SESAME Infrastructure

5.1 General description of the storage ring

SESAME is a third generation light source facility, with an electron beam energy of 2.5 GeV, located in Allan, Jordan. The injector consists of a 22.5 MeV microtron and a 800 MeV booster synchrotron, with a repetition rate of 1 Hz. The main storage ring parameters are given in Table 1Table 1: Parameters of the SESAME storage ring. The storage ring is composed of 8 super periods with 16 dipoles and 16 straight sections of alternate length of 4.163 m and 2.113 m respectively. 4 straights (2 long and 2 short) are allocated for Injection, RF cavities, beam diagnostic etc., leaving twelve straight sections available for insertion devices. The horizontal emittance of the storage ring is 26 nm.rad. Each dipole chamber is equipped with two ports at 6.5° and 0^0 collecting dipole and insertion device radiation, respectively.

Energy (GeV)	2.5
Circumference (m)	133.2
N. of Periods	8
Emitt.(h/v nm.rad)	26.0/0.26
Harmonic Number	222
Beam sizes in the center of long straight (h/v um.)	~ 800/20
Beam sizes in the center of short straight (h/v um.)	~ 800/14

Table 1: Parameters of the SESAME storage ring

The lattice design is a **D**ouble **B**end **A**chromat (DBA), with vertical focusing gradient inside the dipoles and dispersion distribution in the straight sections. The bare lattice has only 2 families of quadrupoles and 2 of sextupoles. The quadrupoles are powered by separate power supplies. The optical functions for a full period are shown in Figure 4. The lattice is quite flexible to compensate locally the optical perturbation introduced by insertion devices.

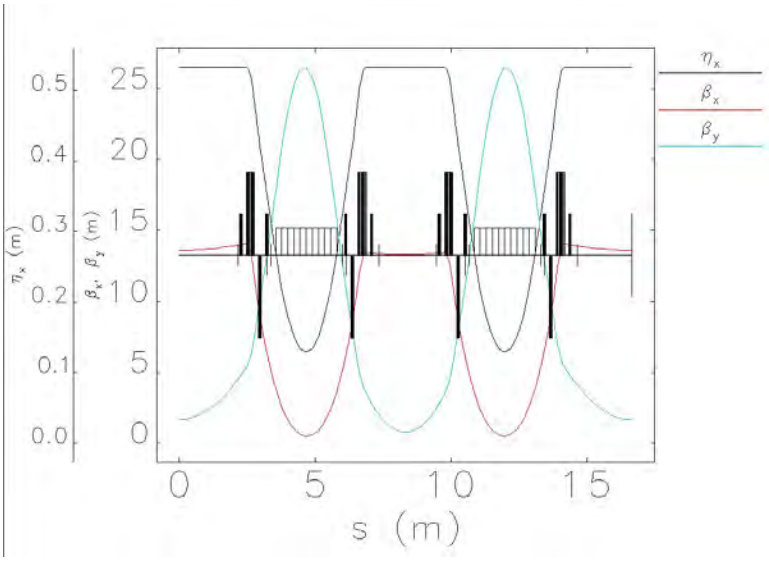

Figure 4: SESAME full period optical functions

5.2 Location of the beamline

The BEATS beamline will be located at port I10 of the SESAME storage ring (Figure 5). The space available for BEATS in the storage ring tunnel and experimental hall of SESAME is defined by the radiation protection wall of the storage ring and by neighbouring beamlines. Sufficient space has to be reserved for the installation and servicing of all beamline components. A service door (width 4m, height 5m) on the opposite side of the hall is available to bring heavy equipment inside. A crane (8 tons maximum) is installed inside the experimental hall.

As can be seen from Figure 5, the position of BEATS is determined by the maximum available beamline length. By making use of SESAME's experimental hall and of two rooms of the adjacent service area it is possible to accommodate a beamline with a maximum length of 45 m. The modifications to the SESAME building required to make room for BEATS have moderate impact and consist of:

- Dismantlement of toilets and adjacent laboratory (power supply laboratory). The laboratory will be moved to another free room of the service area.
- Dismantlement of false ceiling, mechanical parts, electrical pipes and of 3 walls.
- Reinforcement of the floor in the service area with concrete (20 cm) and screed (8 cm) reinforced by high tension steel; mechanical polish; Epoxy layer.

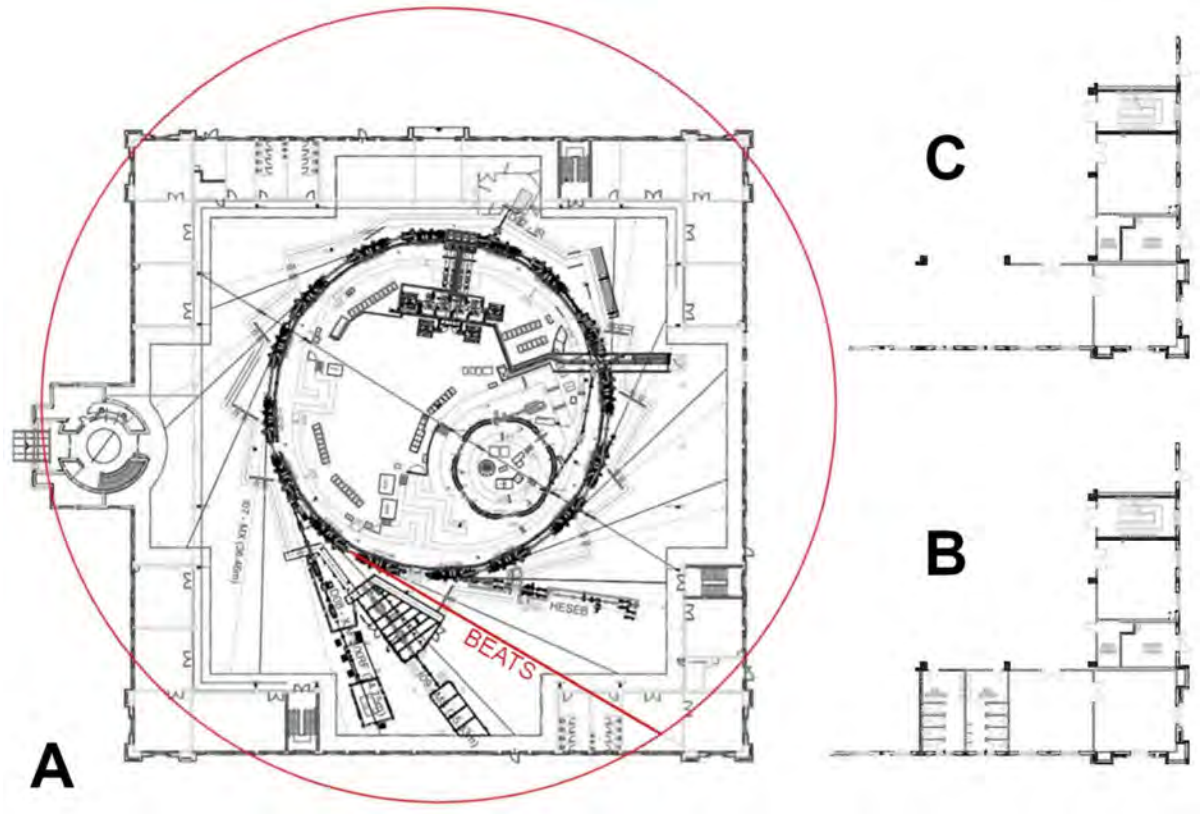

Figure 5: A: Floor plan of the SESAME facility showing the location of BEATS. The red circle indicates the end point of a 45 m long beamline. B: Detail of the current facility floor plan at the future location of the BEATS experimental and control hutches. C: Sketch of the modifications to the SESAME building required to host the infrastructure of BEATS.

5.3 SESAME standards

5.3.1 Electrical Power

The AC distribution board is fed from a 1.5MVA, 33kV/415V – 5% distribution transformer, via power switches with magneto-thermal protection. The 415V secondary star mid-point is earthed at the transformer and the neutral is directly distributed to the equipment. Thus, the neutral must not be earthened at any other point. SESAME 415VAC network characteristics are listed in Table 2.

Line voltage	415V RMS ±10% (TNS neutral mode: three phases + neutral +PE)
Frequency	50 Hz ± 1%
Voltage harmonic distortion	8% rms
Phase imbalance	± 3%
Conductor distribution	3 phases + neutral + PE
Short circuit capacity	<40 MVA
Peak main surges	1500V rms for 0.2 ms & 600V rms for 10 ms
Wire colours	BS7671 prior to 31 March 2004

Table 2: Electrical mains specifications

5.3.2 Cooling System

The beamline components will be supplied by cooling water and pressurized air with the following specifications common to the experimental hall of SESAME:

- Cooling water: 24°C ± 0.2°C, 8 bar, deionized water, 0.23 µS/cm, Swagelok couplings.
- Compressed air: 10 bar, Festo couplings, 0.01 microns max. particle size.

5.3.3 Vacuum System

The standards of the SESAME vacuum system are described in the annex document "*SESAME Beamlines Vacuum standards*".

5.3.4 Control System

The control system allows the access, monitoring and control of the various devices that form the accelerator and beamlines from workstations located in the main accelerator control room and inside the beamlines control hutches.

The control system at SESAME (Figure 6) is based on EPICS (Experimental Physics and Industrial Control System). SESAME utilizes the EPICS toolkit (Base: 3.15.6) for both machine and beamlines control. Each beamline at SESAME has its own control system and its own network. Insertion devices are integrated into and considered to be a component of the accelerator. Access to the accelerator control system (e.g. to retrieve parameters like machine current, energy, …) is granted to the beamline staff via a Channel Access Gateway server. Vacuum pumps and gauge controllers are controllable either via serial protocols or ethernet. Terminal servers are needed to allow the control system software access to serial protocol devices.

All components have a self-safe behaviour (i.e. cooled devices are equipped with flow rate sensors and thermocouples for temperature control).

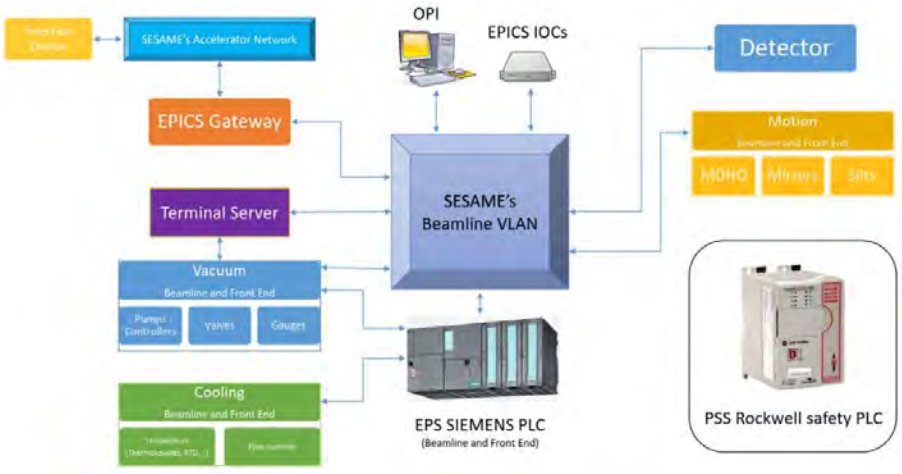

Figure 6: General structure of the SESAME beamline control system

For each new beamline, the control group of SESAME is in charge of the development of the beamline control system and for providing the staff with user-friendly interfaces for the operation of the experimental equipment.

The beamline control system comprises the following sub-systems:

- The **E**quipment **P**rotection **S**ystem (EPS) protects the equipment from physical damage. This system is implemented by a SIEMENS programmable logic controller (PLC) that monitors the temperature of high heat load components, vacuum status in the beamline and coolant flow to components. The EPS is also responsible for reporting the status of beamline components to the main control system and for taking any required protective action (e.g. close shutters, close valves, trip the accelerator, …). Devices integrated within EPS are:
    - Gate Valves: These valves are used to protect the vacuum in the beamline, in case of vacuum interlock the PLC removes the 24 VDC from the valve solenoid and forces it to close.
    - Vacuum Gauge Controllers: The gauge controllers collect the readings from sensors installed on the different beamline components. These controllers display the pressure and send it to the main control system, the device also has configurable set points, if the vacuum level in the beamline decreased to the set point limit, the gauge will send a signal to the PLC to take the protective action to protect the vacuum in the beamline parts.
    - Flow Switches: Flow switches are calibrated to a certain flow, if the flow gets lower than the calibrated value, this switch will send a signal to the PLC to take the protective action.
    - Temperature Switches: Some beamline components are equipped with temperature switches, if the temperature rises above a certain value, the switch will send a signal to the PLC to take the protective action.
    - Thermocouples: Thermocouples are temperature sensors with fast response and high range, they are distributed in the beamline to monitor the temperature of high heat load components.
    - Pressure Gauges: Pressure gauges are used to read the pressure of supply and return water to the beamline cooling circuits, they also transmit the signal back to the PLC.
- Motion Control System: all motorized components of the beamline are controlled via a standardized controller (SESAME Motion Box) providing the interface between EPICS and

motors, switches and encoders. The SESAME Motion Box was designed and developed at SESAME. The specifications of the system are described in chapter 19 “Annex: Motion Control System Standard”.

6 Beamline general layout

A sketch of the BEATS beamline layout is shown in Figure 7. The design of the beamline was established taking into account the various user needs by allowing for a variety of operation modes and ensuring sufficient photon flux density in filtered white beam or monochromatic beam over an energy range from 8 keV up to 50 keV. By displacing the sample position in the experiment, the beam size impinging on it and the propagation distance between sample and detector can be varied, thus allowing to scan objects with a resolution ranging from the macroscopic to the microscopic scale.

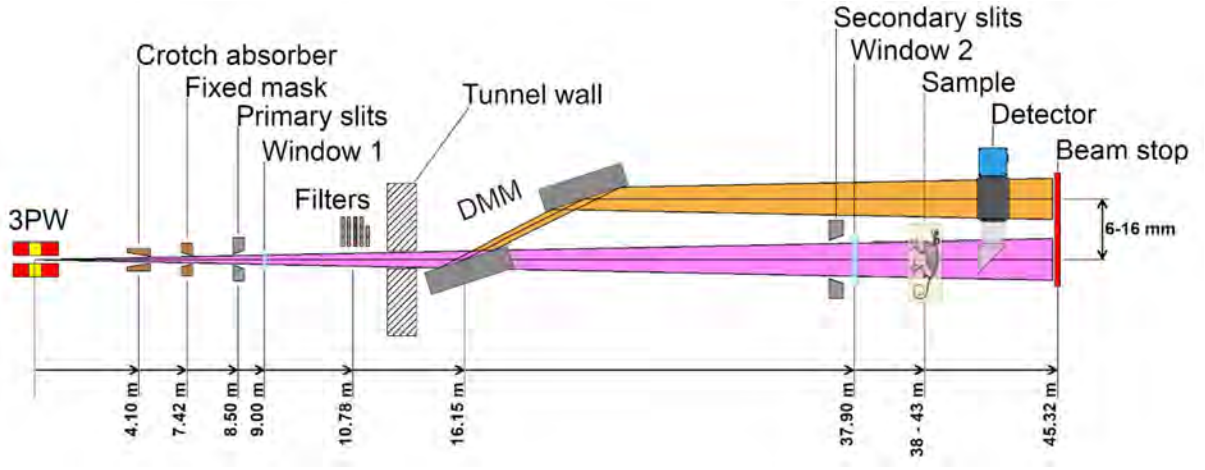

Figure 7: Schematic layout of the BEATS beamline showing all optical beam-defining elements.

The backbone of this concept consists of a powerful insertion device, primary slits which can act as secondary source and a double-multilayer monochromator (DMM) with pink beam option. The broad energy range and high photon flux required will be achieved by a 3T 3-pole wiggler as the x-ray source. Depending on the energy range and resolution needed as well as on limitations of the radiation dose, the beamline will either use the monochromator (8 keV to 50 keV, ΔE/E: 2% to 3%) or a filtered white beam with minimum energy tuneable by absorbers in the front end. This will allow for a high photon flux density over a broad photon energy range which is crucial for x-ray imaging techniques, especially for micro tomography.

Due to the characteristics of the SESAME storage ring, the insertion device constitutes an x-ray source with a rather large horizontal size (up to 2 mm) and divergence (15 mrad). Therefore, over the given energy range and independently of monochromatic or polychromatic operation, two modes of operation have to be considered:

- When a high raw photon flux is the figure of merit (for instance for experiments requiring fast acquisition or high flux density at high energies), the primary slits will be left completely open to illuminate the sample with the entire beam. In this case, the large photon source size will have a detrimental effect on the coherence properties of the wave front at the position of the experiment.
- When high sensitivity is required and spatial coherence of the beam is more important (e.g., for phase-contrast tomography), the primary slits will be partly closed to define a smaller, secondary source of a few 100 µm, of enhanced coherence properties.

Figure 8 presents a drawing of BEATS beamline layout at the SESAME facility.

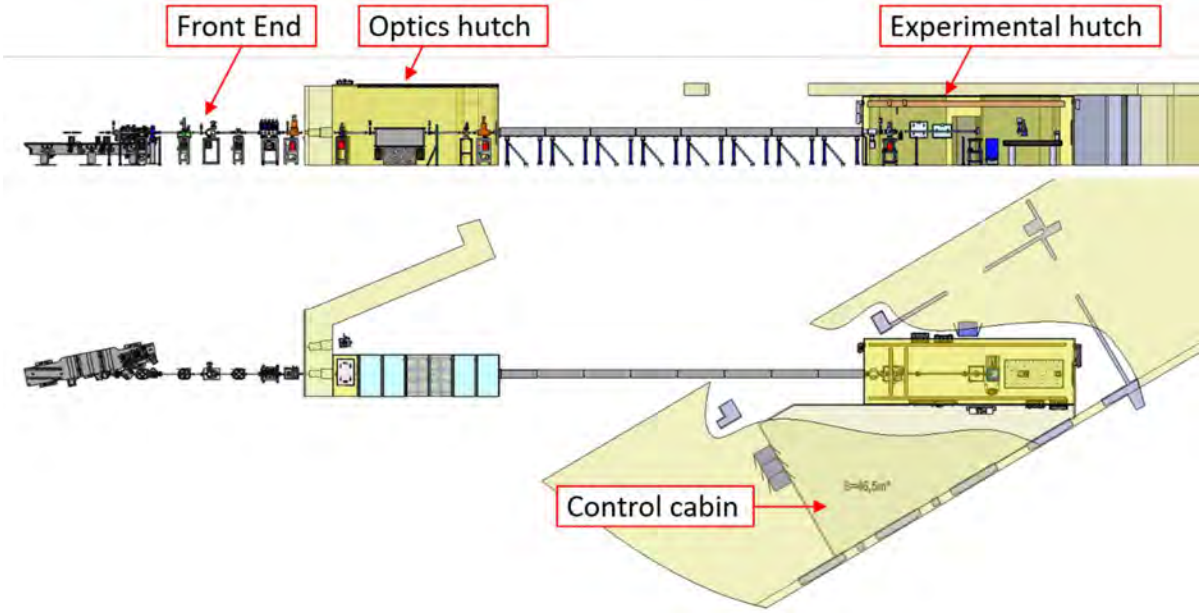

Figure 8: Layout of the BEATS beamline showing the location of the equipment inside the SESAME storage ring tunnel (beamline front end) and experimental hall (optics and experimental hutches).

The **Front End** comprises photon absorbers and stoppers, the fixed mask, a window separating the machine and the beamline vacuum, attenuators and the primary slits The maximum divergence of the beamline as defined by the fixed mask will be 1 mrad (h) by 0.36 mrad (v), leading to a maximum beam size available at 43 m from the source of 43 mm (h) x 15.5 mm (v) for the pink beam.

The main optical component of BEATS will be a **Double Multilayer Monochromator** (DMM) placed outside of the SESAME storage ring tunnel in a dedicated **Optics Hutch**. The DMM will allow to select the photon energy between 8 and 50 keV with an energy bandwidth of 2% to 3%. We consider one pair of stripes, coated with [W/B_4C] of 80 to 100 layers. For a coating with 2.5 nm d-spacing and for energies within the range from 8 to 50 keV, the incidence angle will then vary between $\theta = 1.81°$ and $\theta = 0.29°$. At the largest incident angle, the thermal power density will reach 80 mW/mm^2 and will be dissipated by water cooling of the first mirror. A second pair of stripes (e.g. [Ru/B_4C] with 4 nm d-spacing) will maximize the photon flux at low energies (8 – 20 keV). These multilayer stripes will be coated on Si substrates with an active length of approx. 300 mm. Precision goniometers and translations will control stripe selection, incidence angle and in general the alignment of the two multilayers. The second multilayer will be installed on an independent tower able to translate in the X-ray beam direction.

The total length of the beamline will be approximately 45 m. An **Experimental Hutch** of 9 m length will house sample and detector stages. These will translate on air pads for a broad range of source-to-sample and sample-to-detector beam propagation distances. The sample stage is a large size, versatile equipment allowing a wide range and, at the same time, accurate sample positioning. It will be equipped with a heavy-duty, high-precision rotation stage for the scanning of samples of several kilograms with sub-micron resolution.

Secondary slits positioned at the beginning of the experimental hutch will shape the beam at the sample position, whereas a fast shutter will reduce the exposure of delicate samples. Different full-field detectors based on scintillating screens and sCMOS sensor cameras will be available for operation in monochromatic or filtered white beam. A broad range of applications requiring either macroscopic

resolution over a large field of view or sub-micrometre resolution will be covered by objective magnifications ranging from 1x to 20x. Fast and lossless data collection and transfer will be attained by state-of-the-art instrument control and data acquisition interfaces.

A detailed description of the beamline equipment is presented in the following chapters.

7 The x-ray source

7.1 The design

From the start of the project onward, several options for the beamline's x-ray source were discussed (for details see BEATS deliverables D3.1 and D3.2):

- Installation of a **3 T superbend** magnet, replacing an existing dipole of the SESAME storage ring. This would have necessitated 2 new quadrupoles, a completely new vacuum chamber for the chosen section of the storage ring, and a substantial modification of the affected girder (or even a new design and construction). Compared to the maximal magnetic field of 1.4 T of a standard SESAME bending magnet, the field of 3 T, however, would shift the critical energy of the photon beam from 6 keV to 12.5 keV.
- A high-field **multipole in-vacuum wiggler** of 2.5 metres length and 50 periods, which would yield the same photon spectrum as the superbend together with a substantial increase in flux, however, would lead to large attractive forces between the magnetic structures, require expensive mechanics and, very likely, the introduction of superconducting technology and infrastructure at SESAME.
- A **3-pole wiggler of 3 T magnetic field**, operating in a SESAME short straight section at a gap of 11 mm. It has proven possible to design such a device with very low multipolar effects on the SESAME storage ring optics while as well reducing the attractive forces between the magnetic structures leading to minor mechanical constraints.
- A **2-pole wiggler** design as it is currently introduced at the ESRF during the EBS upgrade. This device would increase the flux by a factor of 2 vs. the 3-pole wiggler, however, the emission would be off-axis and require considerable design work.

The decision was taken in consultation with the SESAME Management to explore the 3-pole wiggler (3 T) solution with the following boundary conditions:

- Minimum gap: 11 mm
- Maximum field: ~3 T
- Magnetic length: < 1 m.
- Spectral range achieved with flux > 10^{11} ph/s.mm^2.0.1%bw: 20-50 keV

7.1.1 The Conceptual Model (basis for the Call for Tender):

A magnetic model (see Figure 9) has been generated taking into account the aforementioned parameters as well as the need to reduce as much as possible adverse multipolar effects on the storage ring's electron orbit. It allows reducing the remnant field of the individual magnetic blocks to B_r=1.28 T, thus making the procurement of the magnetic material easier. Furthermore, the magnetic force between the magnetic structures was reduced to 1200 N. The peak field is 3.0025 T.

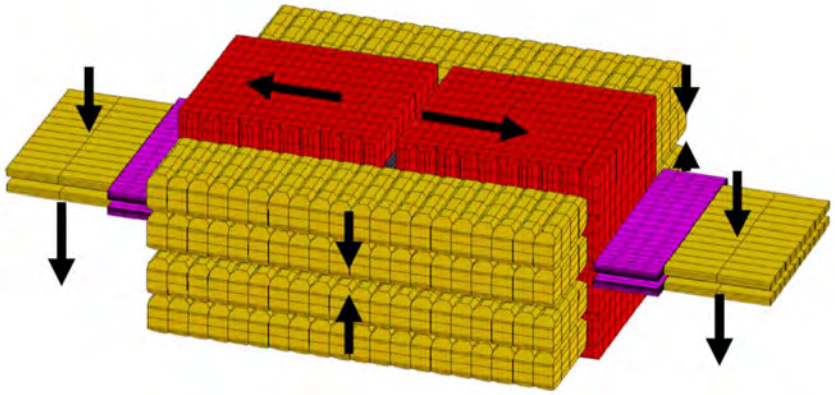

Figure 9: Axis definition and magnetic model. Red and yellow parts are NdFeB magnets. Pink parts are iron poles (there is another iron pole –grey– in the center). The overall length is 0.755 m, the overall width is 0. 400 m, the overall height is 0.331 m and the minimum gap is 11 mm.

Figure 10 shows the magnetic field of the 3-pole wiggler along the direction of the particle beam:

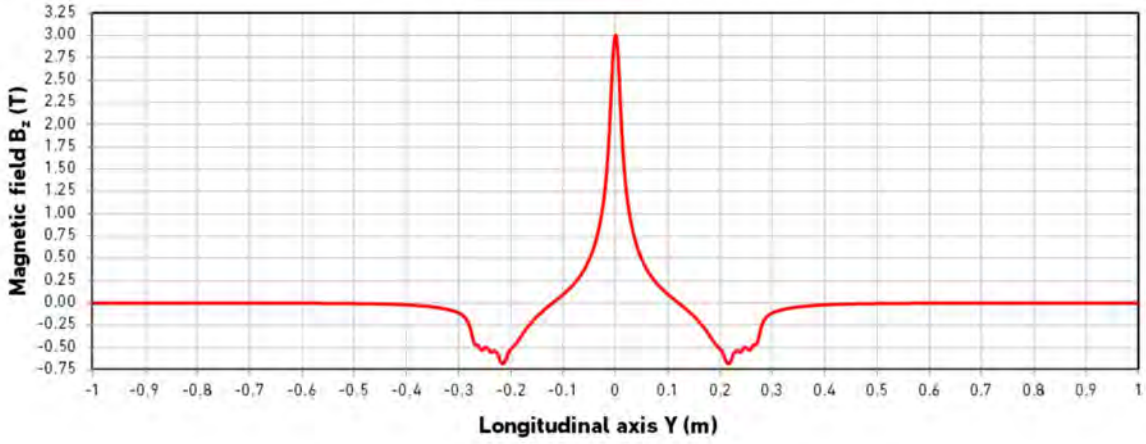

Figure 10: Magnetic field of the 3-pole wiggler

This design minimised the effect on machine dynamics by:

- Minimising 1st and 2nd order field integrals and
- Minimising field effects on particles not traveling exactly along the ideal orbit of the storage ring. Figure 11 and Figure 12 show the horizontal and vertical kickmap, respectively, which are sufficiently flat for the regime of the usual extension of the particle bunches.

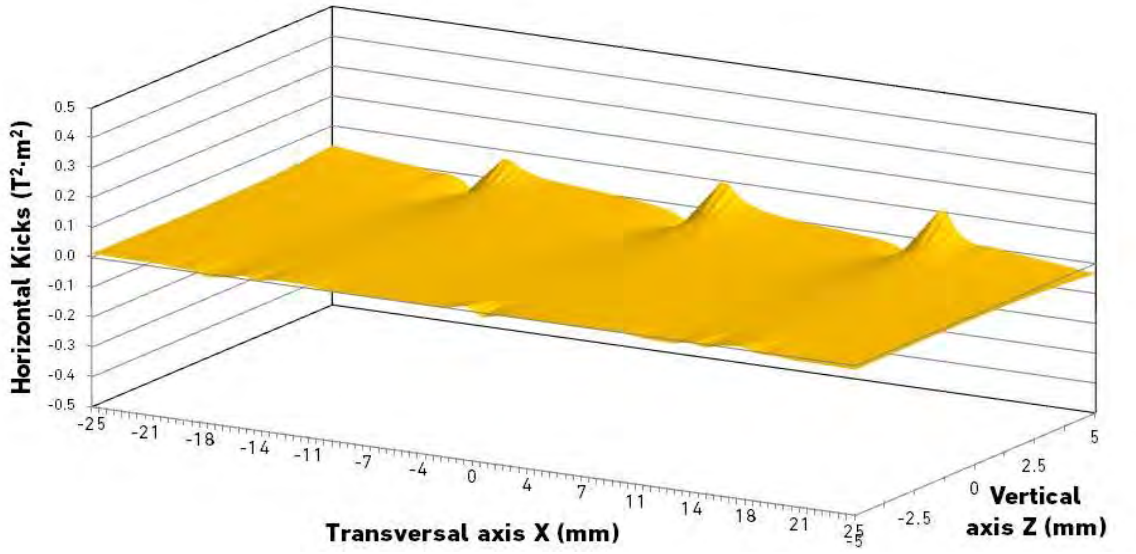

Figure 11: Horizontal kickmap of the BEATS 3-pole wiggler

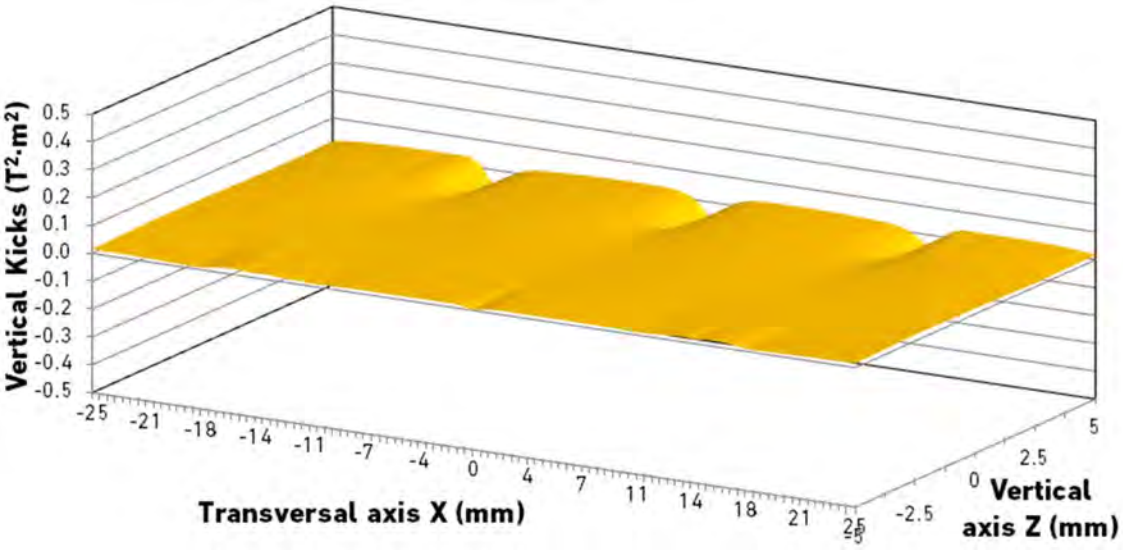

Figure 12: Vertical kickmap of the BEATS 3-pole wiggler

For more detailed information on the manufacturing process and the magnet specifications see BEATS deliverable D3.4.

7.1.2 Photon source characterization

In this paragraph we present simulations of the BEATS 3-pole wiggler performed with the XOP (Sanchez del Rio and Chubar 2014) and ShadowOui (L. Rebuffi and Sánchez del Río 2016) add-ons of the OASYS suite (Luca Rebuffi and Rio 2017) as well as with Spectra (Tanaka and Kitamura 2001).

Plots of the horizontal and vertical photon source size and divergence are shown in Figure 13. The corresponding phase-space plots are shown in Figure 14. At 5 keV and in the horizontal plane (Figure 13A and B, Figure 14A), there is a strong asymmetric and diverging component of the source emission due to the 0.68 T side poles of the 3-pole wiggler. At 10 keV, this effect vanishes almost entirely. To minimize the negative impact of the side poles, the minimum working energy for BEATS will be 8 keV.

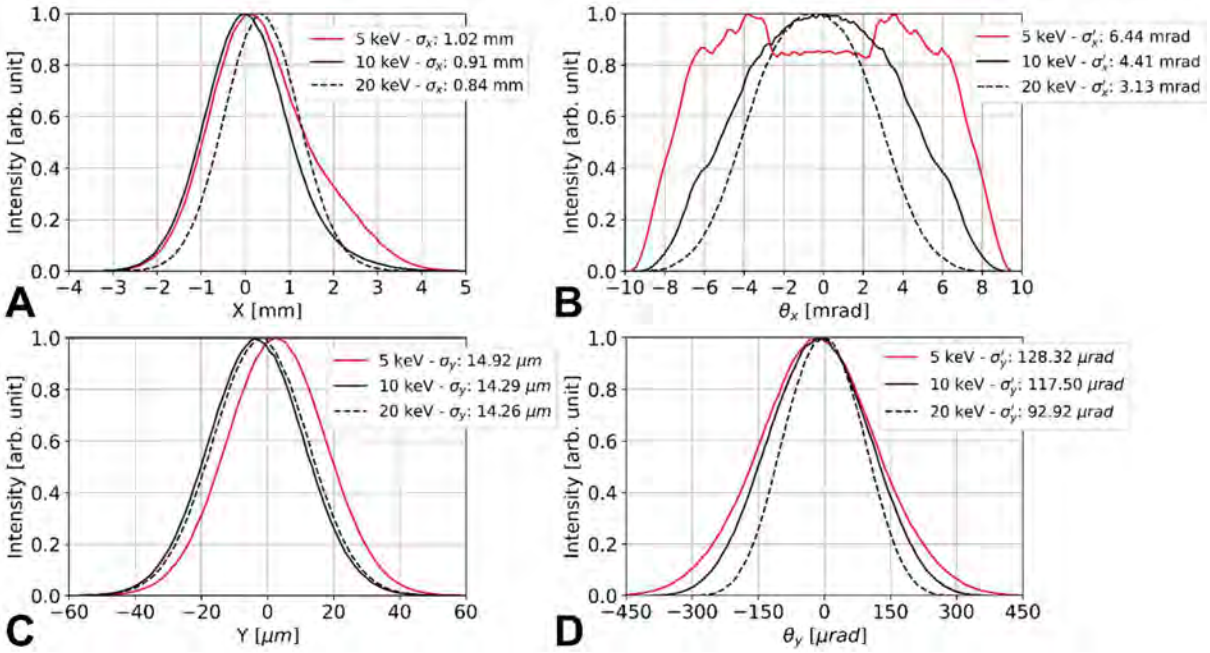

Figure 13: Photon source size and divergence of the BEATS 3PW at 5, 10 and 20 keV as calculated by numerical simulation with XOP and ShadowOui. Horizontal source size (A) and divergence (B). Vertical source size (C) and divergence (D).

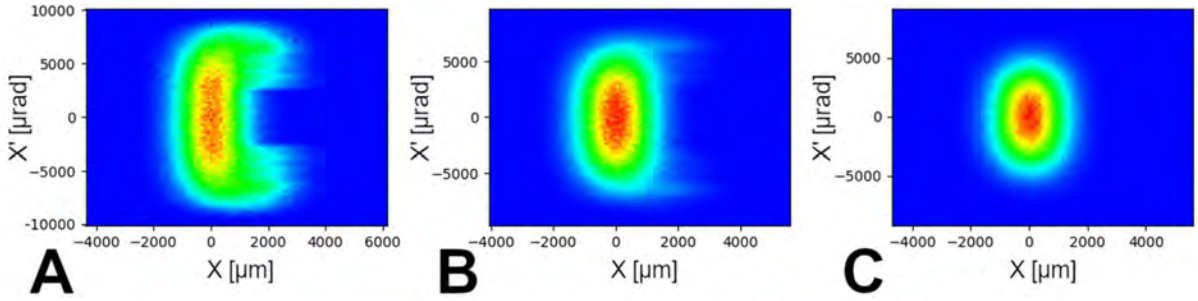

Figure 14: Horizontal phase space intensity distribution of the BEATS 3PW at 5 keV (A), 10 keV (B) and 20 keV (C) photon energies.

The total thermal power delivered by the BEATS 3-pole wiggler is approximately 1 kW, with maximal values of the power density (for electron beam current in the storage ring of 400 mA) of 250 W/mrad^2 (Figure 15).

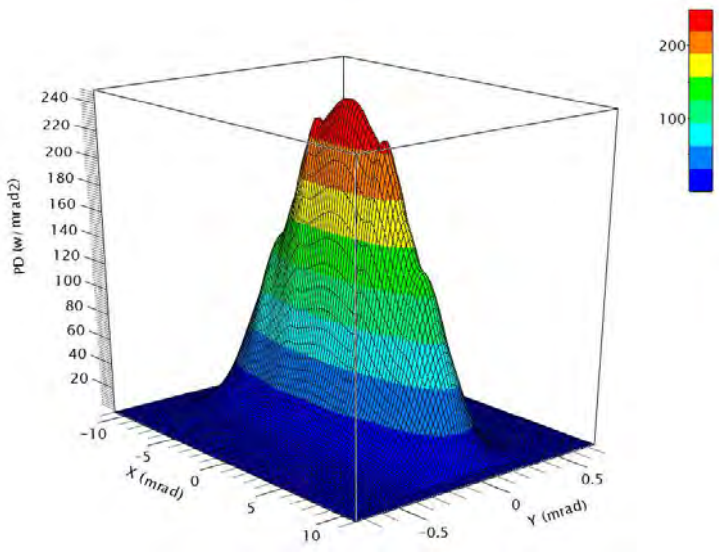

Figure 15: Angular power density (in W/mrad^2) delivered by the 3-pole wiggler.

7.1.3 Flux of the 3-pole wiggler – comparison with other tomography beamlines

Figure 16 shows a comparison of the flux emitted by the BEATS 3-pole wiggler in a unit horizontal angle and 0.1% BW with that of six other tomography beamlines. Two of these (ID17@ESRF and beamline 6C@PLS-II, black lines in Figure 16) have multipole wigglers as their x-ray source. SYRMEP@Elettra and TopoTomo@ANKA (red lines in Figure 16) are bending-magnet-based tomography beamlines. TOMCAT@SLS uses a 2.9 T superbend. The flux of an undulator beamline (P05@PETRA3) is also displayed for comparison.

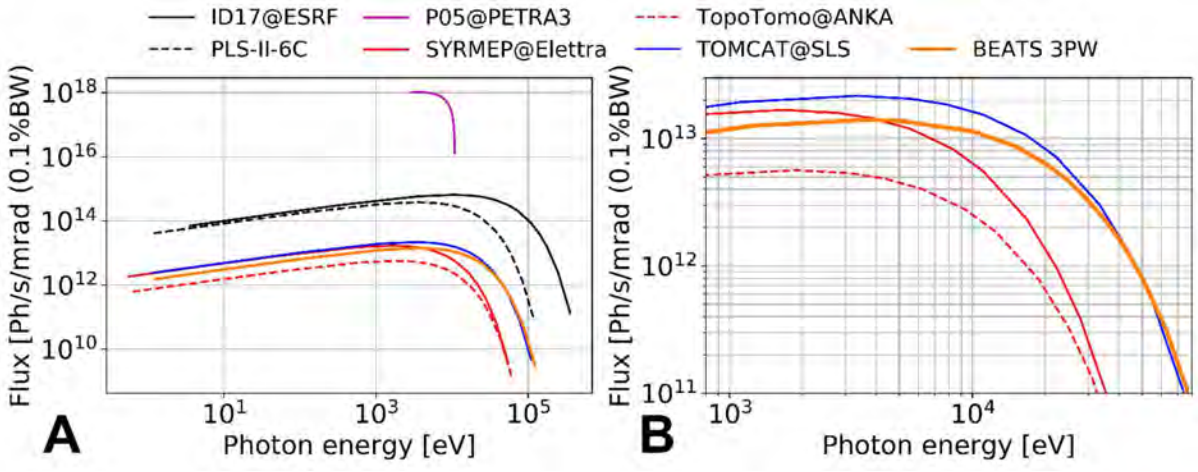

Figure 16: Photon flux in 1mrad horizontal angle. A) Comparison with tomography beamlines at other facilities: bending magnet beamlines in red, wiggler beamlines in black, the undulator of P05@PETRA3 is in magenta. TOMCAT (2.9T superbend) in blue. B) Detail of the 1-80 keV region. To reproduce this plot visit the following Binder link.

8 The Front End

The front end represents the first part of the beamline and is confined in the storage ring tunnel.

It has a key role, as it absorbs undesired radiation (and its thermal load) emitted in the direction of the beamline during injection and operation, thus ensuring personnel and equipment safety during experiments. It provides the beam collimation, prevents the white x-ray beam from impinging on unprotected and uncooled surfaces; it allows to extract the useful part of the x-ray radiation, to shape it and to fully stop it, in case access to the beamline components downstream is required in full safety. Furthermore, the Front end assures the integrity of the storage ring vacuum.

Figure 17 and Figure 18 show the layout of the Front end components for the BEATS beamline.

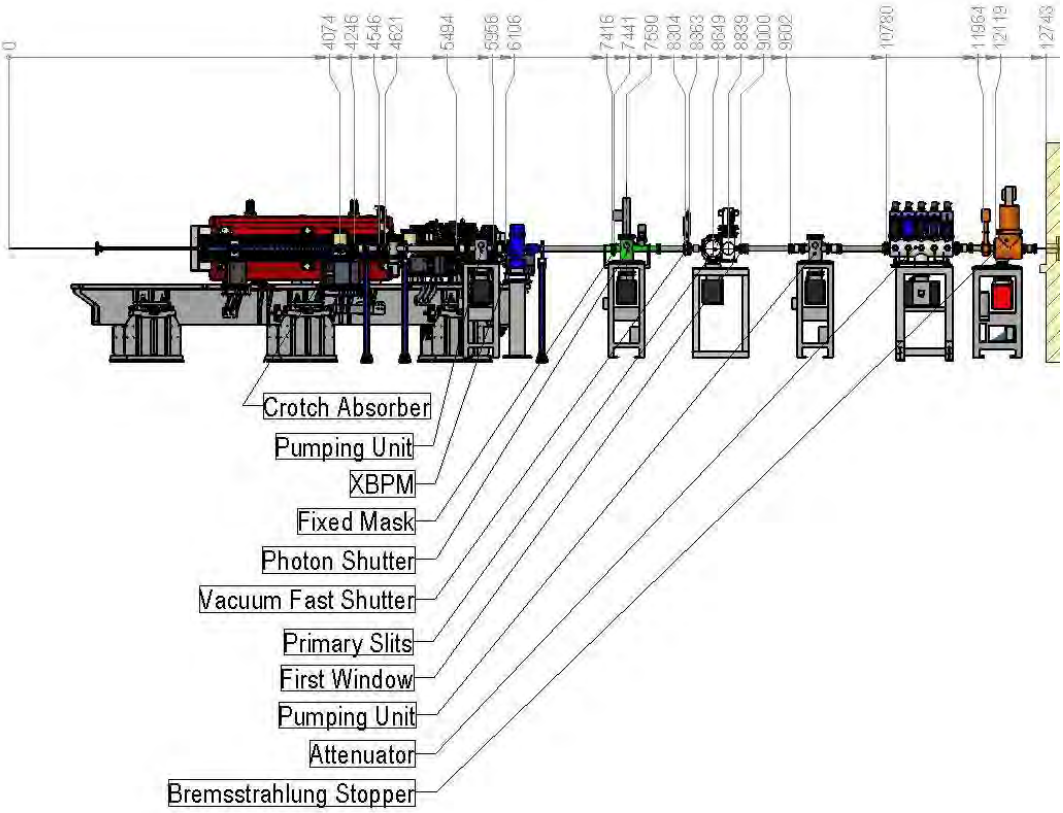

Figure 17: Layout of the BEATS beamline's front end, side view

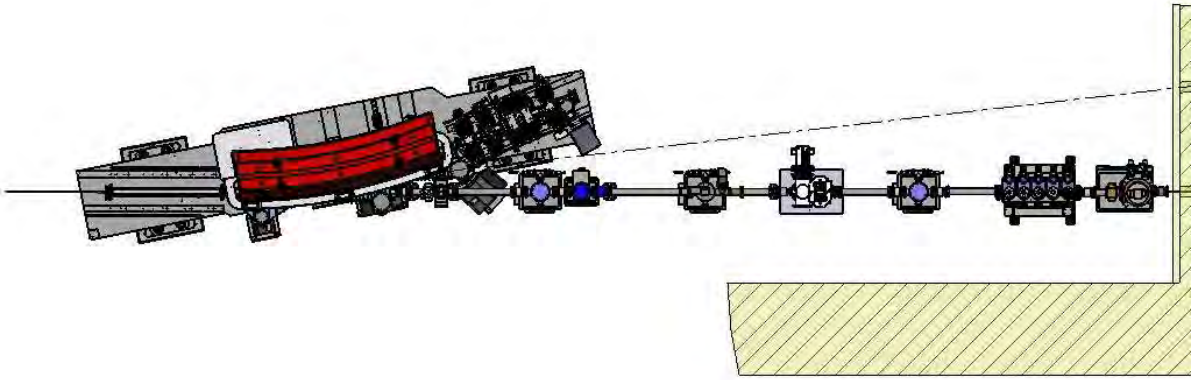

Figure 18: Layout of the BEATS beamline's front end, top view

For all finite element simulations to predict temperature and stress distribution in front end components we applied conservative criteria for the maximal acceptable thermal load. Table 3 shows the limit values for temperature and von Mises stress applied to prevent material creeping.

Material	*Max temperature (°C)*	*von Mises stress (MPa)*
OFHC COPPER	150	210
GLIDCOP	300	400
AISI 316L	400	200

Table 3: Limit values for temperature and stress for materials used in Front end components

To prevent the boiling of cooling water and to maintain single-phase heat transfer, the maximum temperature on the cooling wall was strictly limited to be below the boiling temperature at operating water pressure within the cooling channels (148°C at a typical pressure of 4.5 bar, calculated considering inlet water pressure and pressure losses).

8.1.1 Coordinate system

The coordinate system used in this TDR is the one used at SESAME, which is the right-handed with Z pointing towards the direction of beam propagation, as depicted in Figure 19.

- X is the horizontal direction to the left when looking along the x-ray beam direction
- Y is vertical up
- Z is the direction of beam propagation

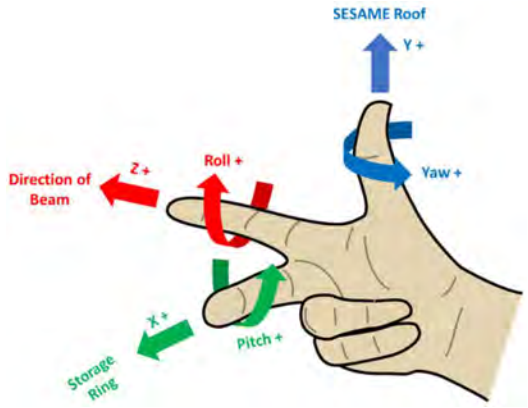

Figure 19: Coordinate system for the TDR.

8.2 Crotch absorber

The crotch absorber is used to protect downstream UHV chambers and front end components from synchrotron radiation emitted by the bending magnets and by the 3-pole wiggler. It is machined from a solid Glidcop bar. Sloped absorbing teeth are made in the lower and upper cooling body of the absorber.

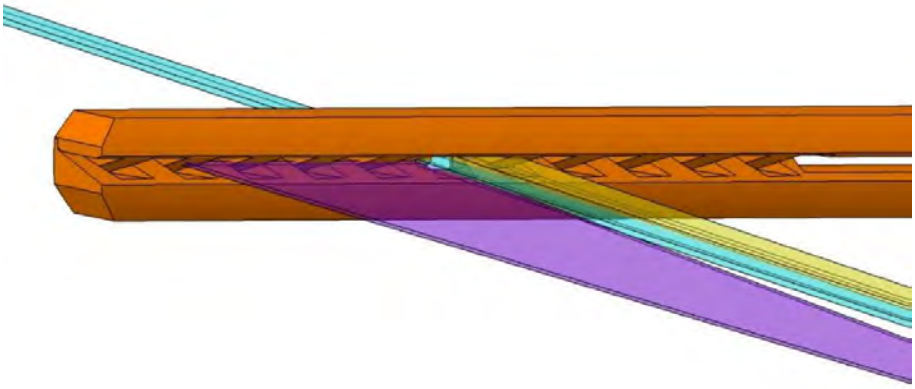

Figure 20: Detailed view of the crotch absorber aperture and teeth absorbing system (Purple and yellow: undesired radiation from dipole magnet, light blue 3-pole wiggler radiation).

Blind cylindrical water channels connected to a concentric water outlet are drilled into the copper body for cooling purposes (Figure 21).

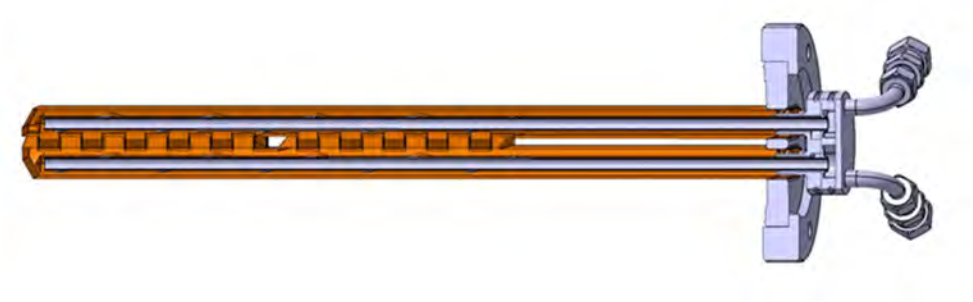

Figure 21: Section view of the crotch absorber with concentric water outlet.

The crotch absorber will have to absorb a total power of 4.17 kW with a maximum power density of 76.6 W/mm2. The radiation from the BEATS source as well as synchrotron radiation emitted by the bending magnets was taken into account for the simulation of the power distribution on the crotch absorber. Figure 22 shows the power distribution of the power absorbed at the crotch absorber

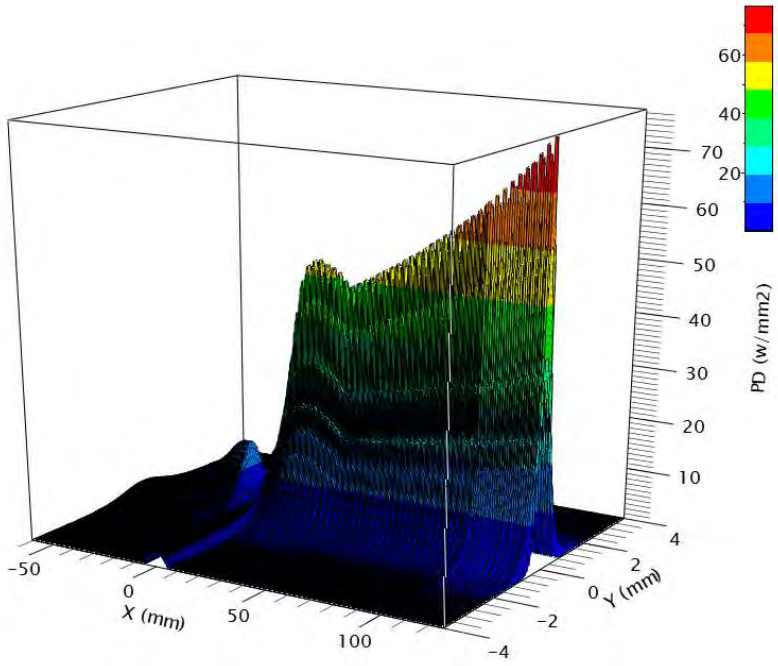

Figure 22: Power distribution of the power absorbed at the crotch absorber.

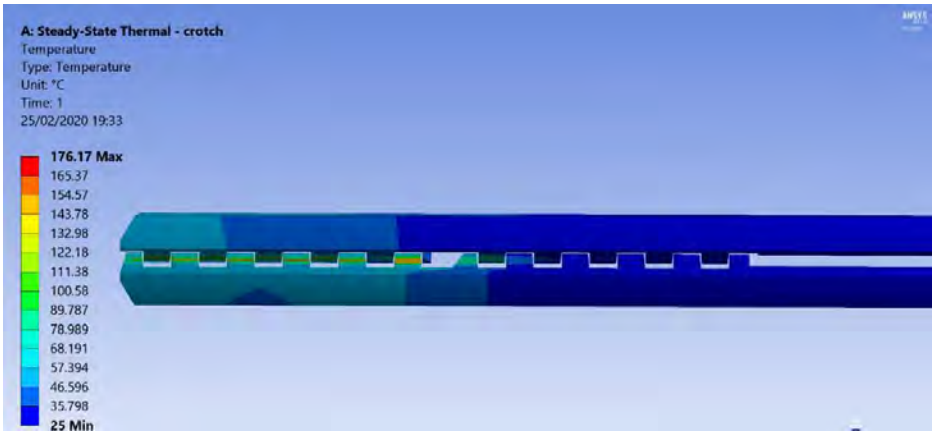

Figure 23: Temperature distribution on the crotch absorber.

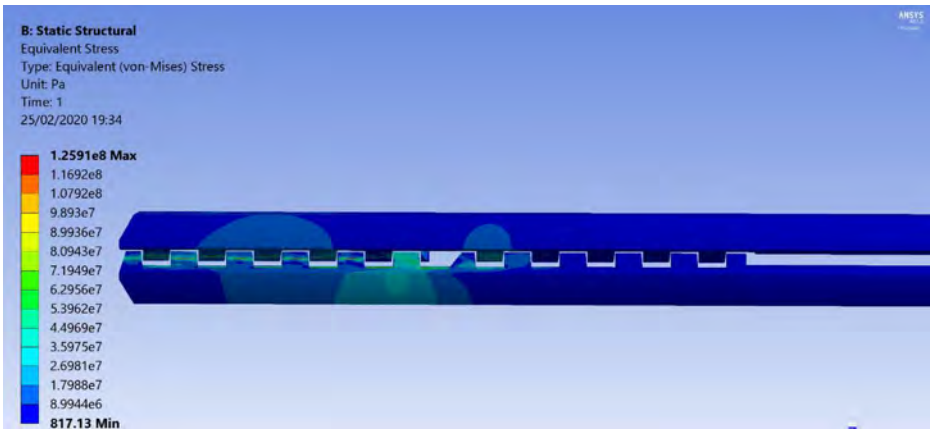

Figure 24 Stress distribution for the crotch absorber during normal operation

Due to the values of temperature and stress reached on this component it must be made of Glidcop or CuCrZr. With one of these materials, both the maximum temperature and the maximum stress are below the failure criteria mentioned above.

8.3 Exit Valve

The exit valve is an all-metal UHV valve, isolating the storage ring from the front end vacuum. Opening this valve is strictly controlled by the SESAME safety procedures.

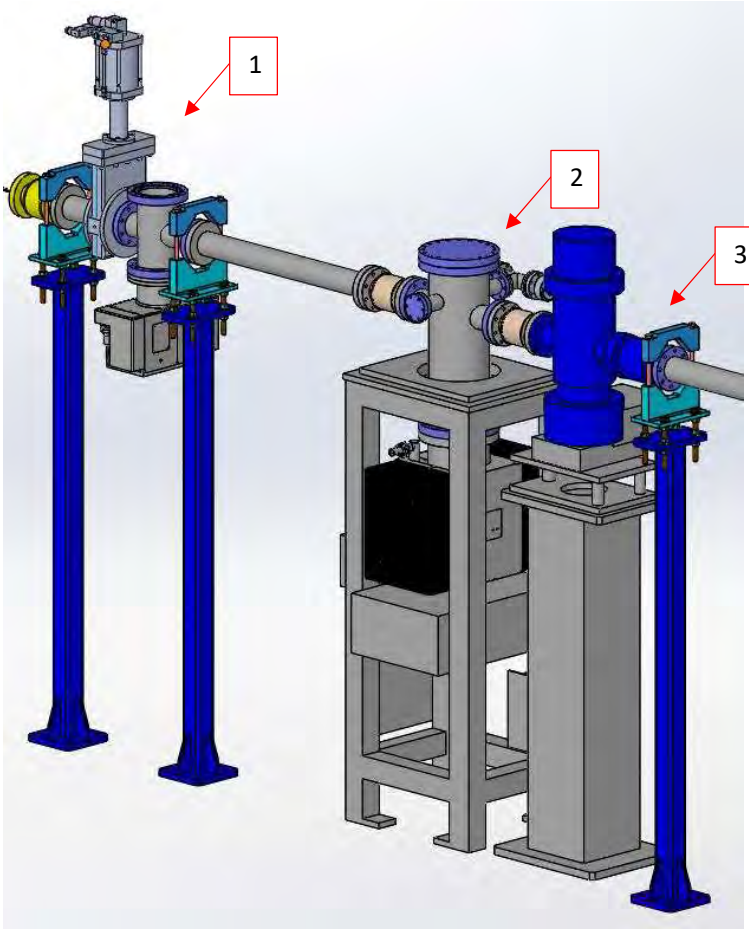

Figure 25: Upstream part of the front end (1: exit valve; 2: pumping unit; 3: XBPM).

8.4 Pumping Unit

Downstream of the exit valve, 2 ion pumps (75 l/min and 300 l/s) will keep the residual pressure in the range of 5 x 10^{-10} mbar. The unit is equipped with vacuum gauges, a square angle valve and a pre-pumping port. The pumping capacity will be sufficient to pump down the outgassing generated by the x-ray beam position monitor (#3 in Figure 25) and by the fixed mask (1.5 in Figure 39).

8.5 X-ray Beam Position Monitor (XBPM)

The XBPM setup consists of an adjustable rigid support structure, a XBPM UHV chamber, a water-cooled XBPM sensor, a motorized X-Y table, and a multichannel electrometer. The adjustable support structure is a rigid steel column prepared for sand filling. It has to include a manual adjustment mechanism that allows the alignment of the X-Y table including the XBPM vacuum chamber in terms of transversal position, pitch, roll and yaw with respect to the support column.

The beam position monitor itself is mounted inside the movable UHV chamber. The base flange of the sensor must be equipped with at least three holders for alignment fiducials which are to be referenced with respect to the photon beam axis between the sensor blades. The motorized X-Y table will allow the horizontal / vertical displacement of the XBPM chamber in a plane perpendicular to the incoming photon beam.

In general, a XBPM sensor uses up to four blades, whose narrow front edges are oriented towards the radiation source, to sense the off-axis radiation of the photon source and to provide an on-line determination of the position of the centre of the photon beam in horizontal and vertical direction using the emitted photoelectron current from the four blades. As BEATS will have a photon source with a large horizontal divergence and thus beam size, we intend to use a **S**taggered **P**air **M**onitor (SPM) configuration, which is only sensitive in the vertical direction (Peatman and Holldack 1998). A scheme of this type of sensor is shown in Figure 26. The size, geometry, and material of the blades must be adapted to the BEATS beam characteristics in order to achieve the maximum photocurrent yield together with an optimized sensibility, position accuracy and linearity. The material of the blades will consist of tungsten or another UHV compatible material. This optimization of the XBPM design is part of the system specification of the front end call for tender and will be left to the successful bidder.

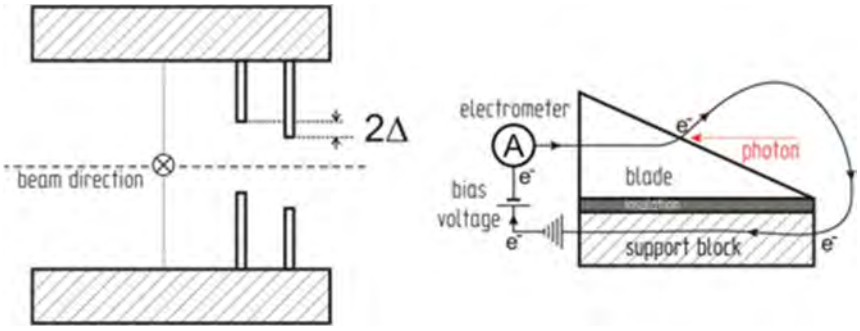

Figure 26: XBPM in Staggered Pair Monitor (SPM) configuration. Δ: vertical offset between the two pairs of blades.

The cooling system of the XBPM and the mechanical layout of its sensor head components exposed to the photon beam must be designed to withstand the associated thermal load.

The connection of the XBPM blades to the multichannel electrometer will be made through Triax cables and connectors in order to allow biasing the blades with a voltage of up to 1kV.

The two axes of the X-Y motion table are to be provided with electrical limit switches (NC type) so that the motors are interlocked, preventing the movements from going beyond the maximum mechanical range. In addition, as a further safety measure, mechanical hard stops are required in order to prevent any damage in case of failure of the electrical limit switches. Each actuator must be equipped with a linear encoder of appropriate resolution and a reference homing position. The encoders used must be radiation-resistant both regarding the associated electronics as the materials used for the encoder's internals (i.e. a glass encoder ruler is not acceptable).

8.6 Fixed Mask

This water-cooled element defines the maximum aperture available for the beamline and reduces the heat load on all the beamline components installed downstream.

It absorbs undesired radiation from the bending magnets passing through the crotch absorber window and limits the size of the beam originating from the 3-pole wiggler. It has an OFHC copper body placed

inside a 63CF flange (ELETTRA design), is cooled by water channels and reduces the angular acceptance to 1 mrad (h) and 0.36 mrad (v), while the crotch absorber aperture accepts 3 mrad horizontally.

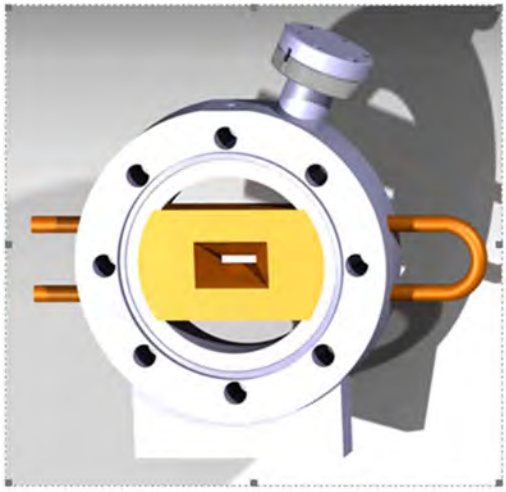

Figure 27: 3D model of the fixed mask.

The horizontal and vertical edges, made of OFHC copper, are sloped and define a central aperture with dimensions of 7.4 mm (h) x 2.7 mm (v). X-ray beam profiles at 8 keV and 20 keV are shown in Figure 28. One can see that once the fixed mask is properly aligned, the vertical aperture of 0.36 mrad allows to accept the useful part of the photon beam.

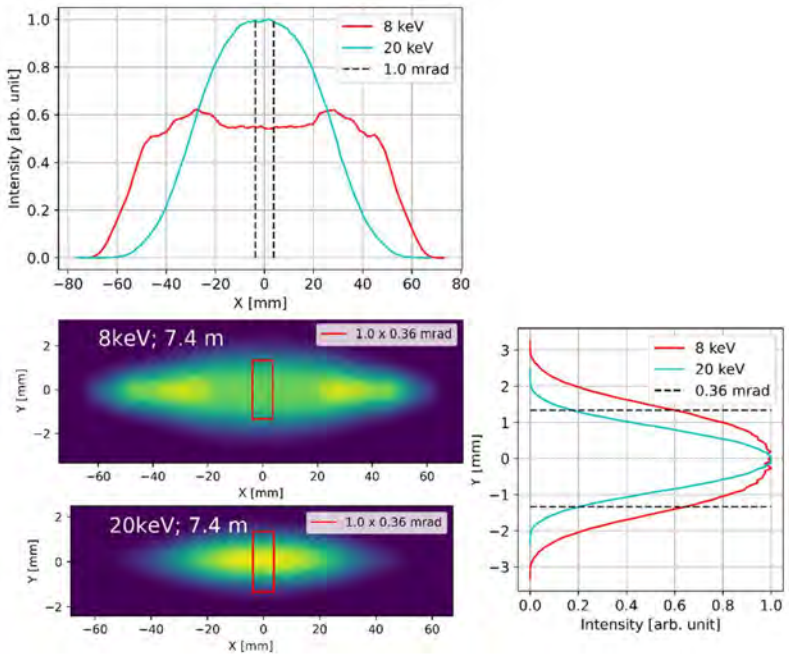

Figure 28: Beam snapshots and profile plots at the position of the fixed mask (7.416 m from source) for the minimum working energy of 8 keV and for 20 keV. Red boxes in figure illustrate the 1.0 mrad (h) x 0.36 mrad (v) aperture of the fixed mask. The crotch absorber is not considered for these simulations in order to visualize the lobes of low-energy radiation produced by the side poles of the 3PW. Due to their large horizontal divergence, only a small portion of the photons emitted by the side poles of the BEATS source will enter the beamline at the fixed mask. The negative effect of a multiplication of the photon source will therefore have a negligible effect at the position of the experiment.

The fixed mask receives a total power of 230 W transmitted by the crotch absorber and will absorb 167 W with a maximum power density of 4.5 W/mm^2. Figure 29 shows the power distribution of the absorbed power at the fixed mask.

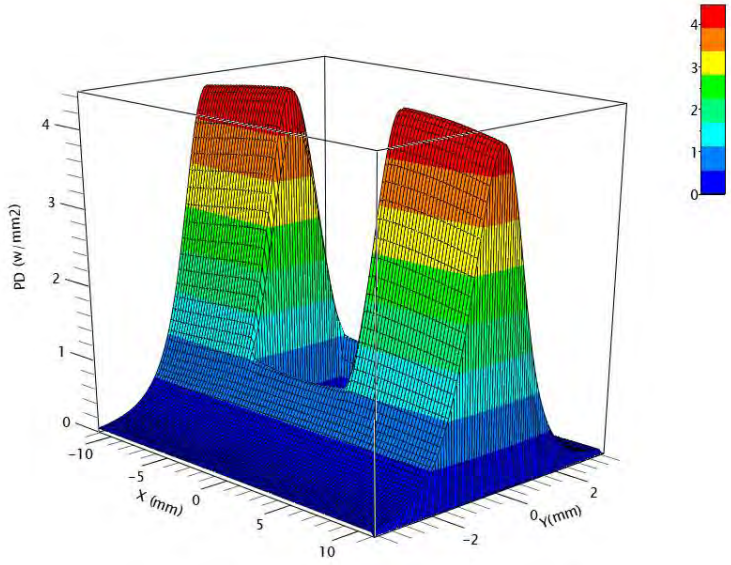

Figure 29: Power distribution of the absorbed power at the fixed mask

The results of the thermal and mechanical stress analysis of the fixed mask are shown in Figure 30 and Figure 31.

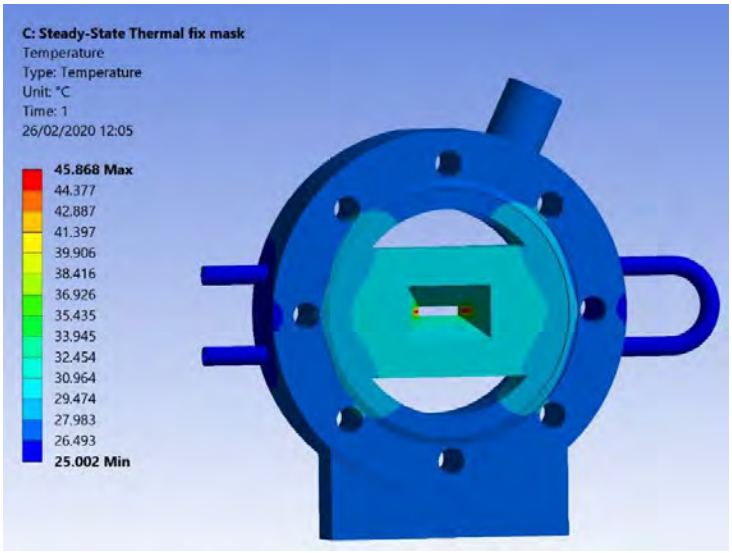

Figure 30: Temperature distribution on the fixed mask during normal operation.

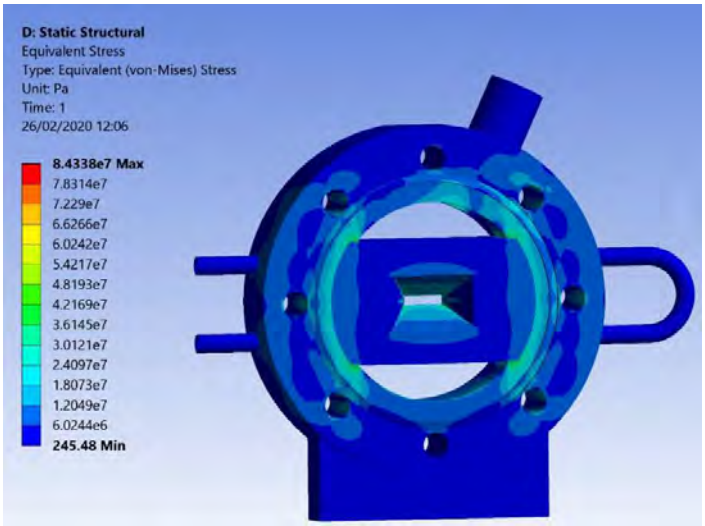

Figure 31: Stress distribution on the fixed mask during normal operation.

8.7 Photon Shutter Assembly

This component (#2 in Figure 39), made of OFHC copper, is designed to completely intercept the X-ray photon beam and isolates the downstream components from the source. A fast-acting mechanism ensures the fast closure of the shutter.

The photon shutter also acts as a safety device to protect the vacuum fast shutter (#2 in Figure 39) from the direct beam. Therefore, the photon shutter is interlocked to the "closed" position of the vacuum fast shutter. The fixed mask and the photon shutter shall be mounted one next to the other on a common support, which will also provide pumping capacity and vacuum level measurement in order to absorb and monitor local outgassing caused by radiation.

When both the photon shutter and the bremsstrahlung stopper (#3 in Figure 42) are closed, the optics and experimental hutch can be accessed safely. For safety reasons, a temperature measurement near the impact point on the photon shutter is needed. Initially, a design by ELETTRA was foreseen (cf. BEATS deliverable D3.3), for technical reasons it was then decided to utilize the design from ALBA, shown in Figure 32 as the basis for the BEATS Front end. Figure 33 and Figure 34 show the distribution of absorbed power, temperature and stress for the blade.

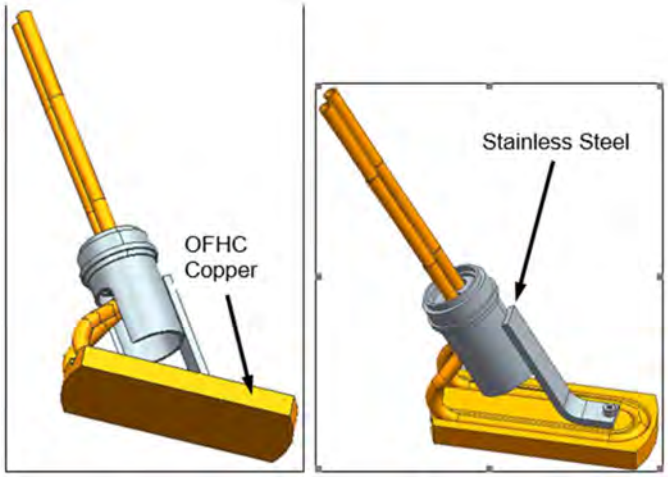

Figure 32: Water-cooled OFHC photon absorber (Courtesy ALBA)

The shutter blade will receive a total power of 63 W with maximum power density of 4.53 W/mm^2, which had been transmitted by the fixed mask.

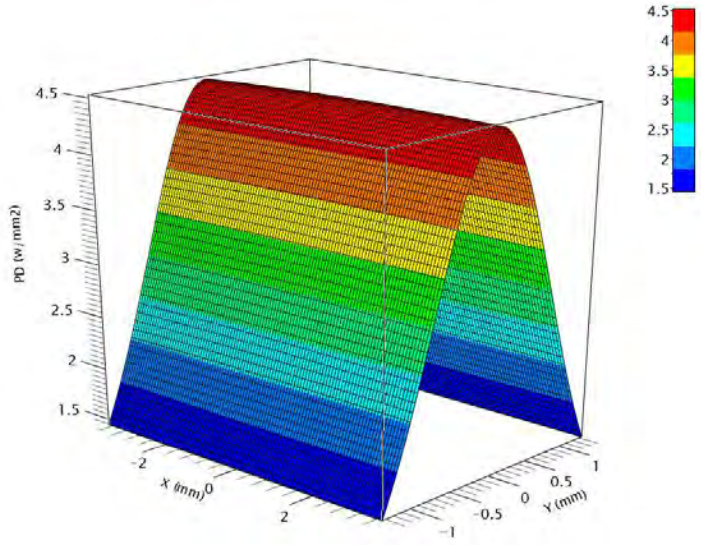

Figure 33: Power distribution of the absorbed power at the shutter

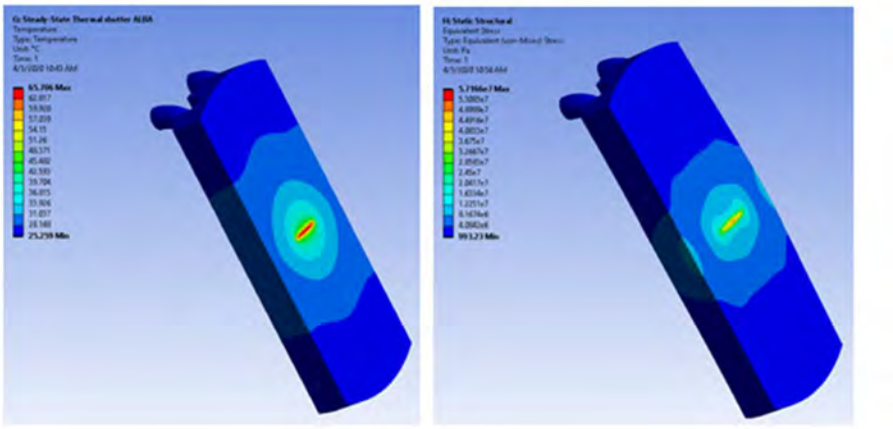

Figure 34: a) Temperature distribution b) Equivalent stress distribution for the photon shutter.

8.8 Vacuum Fast Shutter

The vacuum fast shutter (#3 in Figure 39) protects the vacuum of the storage ring from eventual vacuum accidents occurring on the beamline. Two trigger gauges controlling the actuation of this element are installed on the beamline side in the trigger unit (#1 in Figure 44). This shutter valve closes in 10 ms (for a maximum aperture of 35 mm (h) x 50 mm (v) embedded in a CF63 flange). The vacuum fast shutter acts as a conductance restriction system but is not vacuum tight. To guarantee the full isolation of the upstream section, an additional standard gate valve (closing time ~4 s, located in the Photon Shutter assembly) is also actuated, when the vacuum fast shutter closes.

8.9 Primary Slits

The interaction of the beam with diagnostics and other components, produces scattered radiation. This undesired radiation, together with off-axis radiation, must be absorbed by a cooled slits system. In addition, the slits can be closed in order to adapt the beam size to the needs of the experiment, for

instance, to generate a secondary source of coherent radiation. Finally, when the DMM is used at grazing angles that do not allow the reflection of the full beam height due to the finite length of the substrates, the primary slits are used to vertically reduce the beam to the maximum useful size and to avoid over-shining.

The blades (2 horizontal and 2 vertical), are motorized by independent actuators. The blades and their holders are made of tungsten alloy and copper, respectively, and allow for the dissipation of the heat generated by the white beam.

A safety margin must be foreseen to account for accidental exposure of a single blade to the full direct beam.

Figure 35 presents the ELETTRA design of a blade that will be used at BEATS, Figure 36 depicts the FEA calculation of temperature and stress distribution.

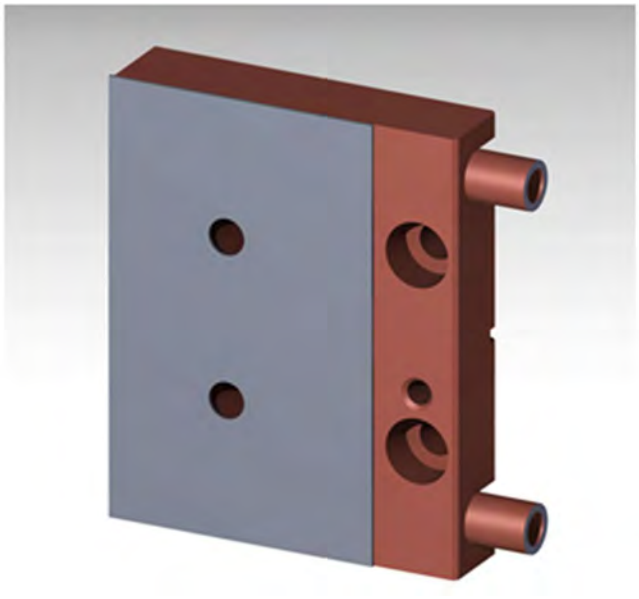

Figure 35: 3D model of the horizontal slits' blade.

In the simulation it is foreseen that a single horizontal blade (more critical than the vertical) absorbs, in normal operation, half the power of the beam (31.5 W).

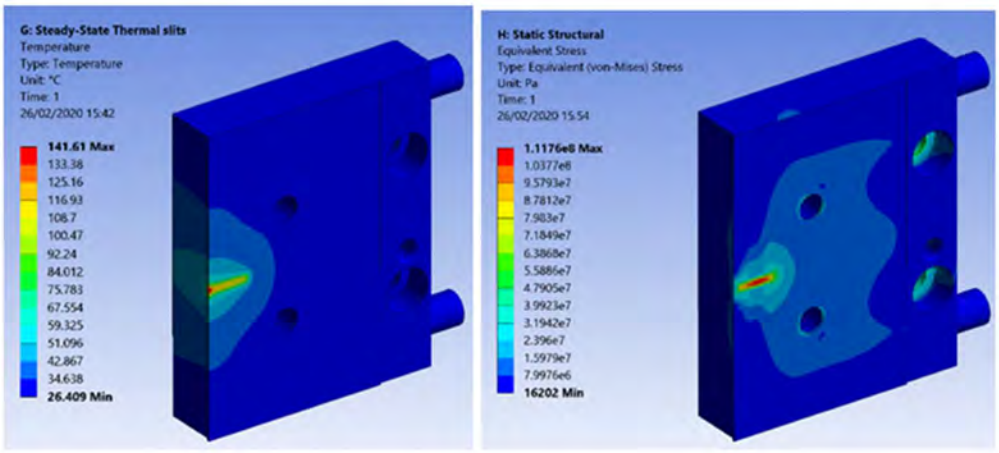

Figure 36: a) Temperature distribution b) stress distribution for a blade interception ½ of the full power.

Under these conditions, the maximum temperature, the maximum wall temperature and the values of the von Mises stress are clearly below any critical value.

In case a single blade absorbs the full beam (heat load 63.5 W), the temperature and stress values for the tungsten alloy blade, the copper holder and the pipe walls are well below any safety limit (Figure 37).

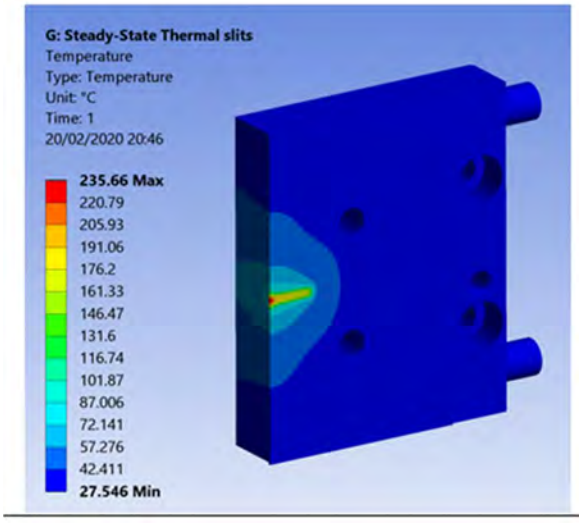

Figure 37: Temperature distribution for the slits blade and a full power of 63.5 W.

Alternatively, the primary slits system of ESRF's beamline ID19 (which will be exchanged in 2020 to cope with the increased power after the EBS upgrade) might be refurbished and used in the BEATS beamline. The ESRF ID19 primary slits can be opened to 20 mm horizontally and 4.5 mm vertically. At the location of the BEATS primary slits (located 8.364 m from the source, #4 in Figure 39), and for the BEATS beamline aperture presented above, the maximum white beam size will be 9.4 mm (h) × 3.2 mm (v). These OFHC slits (see Figure 38) have been designed to sustain a heat load of up to 2490 W).

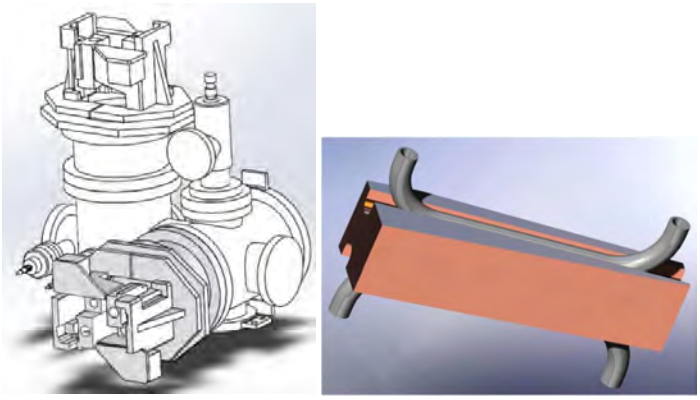

Figure 38: ESRF beamline ID19 primary slit system and OFHC blade model

8.10 First Window

It is mandatory to isolate the SESAME storage ring UHV-sector which in normal operation reaches vacuum values in the 10^{-10} mbar range, from the front end and the beamline vacuum (typically 10^{-8}-10^{-9}mbar). Likewise, there must be no effect of an eventual vacuum leak on the beamline to the storage ring. Consequently, a window, designed to sustain atmospheric pressure on the beamline side, will be installed (#5 in Figure 39). A water cooled **C**hemical **V**apour **D**eposited (CVD) diamond window will be used. For easy maintenance, the window must be placed between two UHV valves and must have vacuum pumps on both sides.

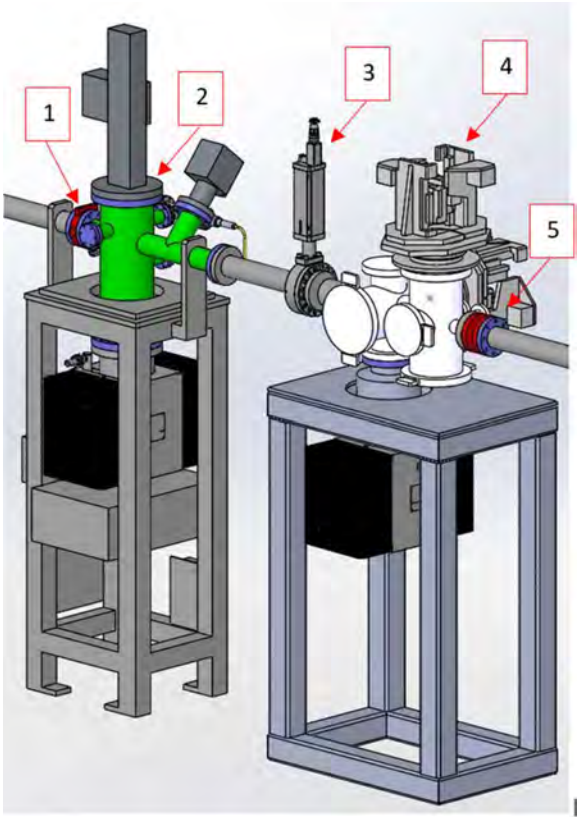

Figure 39: Second part of the front end (1: fixed mask; 2: photon absorber; 3: vacuum fast shutter; 4: primary slits; 5: first window)

The first window is positioned at 9.0 m from the photon source. At this location, the white beam has a maximal extension of 9.6 mm (h) x 3.2 mm (v) (Figure 40). A window with an opening of 11 mm (h) x 5.5 mm (v) and a thickness between 150 µm and 400 µm (to be determined in consultation with the manufacturer) is considered. The surface roughness of the CVD must be low (e.g. < 5nm Ra) to conserve the flatness of the beam front.

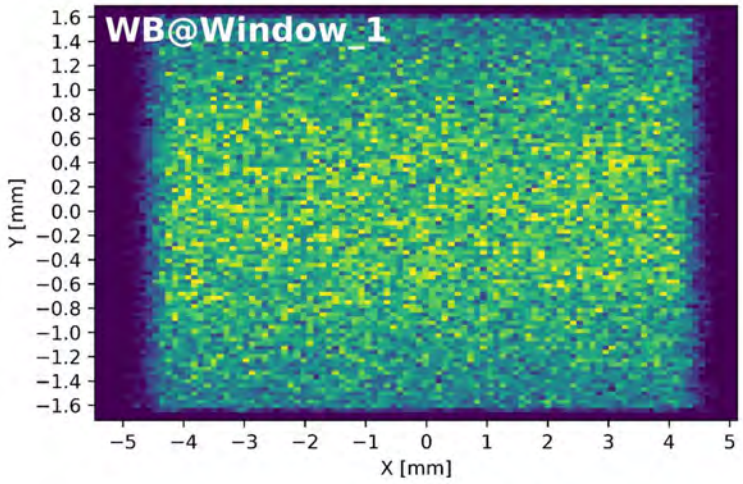

Figure 40: White beam snapshot at 9.0 m from the source.

The CVD window is brazed on a copper body with cooling channels embedded in the flange. It absorbs an average power of 18 W with a maximum power density of 0.68 W/mm^2 for a thickness of 0.4 mm of diamond. Figure 41 shows the power density distribution on the first CVD window.

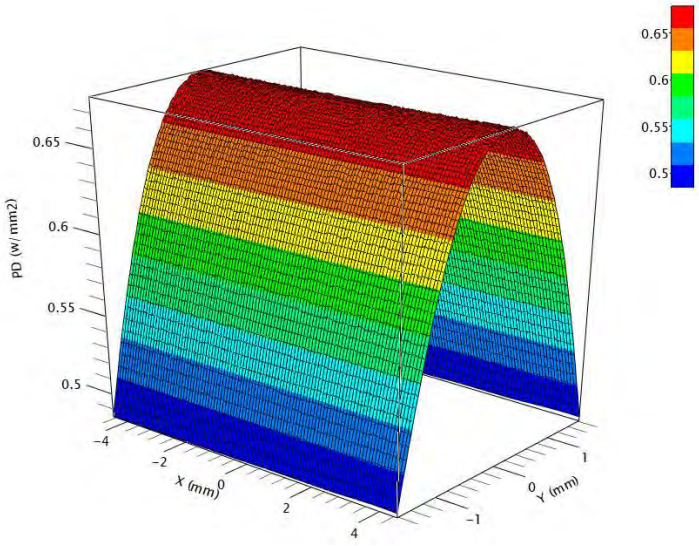

Figure 41: Distribution of the absorbed power on the first CVD window

According to these parameters, finite element simulations showed a maximum temperature of the diamond of 30.3 °C, and maximum von Mises stress of 84 MPa due to thermal deformations and pressure gradient.

If a static pressure difference of 1 bar is applied on the faces of the window (no thermal load, 0.4 mm thickness), the maximum computed stress is found to be around 2 MPa (to be compared with the flexural strength of the diamond which is 137 MPa), causing a deflection of 2 10^{-9} m.

8.11 Attenuator

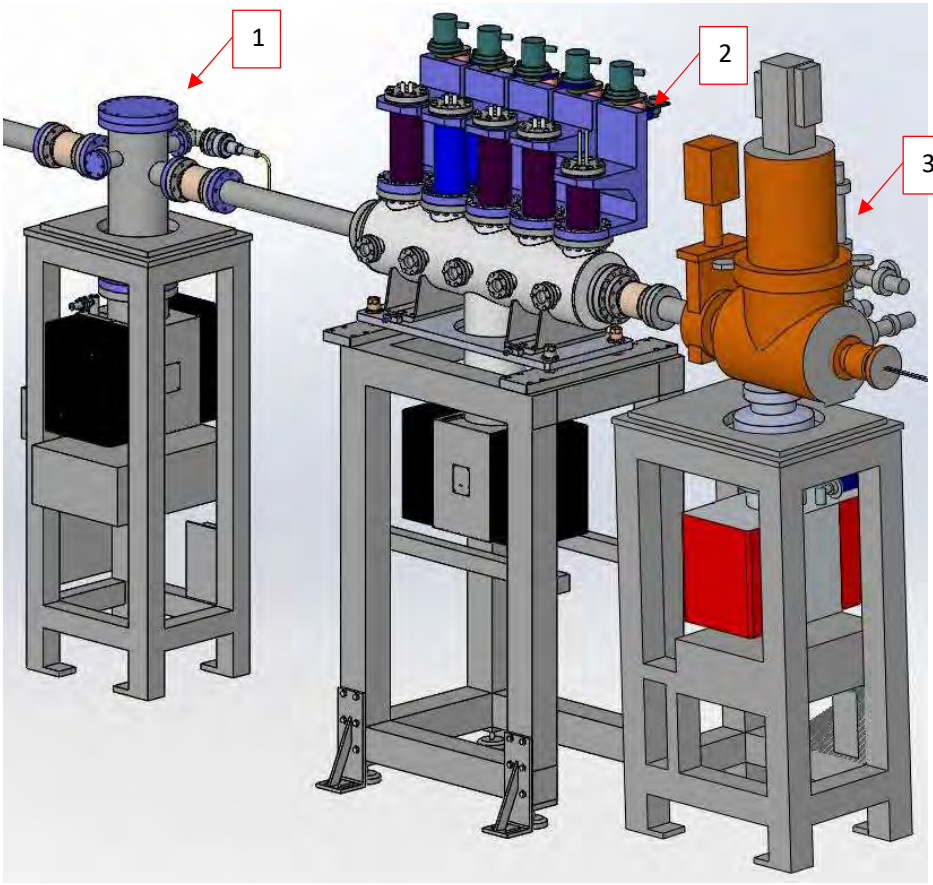

Figure 42: Third part of the front end (1: pumping station (a right angle valve can be included below the chamber); 2: attenuator; 3: bremsstrahlung stopper)

The attenuator consists of a mechanical assembly allowing to insert foils made of different materials and thicknesses into the beam in order to tailor the spectrum according to the needs of the experiment. Aluminium, copper, iron, graphite and palladium are preliminarily considered as attenuating materials. Cooling will be provided by channels around the filter frame (see Figure 43, right).

Frames holding the individual filter foils will be inserted in or moved out of the beam by actuators moved by stepper motors. The attenuator vessel will be connected to an ion pump and must be compatible with standard beamline vacuum. A control system based on switches will allow to monitor the position of the individual filter foils.

The attenuator assembly considered for BEATS is based on the attenuator designed for the ESRF beamline BM18, comprising 5 axes, for a total of 15 foils of attenuating material. For BEATS, the number of axes could be reduced to 3. The position of each filter axis can be controlled either with position switches or with encoders and limit switches. The maximum aperture of the device should leave space for a 13.2 mm (h) × 4.2 mm (v) beam at the position of the attenuator.

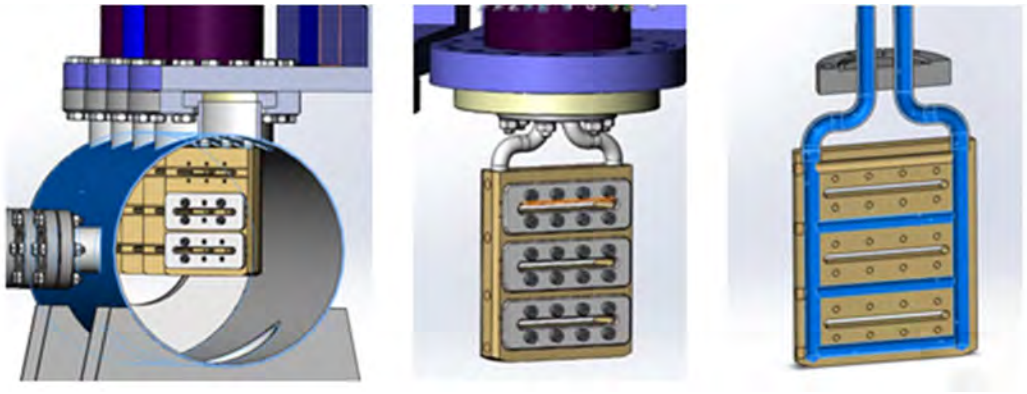

Figure 43: Details of the attenuator system design for BM18 at the ESRF. (Courtesy: F. Cianciosi)

8.12 Bremsstrahlung Stopper

This stopper absorbs bremsstrahlung radiation from scattering from the particle beam in the residual gas of the straight section. The stopper is made of an UHV uncooled compatible tungsten alloy block (or lead enclosed in a stainless-steel tight envelope), it must not be exposed directly to the photon beam. Therefore, the upstream photon shutter is interlocked with this bremsstrahlung stopper.

When the stopper is closed, it will completely intercept the radiation cone originating from the upstream components. It will be moved by a pneumatic actuator into the working position.

The bremsstrahlung stopper must be closed during each electron storage ring injection to absorb the bremsstrahlung produced. In addition, the photon-bremsstrahlung stopper assembly is closed every time the downstream optics hutch is accessed.

8.13 Conclusions about thermal and stress assessment for white beam

For a complete description of the front end thermal analysis the reader should refer to BEATS deliverable 3.3, “Front end thermal analysis”.

The thermal and stress analysis indicates that all front end components, under normal operation as well as under extreme (worst case) conditions, have a reliable thermal design and are compliant with safety requirements. Furthermore, results are far from failure criteria including a large safety margin.

Further thermal and stress analyses for all front end components (incl. attenuators) will be carried out once the “as-built” drawings of the components will be provided by the manufacturers, and before the production phase.

8.14 Design and motorization in the Front End

Table 4 presents the front end equipment with details on the number of motorized axes as well as the design (or supply) responsible for each component.

Equipment	N. of axes	Along axis	Encoder required	Comment	Design used at
Crotch Absorber				No motion	SESAME
Pumping Unit				No motion	
X-ray Beam Position Monitor	2	X/Y	Yes		ALBA
Fixed Mask				No motion	ELETTRA
Photon Shutter	1	Y	No	Pneumatic	ALBA
CVD window				No motion	
Primary Slits	4	X/X/Y/Y	Yes		ESRF
Attenuator	5	Y/Y/Y/Y/Y	Position Switches / Encoders		ESRF
Bremsstrahlung Stopper	1	Y	No	Pneumatic	ALBA

Table 4: Front End equipment with information on motorized or pneumatic components.

9 Optics

The principal optical component of the BEATS beamline will be a **D**ouble **M**ultilayer **M**onochromator (DMM). This will tune the beamline energy deflecting the beam vertically over two multilayers coated on Si substrates. The optics hutch of BEATS (Figure 44) will host the DMM and will be positioned outside of the SESAME storage ring.

Having the DMM outside of the storage ring in addition to proper photon and bremsstrahlung stoppers before the storage ring wall as described above presents the following advantages:

- Allow commissioning and maintenance of the DMM (and in general to enter the optics hutch) during normal operation of the storage ring: it is not necessary to shut down the storage ring to access the DMM.
- Reduce maintenance costs and risks due larger space surrounding the DMM available.
- Increase encoders lifetime, since these are less exposed to radiation.

The DMM will leave the possibility to operate the beamline in filtered white beam mode. When in use, the DMM will deflect the beam vertically by an offset between 6 and 20 mm, depending on the energy. All components (e.g. pipes, stopper…) after the DMM will be large enough to cope with the offset between monochromatic and pink beam.

Apart from the DMM, the optics hutch will contain a trigger unit equipped with a wire monitor, a beam viewer and a combined photon-bremsstrahlung stopper (Figure 44 and Table 10).

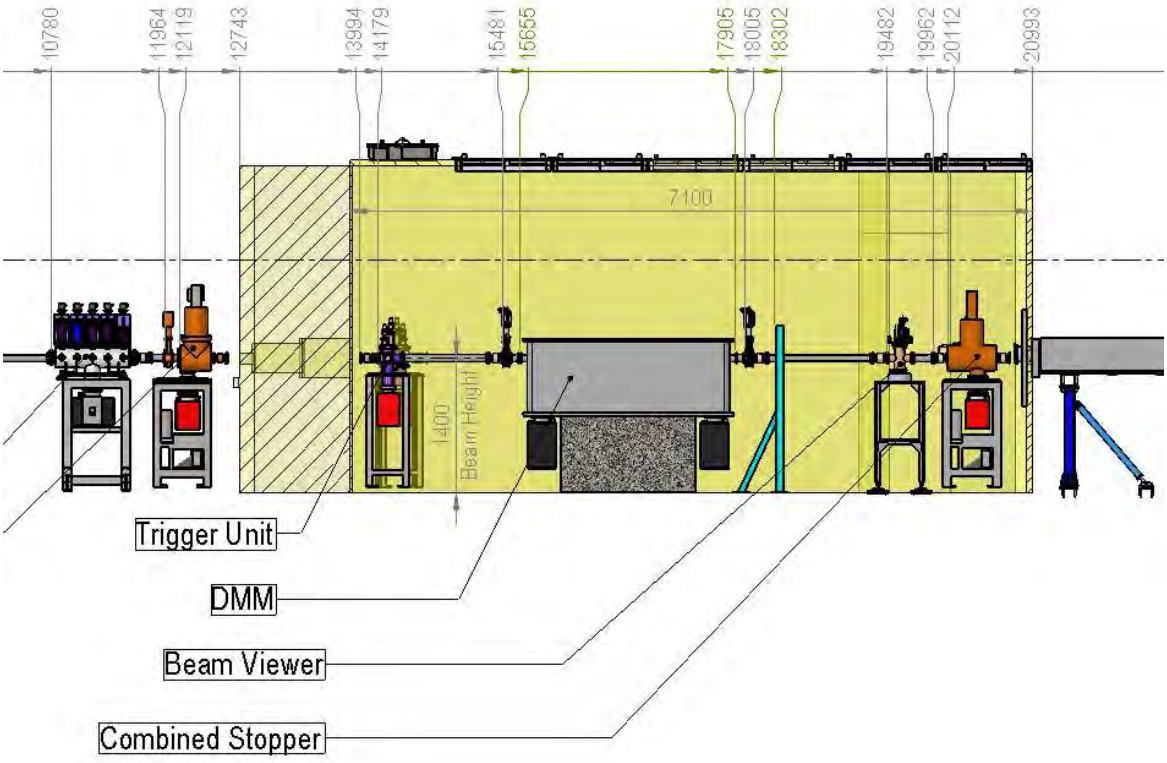

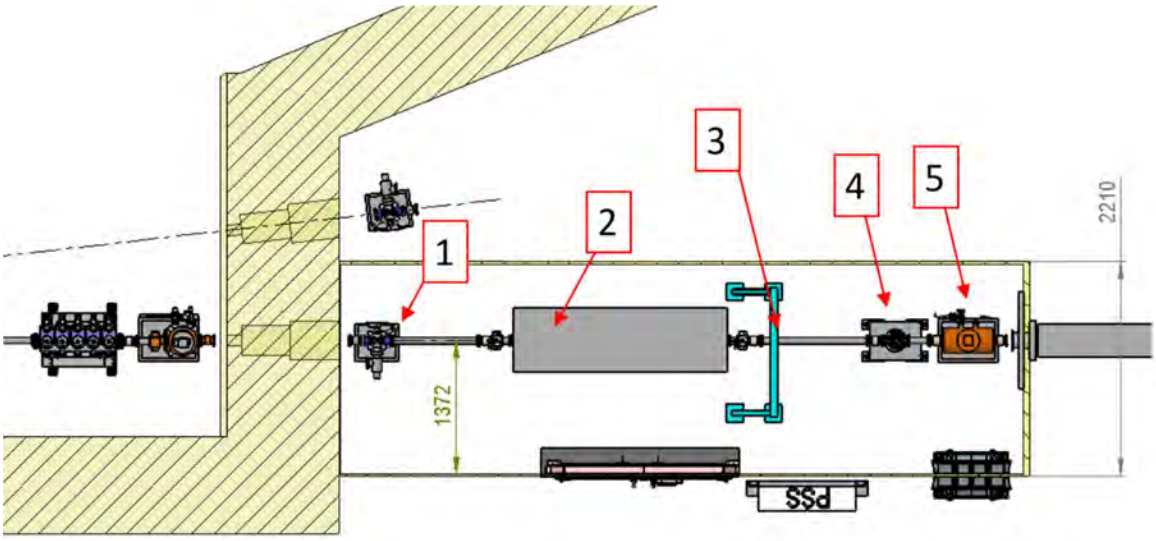

Figure 44: BEATS optics hutch. (1) trigger chamber. (2): double multilayer monochromator. (3) local shielding. (4) beam viewer. (5) combined stopper. The final shape of this hutch might change after revision of the radiation protection raytracing calculations and inclusion of local shielding for scattered radiation and polyethylene for neutrons. Constraints imposed by the steel frame of the hutch (not shown in this figure) during commissioning of the DMM shall be also taken into account.

9.1 Beam defining elements

9.1.1 Trigger Unit

A trigger unit is installed in the optics hutch as the first element. It provides pumping capacity, vacuum readings and allocates at least one of the two trigger gauges to activate the vacuum fast shutter (#3 in Figure 39).

In addition to that, the trigger unit will host a **Wire Scanner Monitor**, this monitor consists of a tungsten wire that is driven through the beam by a motorized actuator in order to scan it and obtain the profile and intensity of the beam.

9.1.2 Beam viewer

A beam viewer is necessary to check the beam position and visualize the beam profile at the end of the DMM. An example of beam viewer (ESRF design, courtesy F. Cianciosi) is shown in Figure 45. The beam viewer consists of a screen (generally diamond or a scintillating material such as cadmium tungstate or yttrium aluminium garnet) driven by a motorized actuator. The screen is imaged by an optical system composed by an objective lens and a CCD camera. Depending on the material chosen for the screen and on the expected heat load, the beam viewer will be operated only for monochromatic beam (in case of a fluorescent screen unable to resist the pink beam heat load is installed) or for both pink and monochromatic beam. In addition, for a multilayer monochromator with variable offset, the beam viewer should be usable over the whole offset range.

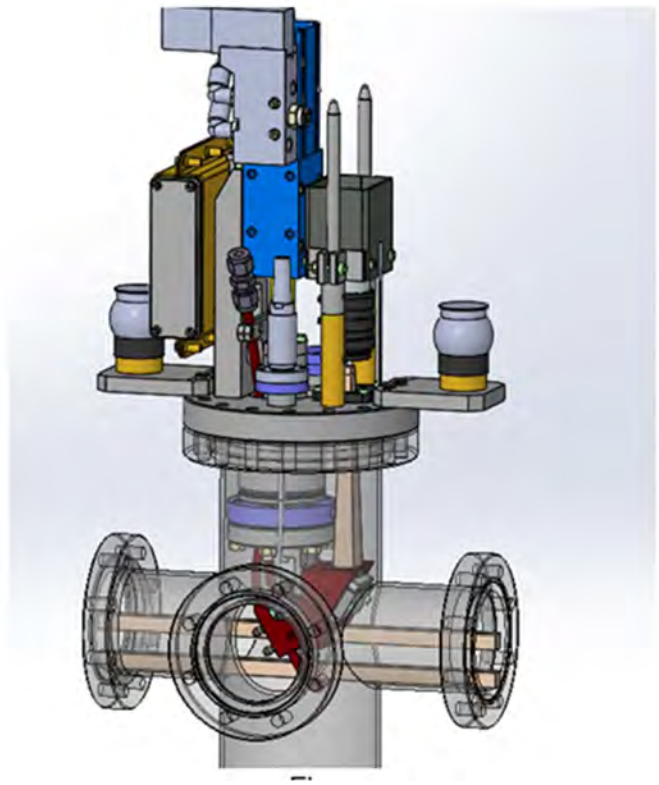

Figure 45: ESRF beam viewer. Image courtesy of F. Cianciosi

9.1.3 Combined stopper

In order to allow access to the experimental hutch while keeping the monochromator under heat load, a combined stopper will be used, with both the functionality of bremsstrahlung stopper and photon shutter.

The combined stopper assembly will be placed downstream from the monochromator in the optics hutch.

9.1.4 Shielded transfer pipe

To ensure a proper shielding around the transfer line connecting the optics and experimental hutch, two schemes are possible. Either a wrapping of lead sheets around the stainless-steel pipe, or a tunnel fixed on a rigid structure. The latter one is often a cheaper solution than the first one as it allows to modulate easily the different thicknesses of lead (thicker at the entrance of the pipe). This solution is presented in Figure 46. The thickness of the lead shielding required for the transfer pipe is determined by the radiation protection raytracing simulations (cf. chapter 12). For safety reasons, the transfer pipe might have no pump installed.

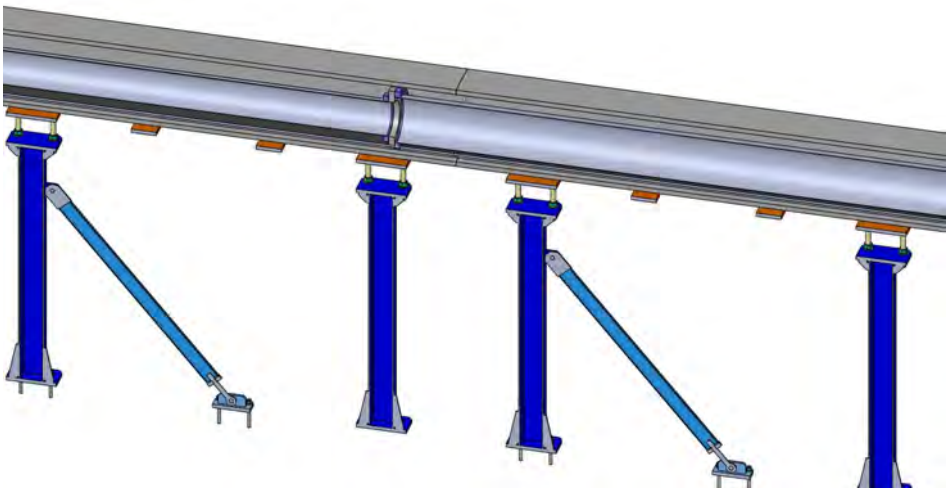

Figure 46: section of the shielded transfer pipe showing the lead casing enclosing transfer pipe and relative flanges. The image shows the central position of the transfer line where the pipe diameter increases from CF150 to CF200.

9.2 Monochromator

The BEATS DMM will be located at approximately 15.5 m from the source.

The choice of multilayers and the DMM design considered the following principles and constrains:

- **Operating photon energy:** 8 – 50 [keV] Working energies below 8 keV are deprecated due to the predominant effect of radiation emitted by the side poles of the 3-pole wiggler which would triplicate the point of photon emission. In addition, photon energies below 8 keV are heavily attenuated by the minimum set of windows (diamond or beryllium) of the beamline.
- **Resolution:** dE/E between 2 and 4 [%].
- **Vertical deflection** of the beam.
- **Preserve beam height:** the effective length of the multilayer coating should allow to reflect as much as possible the full beam height for the working incidence angles of the DMM.
- **Preserve homogeneity, flatness and coherence of the reflected beam:** high-quality substrates should be used. The choice of materials should also consider as much as possible preservation of the beam flatness (A. Rack et al. 2010; 2011).
- **Allow pink beam operation:** The motion of the two multilayers should allow complete retraction of both mirrors from the beam path when BEATS is operated in filtered white beam mode.
- **Selection between two stripes:** The device must be designed to allow the installation of substrates with two stripes of different multilayer coatings. The motion (horizontal translation perpendicular to the beam path) of the multilayer stages must allow to switch between different stripes.

9.2.1 Choice of multilayer coatings

The performance (integrated reflectivity after two reflections, R^2(int)) of several multilayer choices is shown in Figure 47 for the energy range required for BEATS (Ch. Morawe 2020). B_4C was chosen for the low-Z material since it is well-known and widely used at imaging beamlines. All simulations were performed considering a constant d-spacing of 2.0 nm, a Γ factor of 0.5 and a number of layers maximizing R^2(int). Despite the absorption L-edge of tungsten at 12100 eV, W/B_4C shows the best performance over a wide energy range. W/B_4C is a widely used, stable combination of materials. W/B_4C will be the coating of choice for the first stripe of the BEATS DMM.

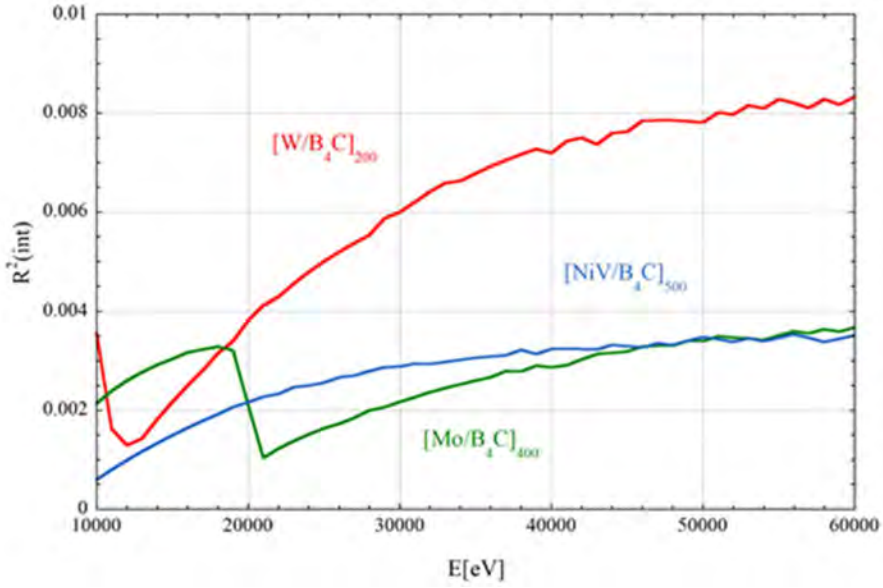

Figure 47: Integrated reflectivity after two reflections from multilayers of different composition. d-spacing: 2.0 nm. The integrated reflectivity R^2(int) is calculated as the product of the peak reflectivity after two reflections R^2(peak) and the bandwidth (dE/E) of the system. Courtesy of Dr. Christian Morawe.

9.2.2 Multilayer properties

The choice of the multilayer d-spacing follows a compromise between multilayer reflectivity, resolution and the resulting incidence angle in the working energy range. The latter determines the available beam height and the precision required for of the motion (particularly the pitch) of the mirrors.

This paragraph presents a comparison between the performance of three W/B_4C multilayers with d-spacing of 2.5 nm, 3.0 nm and 4.0 nm. All multilayers were simulated in XOP with a Γ factor of 0.5 and number of layers maximizing R^2(int). Roughness values of 3.0, 3.1 and 3.3 Å were considered for the Si substrate, W and B4C layers, respectively. As shown in Figure 48C, a 4 nm d-spacing multilayer ($[W/B_4C]_{30}$) provides higher integrated reflectivity (and thus flux), mainly due to a broader energy band-pass (Figure 48B).

Figure 49, Figure 48A show the incidence angles for the operation of W/B_4C multilayer of 2.5 nm, 3.0 nm and 4.0 nm d-spacing. The resulting beam height available at a sample position of 43 m is shown in Figure 49B.

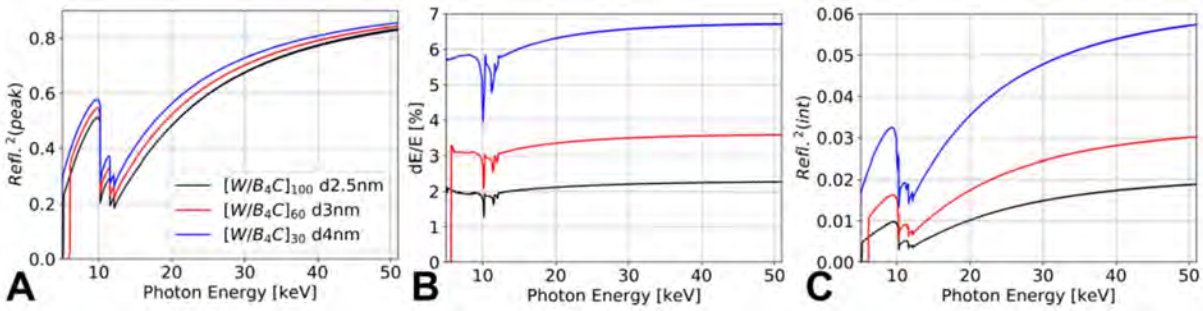

Figure 48: (A) Peak reflectivity of W/B_4C DMMs with different d-spacing. (B) Energy resolution. (C) Integrated reflectivity after two reflections.

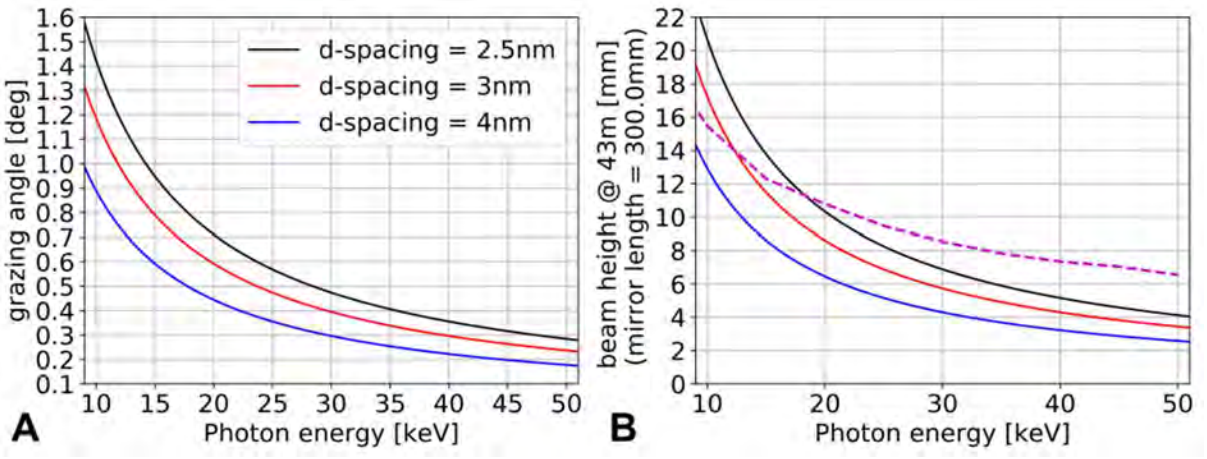

Figure 49: (A) incidence angles for the operation of three DMMs with different d-spacings. (B) Beam height available at a sample position of 43 m. A coated mirror length of 300 mm was considered. The dashed line in magenta shows the comparison with the beam height (FWHM) available at the corresponding energy without the DMM.

For the purpose of fast and efficient tomography the maximum possible beam height should be utilized. For this reason, even if larger d-spacings maximize the integrated reflectivity, these are deprecated due to the reduction of the beam height. The first stripe of a DMM for BEATS should host a W/B_4C coating with 2.5 nm d-spacing and between 80 and 100 bilayers. This solution represents a compromise between reflectivity with 2% to 3% energy resolution and maximum preservation of the beam height.

The roughness of the substrate and of each coating should be minimized and not exceed 3.0 Å (RMS). 300 mm-long coatings were considered for this document. If available, high-quality, longer substrates would allow to increase the exploitable beam height.

The actual incidence angle will vary along the longitudinal position on the multilayer mirror. In order to reflect at constant wavelength over the entire mirror length, the d-spacing can be controlled during deposition to vary longitudinally according to an appropriate gradient. For 300 mm mirror length and a d-spacing of 2.5 nm, a d-spacing gradient of 1.86% is foreseen (Christian Morawe 2019).

9.2.3 Second DMM stripe

A second pair of multilayer stripes can fulfil one or both of the following purposes:

- **Maximize the photon flux** at the expense of energy resolution and available beam height. For this, a second W/B_4C coating with larger d-spacing (4 nm) is considered. As shown in Figure 50B, a $[W/B_4C]_{30}$ multilayer with 4 nm d-spacing increases the integrated reflectivity (as well as the bandwidth of the reflected radiation) by a factor of 3. Due to the lower incidence angle, the use of this stripe is likely limited to a narrower (and lower) energy range.
- **Operation of the beamline in the low energy range:** two possibilities are considered for this scenario: a $[Mo/B_4C]_{100}$ coating with 3.0 nm d-spacing and a $[Ru/B_4C]_{65}$ with d-spacing = 4 nm. The expected performance (resolution and integrated reflectivity) of these coatings is shown in Figure 50. Both combinations of materials are widely used at imaging beamlines. For operation at low energies, the d-spacing can be increased to 4 nm if no particular requirement on the energy resolution is present. The $[Ru/B_4C]_{65}$ combination yields a slightly larger range of working energies, offering a good overlap with the energies covered by a W/B_4C stripe.

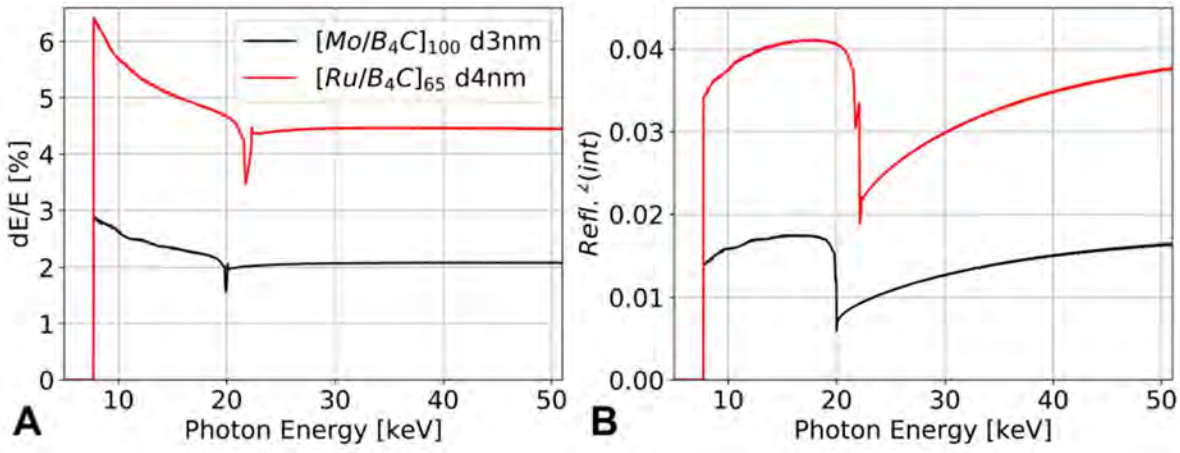

Figure 50: (A) Energy resolution of two DMMs for operating BEATS at low energies. (B) Integrated reflectivity after two reflections.

The properties and performance of the two multilayer coatings proposed for BEATS are summarized in Table 5.

		Stripe 1	Stripe 2	
Substrate		Si	Si	Si
Material 1		W	W	Ru
Material 2		B_4C	B_4C	B_4C
d-spacing		**2.5 nm**	**4 nm**	**4 nm**
N. bilayers		**100**	**30**	**65**
Refl.^{2} (peak) @	**15 keV**	0.33	0.42	0.82
	30 keV	0.67	0.72	0.67
	50 keV	0.82	0.83	0.85
dE/E @	**15 keV**	2.02 %	6.02 %	5.01 %
	30 keV	2.10 %	6.55 %	4.46 %
	50 keV	2.30 %	6.67 %	4.46 %

Table 5: Properties and performance of the two multilayer coatings proposed for BEATS

9.2.4 Operation of the DMM and design parameters

The operation of the BEATS DMM with **two multilayer stripes (2.5 nm and 4 nm d-spacing) and a usable coating length of 300 mm** is demonstrated in this paragraph. incidence angles from simulations with XOP for both stripes and for some reference energies are shown in Table 6.

Stripe	**d-spacing**	**Incidence angle [deg]**				
		8 keV	20 keV	30	40	50
$[W/B_4C]_{100}$	2.5 nm	1.8186	0.7283	0.48565	0.36434	0.29151
$[Ru/B_4C]_{65}$	4.0 nm	1.159	0.4635	0.30901	/	/

Table 6: Incidence angles for the two multilayer stripes

A fixed offset of 10 mm is considered in the first instance. Stripe 1 of the BEATS DMM ($[W/B_4C]_{100}$; 2.5 nm d-spacing) can cover energies between 18 keV and 50 keV (0.809° – 0.284° incidence angle) with a stroke of the second mirror between a minimum of 363 mm and 1.01 m maximum (Figure 51A). Alternatively, the maximum stroke of the second mirror can be limited by decreasing the DMM offset when operating at low incidence angles. This is shown in Figure 51B for the operation with the 2.5 nm d-spacing stripe between 29 and 50 keV: a reduction of the offset to 6 mm allows to reduce the stroke

of the second multilayer to about 600 mm. The entire beamline downstream of the DMM is therefore shifted vertically.

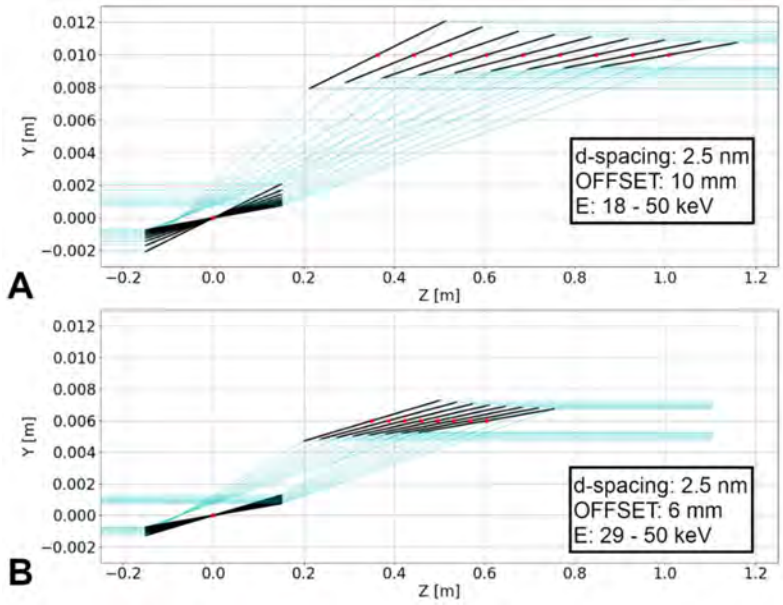

Figure 51: Mirrors position for different working energies with STRIPE_1 of the BEATS DMM. (A) 2.5 nm d-spacing; 300 mm long effective coatings. This stripe ([W/B4C]100) can cover a broad energy range (18 - 50 keV) while keeping a fixed offset of 10 mm. (B) A reduction of the maximum stroke of the second mirror is obtained reducing the DMM offset when low incidence angles are needed.

For low energies, a second stripe with larger d-spacing is considered. Figure 52A shows DMM mirror positions of 4 nm d-spacing coatings and working energies between 8 and 29 keV). The offset can be increased in order to reduce the risk of collision between the two mirrors at the lowest energies, see Figure 52B).

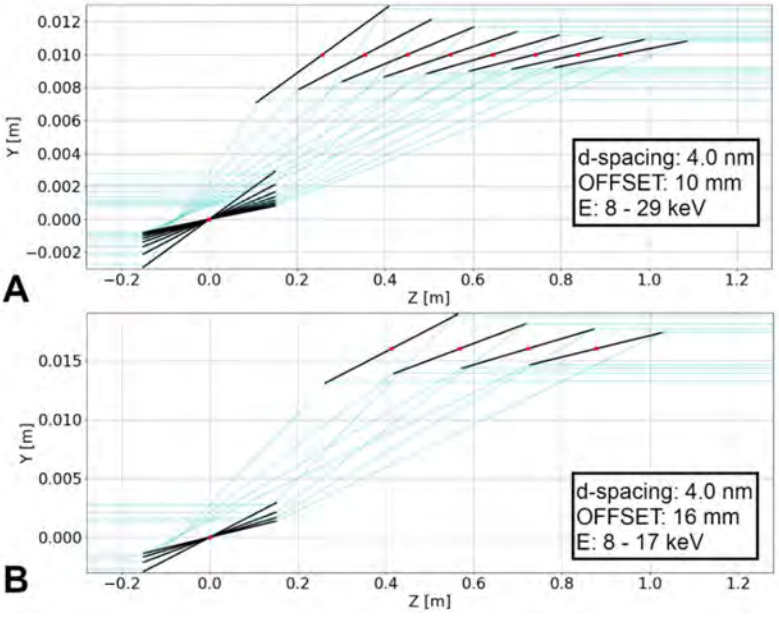

Figure 52: Mirror positions for different working energies with STRIPE_2 of the BEATS DMM. (A) [Ru/B_4C]$_{65}$; 4 nm d-spacing, 300 mm long coatings. Energies between 8 and 29 keV are covered with a fixed offset of 10 mm. (B) The risk of collision between the mirrors is minimized by increasing the DMM offset at the low energies.

Working with a multilayer with thicker d-spacing reduces the incidence angle and the distance between the reflectivity peak and the edge of total reflection (Figure 53). When the second stripe of the BEATS DMM (4 nm d-spacing) is utilized, low energies must be attenuated by appropriate filters.

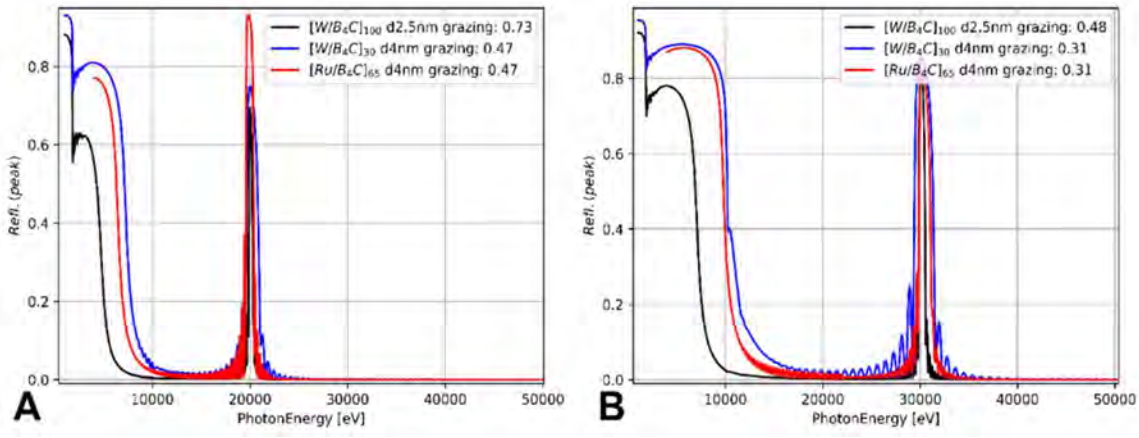

Figure 53: Plot of the multilayer peak reflectivity at working energies of 20 keV (A) and 30 keV (B). $[W/B_4C]_{30}$ and $[Ru/B_4C]_{65}$ stripes with d-spacing of 4 nm require low incidence angles. As a result, a broader portion of the low energy spectrum is going through total external reflection of the DMM. Low energies must be suppressed by attenuators in this case.

9.2.5 Footprints and power density on the first mirror

Figure 54 shows the expected footprint on the first multilayer mirror of the BEATS DMM. 2.5 nm and 4 nm d-spacing coatings of infinite length are assumed. The footprint at working energies of 8 keV, 20 keV and 50 keV for 2.5 nm d-spacing are shown in A, B and D, respectively. Figure 54C shows the footprint at 20 keV when a multilayer stripe with d-spacing of 4 nm is used. The beam and DMM properties used for the calculation of the footprints of Figure 54 are listed in Table 7.

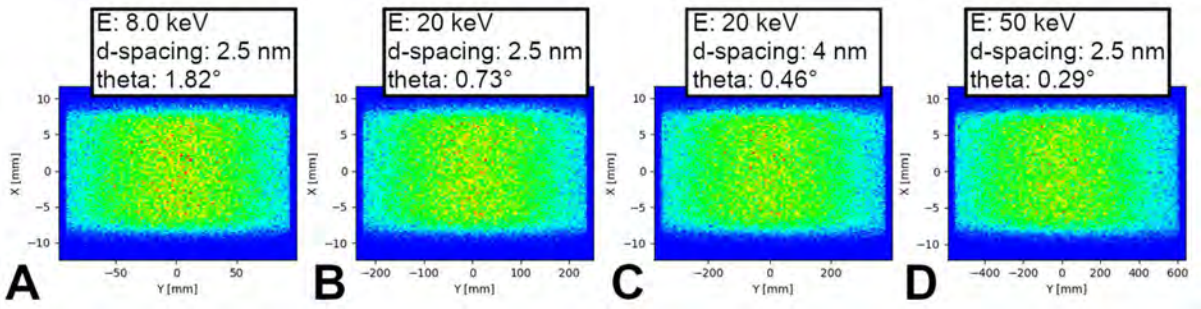

Figure 54: Footprints on the first DMM mirror for different working energies and coating d-spacing. 5 – 60 keV source simulated in ShadowOui. A 0.2 mm-thick diamond window and infinite coating dimensions are considered for the simulations.

Nominal beam divergence (defined by fixed mask aperture)	1.0 × 0.36 (H × V) [mrad]			
Mirror 1 distance from source [m]	16.155			
Substrate dimensions	infinite			
Energies [keV]	8	20		50
d-spacings [nm]	2.5	2.5	4	2.5
Theta (incidence angle) [deg]	1.8186	0.7283	0.4636	0.2916
Footprint size X (FWHM) [mm]	~ 17.5			
Footprint size Y (FWHM) [mm]* *percentage of the footprint intercepted by a 300 mm-long mirror given in brackets	150 (100%)	360 (83%)	565 (53%)	912 (33%)
Mirror dimensions	infinite			

Table 7: summary of the beam and DMM properties and of the mirror positions considered for footprint calculations.

We have calculated the total power absorbed by the 1st and 2nd type of multilayers for two cases, at maximum and minimum incidence angle. The worst-case scenario for the 1st multilayer will be at the maximum incidence angle and for the 2nd multilayer will be at lowest incidence angle.

At maximum incidence angle the 1st multilayer will absorb 45.3 W with a maximum power density of 0.0236 W/mm^2.Water-cooled copper plates installed at the substrate's side will dissipate the power absorbed by the first multilayer. Figure 55 shows the power density along the beam footprint at the 1st multilayer.

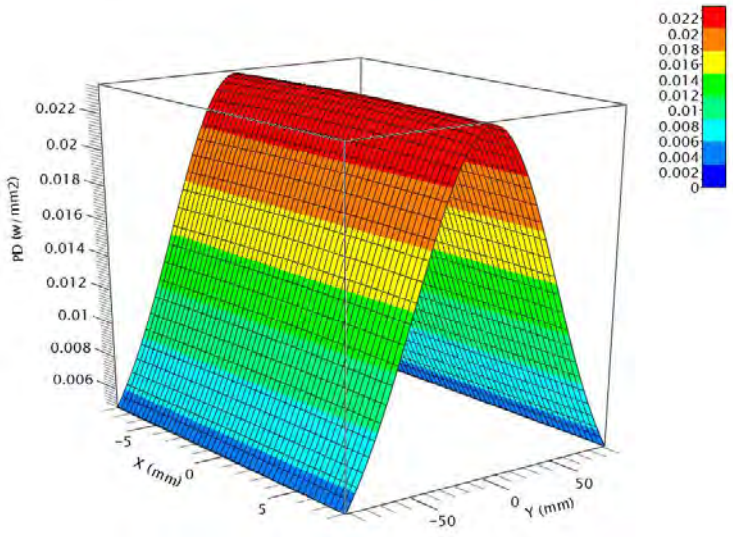

Figure 55: Power distribution of the absorbed power at the 1st ML @ 1.8 deg incidence angle

For the 2nd multilayer the worst-case scenario will be at a minimum incidence angle of 0.2915 deg. In this position the multilayer will absorb 2.5 W with maximum power density of 0.00052 W/mm^2. Figure 56 shows the power density along the beam footprint at the second multilayer.

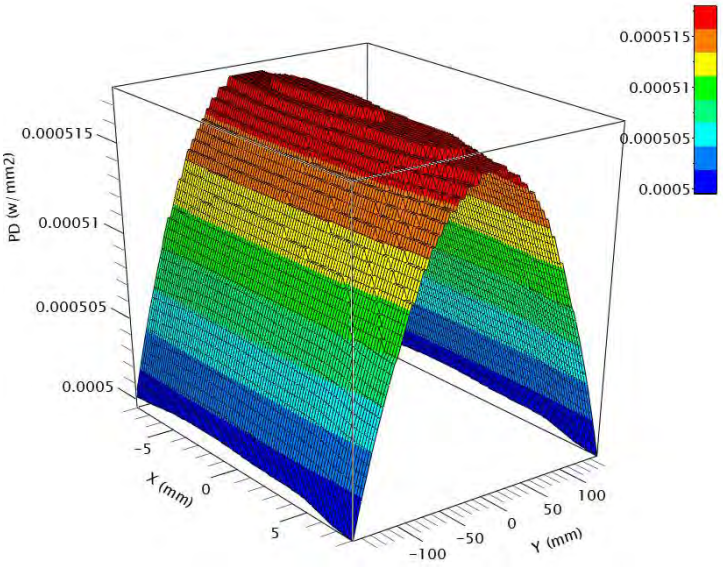

Figure 56: Power distribution of the absorbed power at 2nd ML @0.2915 deg incidence angle

9.2.6 Design and manufacturing parameters

The main design specifications of the BEATS DMM are summarized in Table 8.

Offset	6 – 16 [mm]
Coating dimension	20 × 300 [mm]
Mirror 2 travel range	(250) 360 – 1010 (610) [mm]

Table 8: Summary of the BEATS DMM design specifications.

A massive granite basement and adjustable interface to the ground should provide precise and stable positioning of the DMM during installation. The granite base and the DMM lid should accommodate electrical and hydraulic utilities and leave space for the installation of enough ion pumps. These can be one or two and should guarantee a target vacuum inside the DMM chamber of $5x10^{-8}$ mbar approximately.

Each DMM mirror will be mounted on a dedicated and independent support. For the first mirror, vertical (Y) and horizontal (X, for stripe selection) displacements as well as pitch (Bragg angle) should be motorized and equipped with dedicated encoders. In addition to X, Y and Pitch, the second DMM mirror will be mounted on a motorized Z translation support for the displacement of the mirror along the beam path. The roll angle of the second mirror can be controlled manually or can be motorized. The necessity of a motorized control of the yaw angle of the second mirror is still under evaluation.

The first DMM mirror should be equipped with adequate cooling to dissipate the power density. An active anti-collision control system (software and/or hardware e.g. cameras or inclinometers) can be included to interlock the motion of the mirrors when these are too close.

9.3 Raytracing

The following paragraph illustrates the expected beamline performance of BEATS. Raytracing simulations were performed using XOP (Sanchez del Rio and Chubar 2014) and ShadowOui (L. Rebuffi and Sánchez del Río 2016). OASYS scripts and Jupyter notebooks for the reproduction of the calculations illustrated here are archived on Zenodo (Gianluca Iori 2020) and can be downloaded at the link: https://doi.org/10.5281/zenodo.3988604

9.3.1 Pink beam size at sample

9.3.1.1 Primary slits OPEN (effect of the fix mask)

Binder link for reproducing this paragraph.

Figure 57 shows the beam size inside the BEATS experimental hutch for primary slits open and a fixed mask at 7.428 m from the source with an acceptance of 1.0 mrad × 0.36 mrad (H × V). 1 mrad of horizontal divergence guarantees a horizontal beam size up to 45 mm (enough for all applications foreseen by the BEATS scientific case) while reducing the size of the second CVD. The vertical size of the pink beam available inside the BEATS experimental hutch ranges from approx. 12.5 mm at the entrance through the CVD window in contact with air up to 14 mm at the maximum distance from the source (43 m).

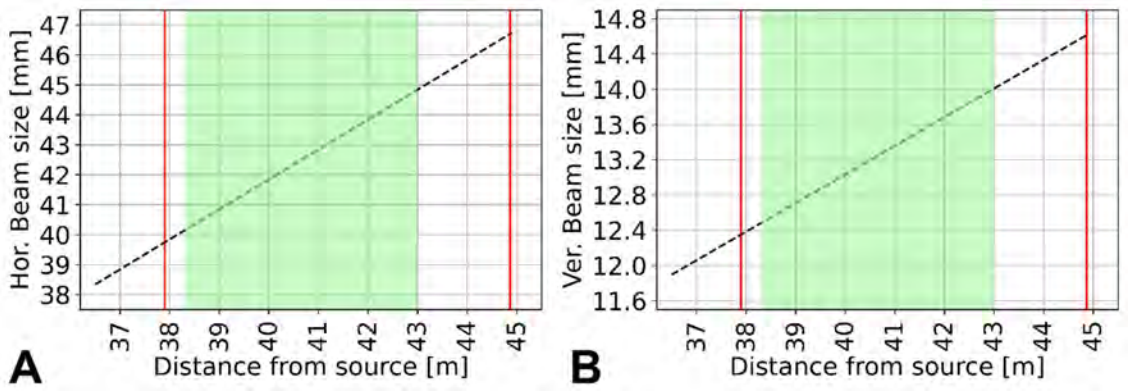

Figure 57: Pink beam size inside the BEATS experimental station (dashed lines). The distance from the photon source can vary between 38.5 m and 43 m (area in green). Red lines indicate the positions of the second window and of a beam stop at the entrance and back of the experimental hutch, respectively. A) Horizontal beam size with primary slits completely open and beamline divergence of 1 mrad defined by the fixed mask aperture. B) Vertical beam size in the experimental station.

9.3.1.2 *Primary slits as secondary source*

Plots of the horizontal beam divergence and of its horizontal size at 43 m from the source are shown in Figure 58 A and B, respectively, when the primary slits in the front end are operated. Dashed lines in Fig. 5 are obtained using Equation 1 for the effective beam divergence, where a secondary source of size a (horizontal aperture of the primary slits) is considered. In Equation 1 , η_x, σ_x and d are the horizontal beam divergence after the slits, the horizontal source size at the centre of the wiggler and the distance between wiggler and slits, respectively.

$$\eta_x = \frac{\sqrt{\left(\frac{\sigma_x}{2}\right)^2 + \left(\frac{a}{2}\right)^2}}{d} \quad (1)$$

Equation 1: Effective beam divergence.

There is a minimum limit to the aperture of the primary slits (approx. 0.5 mm), after which a further closure of the slits does not provide further reduction in horizontal beam size.

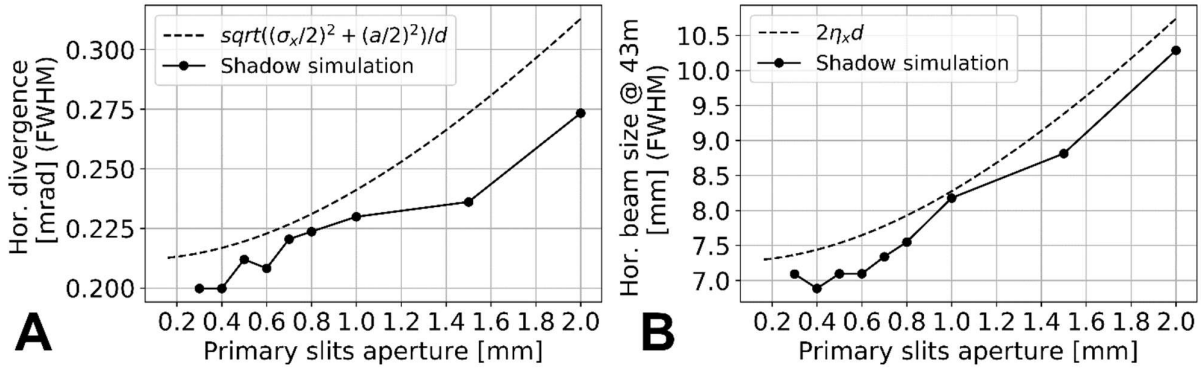

Figure 58: Beam divergence and size with primary slits as secondary source. A) Horizontal beam divergence behind the primary slits when the slits aperture is reduced; comparison between raytracing results from ShadowOui and expected divergence from Equation 1. B) Horizontal beam size @ 43m from the wiggler when the slits aperture is reduced.

9.3.2 Coherence length and blur

9.3.2.1 Primary slits OPEN (fix mask with 1mrad acceptance)

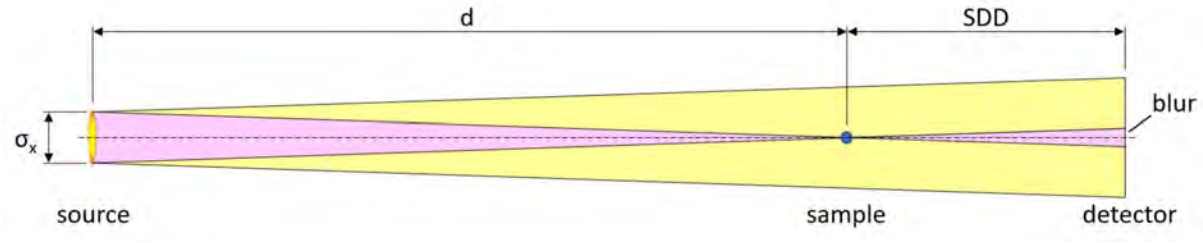

Figure 59: Image blur with a source of finite size. Reproduced from (Cloetens 2007).

Estimations of the transverse coherence length of a photon beam with energy of 20keV at the following synchrotron computed tomography beamlines: ID19 of the ESRF, TOMCAT (SLS), SYRMEP (Elettra) and TopoTomo (former ANKA) are given in Table 9. The transverse coherence length was calculated using Equation 2, where *d* is the distance between source and sample, λ is the wavelength (0.62 Å) and σ_x is the FWHM horizontal photon source size as illustrated in Figure 59 (Pogany, Gao, and Wilkins 1997).

$$l_{\mathrm{coh}} = \frac{2\lambda \mathrm{d}}{\sigma_x} \quad (2)$$

Equation 2: transverse coherence length

Beamline	d [m]	σ_x [µm]	Transverse coherence length [µm]
ID19@ESRF	145	25	720.1
TOMCAT@SLS	34	140	30.2
SYRMEP@Elettra	23	197	14.5
TopoTomo@ANKA	33	500	8.2
BEATS - Primary slits OPEN	43	1978	2.7
BEATS - Primary slits: 1 mm (H)	34.6	1000	4.3
BEATS - Primary slits: 0.5 mm (H)	34.6	500	8.6

Table 9: transverse coherence length at 20 keV. Comparison of BEATS with other tomography beamlines.

9.3.2.2 Primary slits as secondary source

The coherence properties of the beam will be improved by using the primary slits in the front end as a secondary source of reduced size. This configuration for improved transverse coherence will be required in particular for propagation-based application of phase contrast imaging. The expected increase in transverse coherence length of the BEATS beam when progressively closing the primary slits is shown in Figure 60A. At 20 keV, a transverse coherence length of approximately 8 µm is reached when closing the primary slits to a horizontal aperture of 0.5 mm. The corresponding image blur (Equation 3) at varying sample-detector-distance (SDD) is shown in Figure 60B. Red dots in Figure 60 show the comparison with a configuration (ANKA's TopoTomo beamline) in which propagation-based phase contrast imaging is available and has been widely exploited (A. Rack et al. 2009; Weitkamp et al. 2011).

$$blur = \frac{\mathrm{SDD}\ \sigma_x}{d} \quad (3)$$

Equation 3: Image blur.

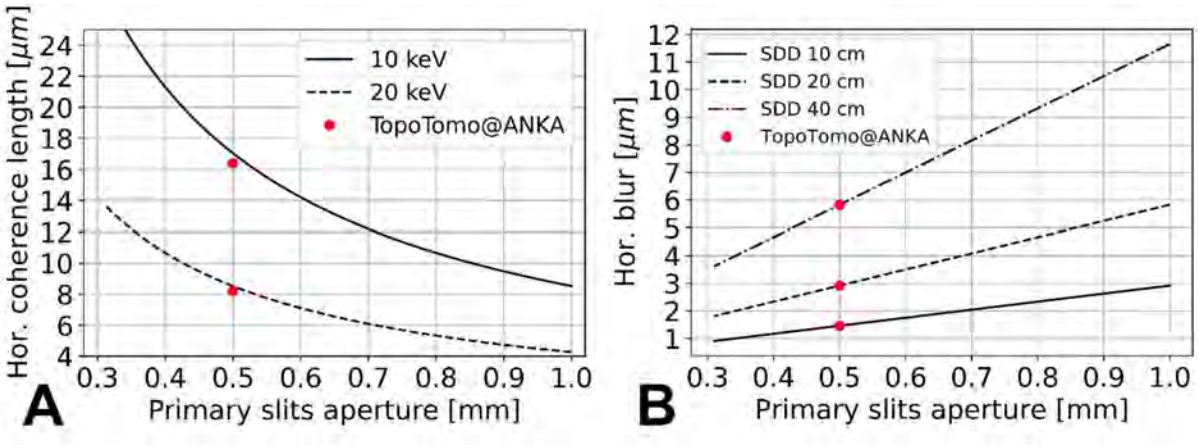

Figure 60: A) Transverse coherence length closing the primary slits for 10keV and 20keV. B) Horizontal image blur closing the primary slits for different sample-detector distances (SDD). Red dots showing the corresponding values calculated for TopoTomo at ANKA (Hor. photon source size: 0.50 mm).

9.3.3 Propagation-based phase contrast imaging at BEATS

The transverse coherence length calculated in the previous paragraph yields a rough estimate of the maximum distance between two object points for which interference effects (edge enhancement and phase contrast) can be observed. At the same time, for a given pixel size Δ and wavelength λ, optimal fringe separation is obtained when the sample-detector-distance is in the Fresnel (near-field) regime at (Willmot 2019):

$$SDD = \frac{(2\Delta)^2}{\lambda} \quad (4)$$

Equation 4: Optimal sample-detector-distance (SDD) for propagation-based edge enhancement. The detector pixel size Δ matches the fringe separation.

The relationship between pixel size, photon energy and optimal propagation distance for propagation-based phase contrast is illustrated in Figure 61. The area of Figure 61 highlighted in green shows the pixel sizes available at BEATS with the detectors foreseen for day-1 operation (see paragraph 10.4). The source spectrum is limited superiorly to around 50 keV, as shown above (see Figure 16). It can be concluded from Figure 61 that the maximum propagation length foreseen for day-1 phase contrast applications at BEATS will be approximately 3 m.

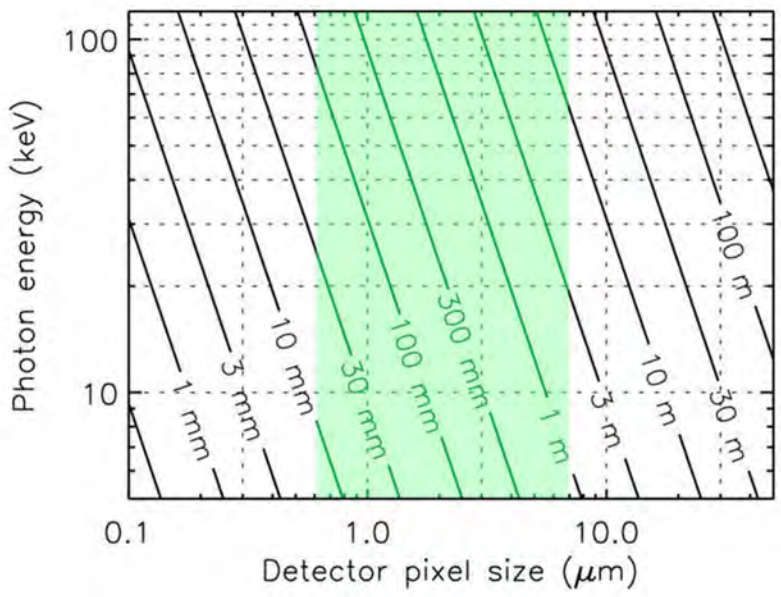

Figure 61: critical propagation length for near-field condition at different photon energies and detector pixel sizes. A propagation length below the critical near-field distance is a necessary condition for propagation-based phase-contrast imaging. The maximum pixel size is constrained by the pixel size of the installed detectors and by the transverse coherence length of the beam at a given energy. In the case of BEATS, a transverse coherence length of 8.6 µm is obtained at 20 keV when the primary slits are closed to form a 0.5 mm pinhole acting as secondary source. With the same slits aperture, the transverse coherence length is 5.7 µm and 4.3 µm at 30 keV and 40 keV, respectively. Closing the slits further is detrimental for the photon flux and does not represent an advantage since the limited beam size (approx. 7 mm horizontally) does not allow to illuminate larger samples, for which larger propagation distances are required. With the portfolio of detectors considered for day-1 operation (see paragraph Detectors below), pixel sizes between 0.65 µm and 6.5 µm will be available (green area in the figure). Accordingly, we expect to perform experiments from day-1 within a maximum sample-to-detector propagation distance of 3 m. Adapted from (Weitkamp et al. 2011).

9.3.4 Flux density @ sample

9.3.4.1 White beam flux density @ sample: primary slits as secondary source

To quantify the effect of a reduction of the primary slits horizontal aperture on the flux density at the sample position we used the OASYS ShadowOui tree of Figure 62. The geometrical beam defining elements of the front end considered are the crotch absorber (3 mrad aperture), the fix mask (1 mrad aperture), and the primary slits.

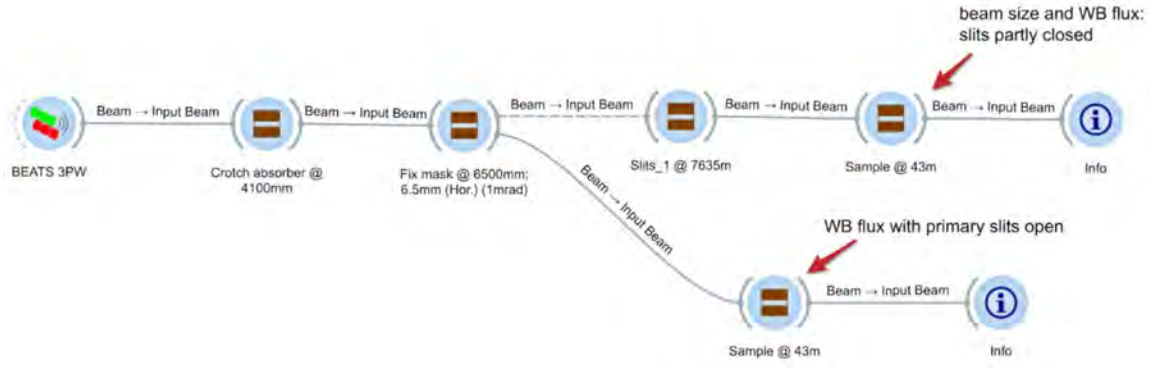

Figure 62: Oasys tree for the calculation of the BEATS white beam spectral flux density through a pinhole at the sample position (43m from source).

The simulation is repeated at different energies, storing each time the intensity (*n. good rays*) of the beam through a pinhole at the sample position. The flux density for each energy is then calculated as:

$$Flux_{\text{WB @ sample}}(eV) = Flux_{\text{XOP}}(eV)\frac{n.goodrays}{Tot.rays} \quad (5)$$

Equation 5: White beam flux on sample

Where $Flux_{XOP}$ is the total flux from an XOP simulation at that photon energy and *Tot. rays* = 5×10^6. The result for three different settings of the primary slits (fully open, 1 mm and 0.5 mm horizontal aperture) are shown in Figure 63. At 20 keV, there is a reduction in the flux density at the sample position of approximately 72% when the primary slits are closed horizontally to 0.5 mm.

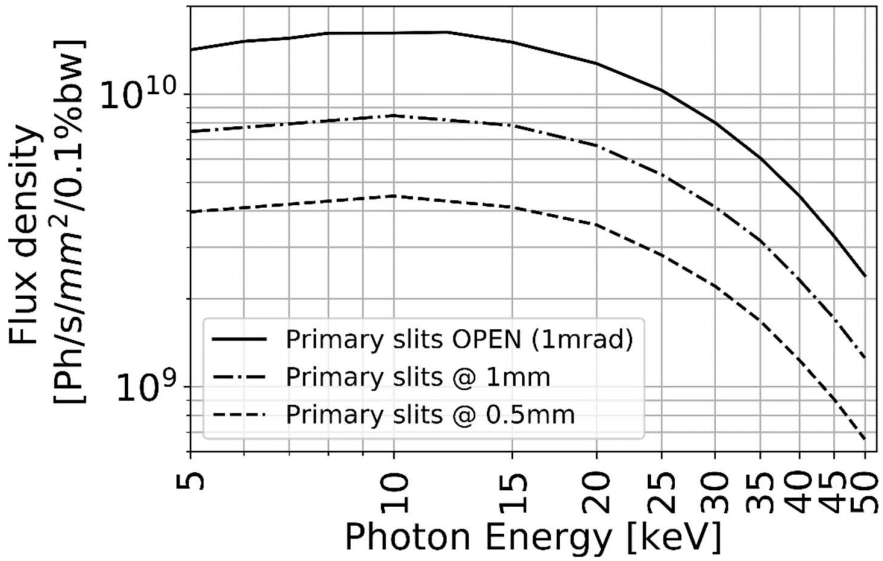

Figure 63: White beam spectral flux density through 1x1mm2 pinhole @ sample position (43m from source) for three different settings of the primary slits. XOP and ShadowOui data.

9.3.4.2 Pink beam flux density @ sample with different attenuating elements

Foils of different attenuating materials and with different thicknesses will be installed in the attenuator tower in the front end to condition the x-ray spectrum and particularly reduce the total heat load and radiation dose by filtering low energies. Plots of the expected pink beam spectrum at the sample are shown in Figure 64. For each plot, two CVD diamond windows with a total thickness of 0.7 mm were considered. The plots are grouped for different examples of attenuating material: Al (A), Cu (B) and graphite (C). The effect of 1 m propagation distance in air is also shown (Figure 64C).

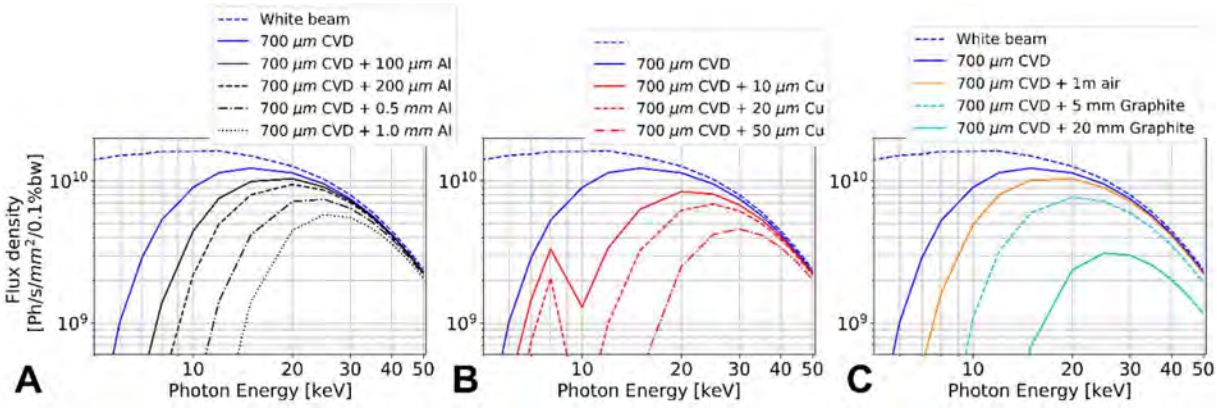

Figure 64: Pink beam spectral flux density through 1x1mm² pinhole at the sample position (43m from source); effect of different attenuating elements for the treatment of the polychromatic spectrum. XOP and ShadowOui data.

9.3.5 Flux density @ sample after DMM:

The flux through a pinhole at the sample position is obtained from ShadowOui and XOP simulations. The OASYS ShadowOui tree is shown in Figure 65.

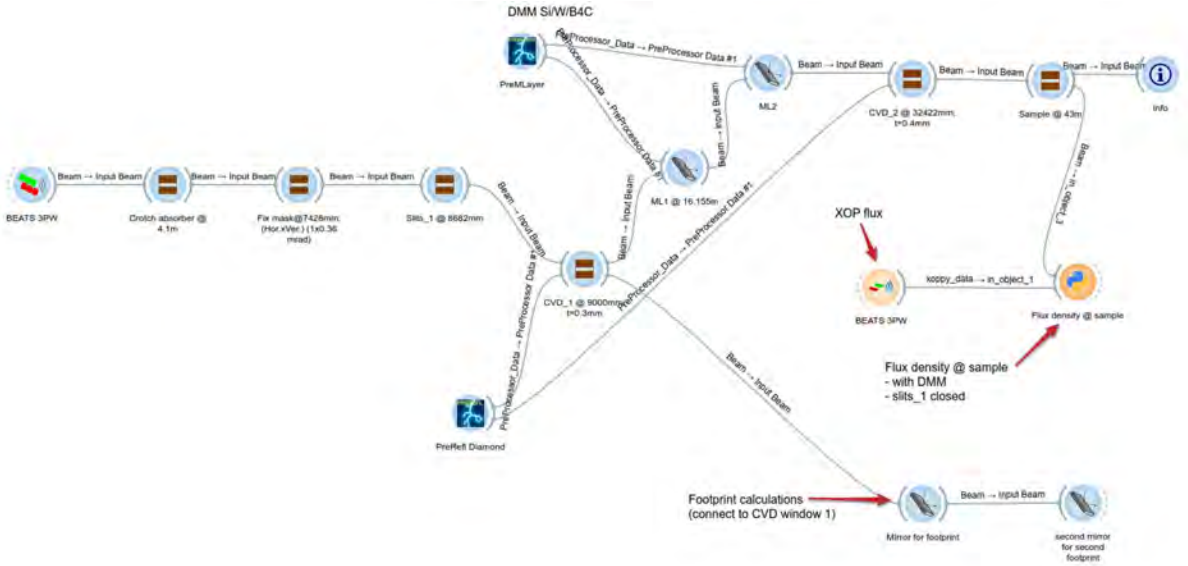

Figure 65: Oasys tree for the calculation of the BEATS spectral flux density after the DMM and through a pinhole at the sample position (43m from source).

The photon flux at the sample position is calculated based on Equation 6 as in (Abdellatief et al. 2017):

$$F_{sample} = F_{XOPsource} \frac{\Delta E_{source}}{0.001E} \frac{I_{sample}}{n.rays} \quad (6)$$

Equation 6: Monochromatic flux at sample position

Where $F_{XOPsource}$ is the flux from the XOP source at a given energy, ΔE_{source} is always set large enough to include the whole DMM bandwidth (4% for STRIPE_1 and 6% for STRIPE_2), E is the photon energy, I_{sample} is the intensity from ShadowOui through an aperture at the sample position and *n. rays* was 2E+6 for all simulations.

Figure 66 shows the spectral flux density (0.1% BW) at the sample position obtained with the two different DMM stripes. The flux density reduction due to DMM reflectivity at a certain energy is

between 30% and 70% compared with the flux density available from the white beam at the same energy. It should be noted that the two stripes have different resolution and therefore different integrated reflectivity. The effective flux density (considering the different resolution and reflectivity of the two stripes) is shown in Figure 67.

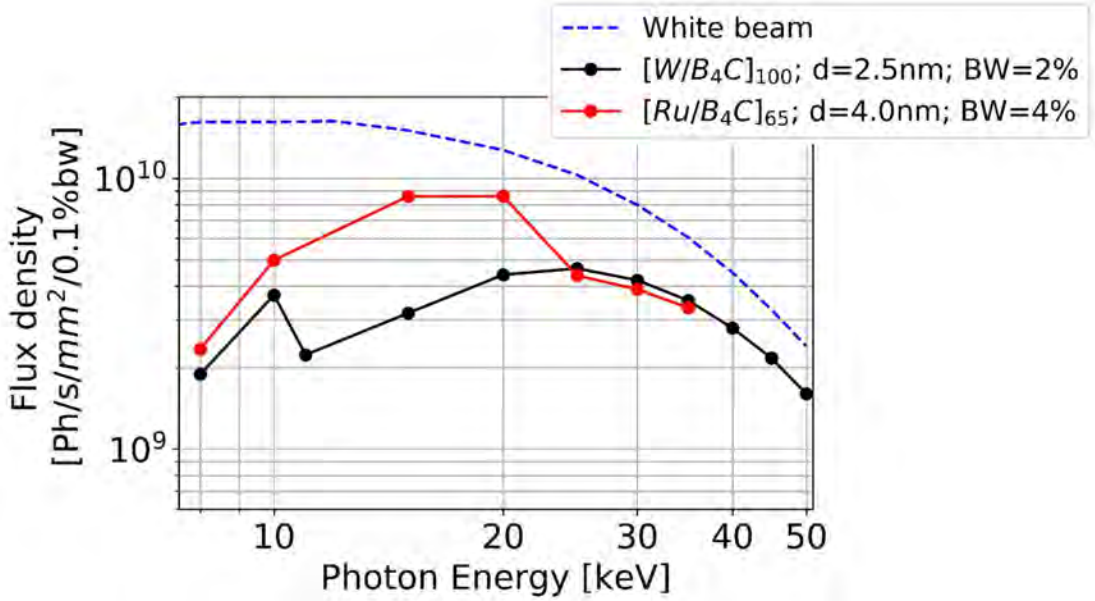

Figure 66: Spectral flux density after the DMM through 1x1mm^2 pinhole at the sample position (43m from source) and for 1% of the DMM bandwidth. XOP and ShadowOui data.

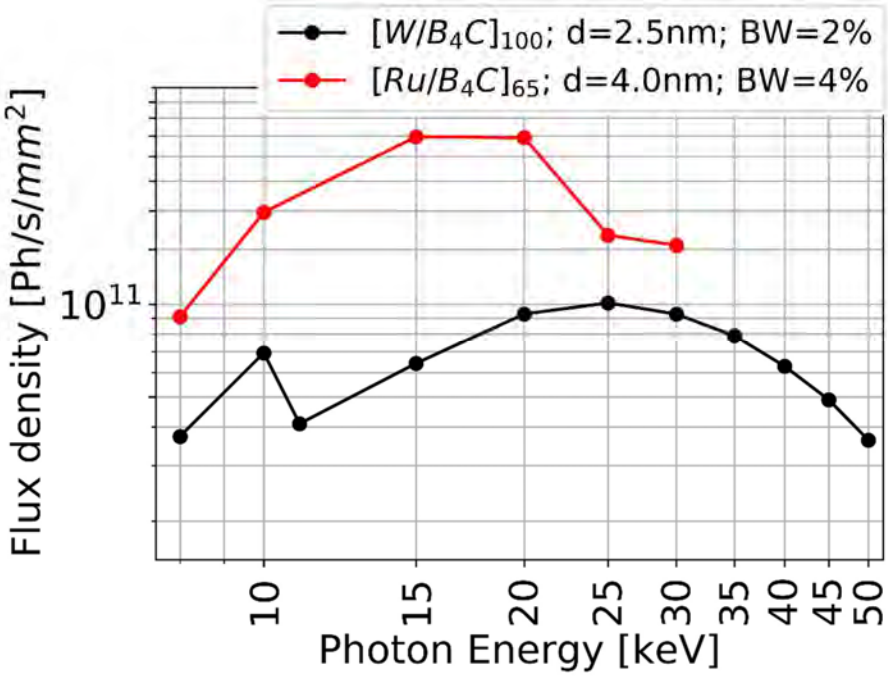

Figure 67: Spectral flux density after the DMM through 1x1mm^2 pinhole at the sample position (43m from source) considering the effective DMM bandwidth. XOP and ShadowOui data.

9.4 Design and motorization in the Optics hutch

Table 10 presents the number of motorized axes required in the Optics hutch.

Equipment	N. of axes	Along axis	Encoder	Comment
Trigger unit	1	Y	Yes	Wire monitor
DMM	7(+1)		Yes	Controllers for eventual piezo motors must integrate with EPICS and be provided by DMM supplier.
Mirror 1	3	X	Yes	Stripe select
		Y	Yes	Retract crystal for pink beam
		Pitch	Yes	Bragg
Mirror 2	4	X	Yes	Stripe select
		Y	Yes	Offset
		Z	Yes	Stroke
		Pitch (coarse)	Yes	Bragg
		Pitch (fine)	Yes	Bragg
		Roll		Can be manual
Beam Viewer	1 or 2	Y/Y	Yes	Might require two axes if separate screens are used for pink and monochromatic beam
Combined Stopper	1	Y	No	Pneumatic

Table 10: Optics hutch equipment with information on motorized components.

10 Experimental Station

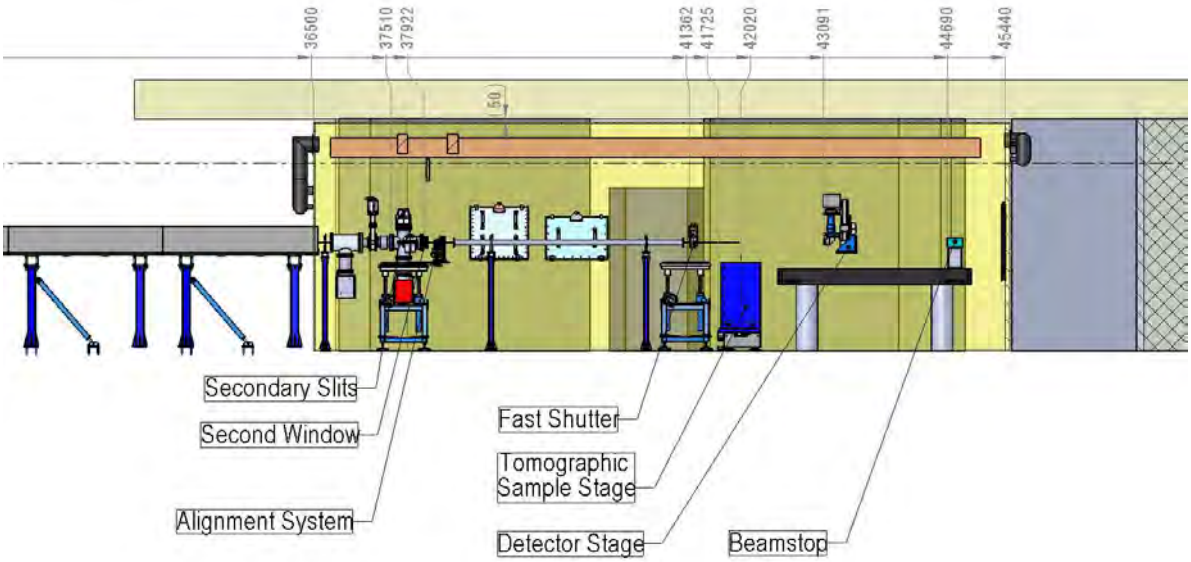

Figure 68: Experimental hutch, side view

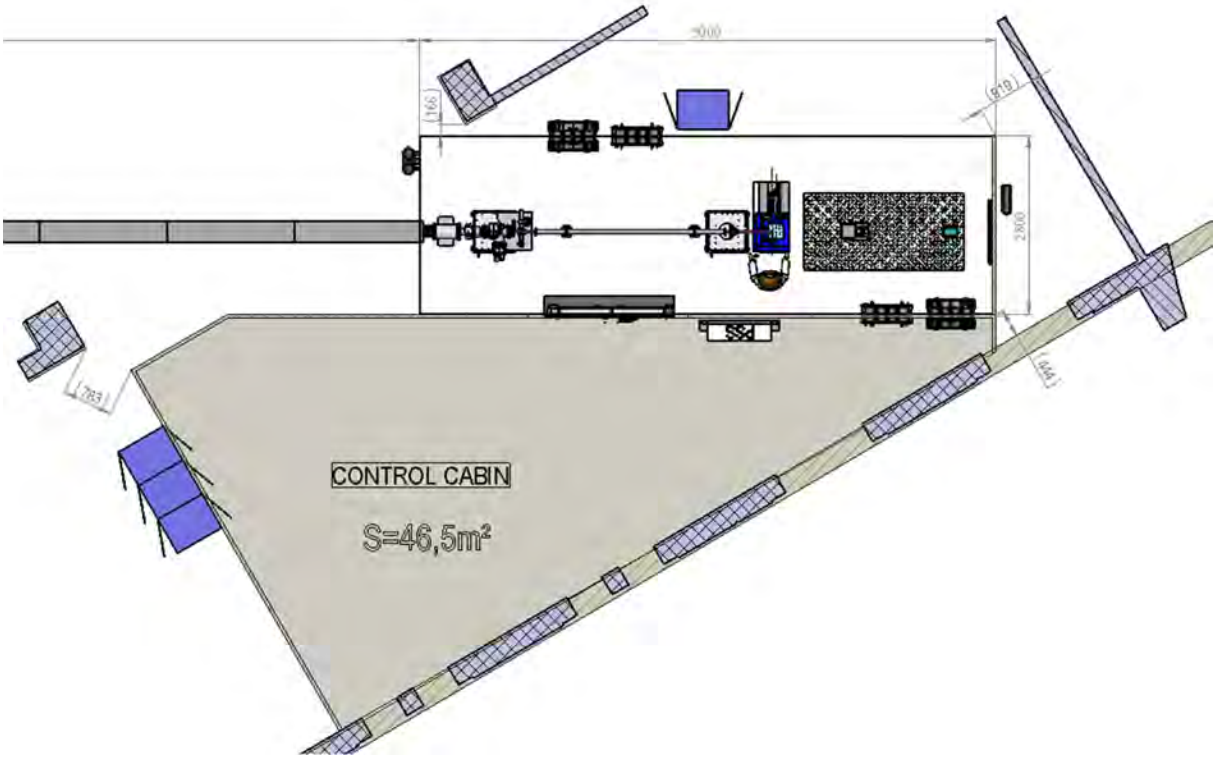

Figure 69: Experimental hutch, top view

The experimental hutch is located under the mezzanine of SESAME's main office building adjacent to the experimental hall and fits between two concrete pillars. The hutch will cover a length of 9 m allowing, if one includes space for optical components and the beam stop, the positioning of the sample at a distance between 38 m and 43 m from the primary photon source.

A space of 50 mm has been left between the roof top of the hutch and the slab of the mezzanine. A precise measurement campaign of the ground and ceiling will be done prior to hutch installation.

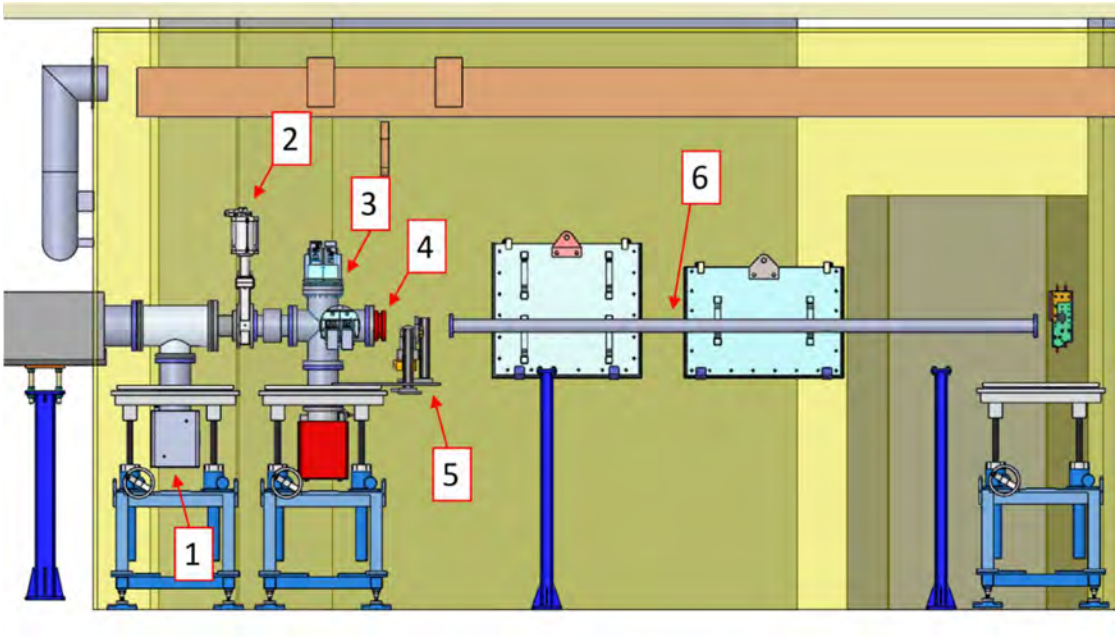

Figure 70: Side view of the BEATS experimental hutch showing the beamline exit. (1) pumping station. (2) gate valve. (3) secondary in-vacuum slits. (4) second beamline CVD window. (5) laser alignment system. (6) flight pipe.

10.1.1 Pumping unit and Gate Valve

At the entrance of the experimental hutch, a standard gate valve preceded by a pumping unit of 300l/s capacity will be installed (Figure 70). A bellow is located right downstream of the valve. With a 300l/s ion pump, the maximum pressure inside the 15.5-m-long transfer line will remain below 5 x 10^{-6} mbar when the gate valve is closed (i.e. during service or shutdown) (Figure 71).

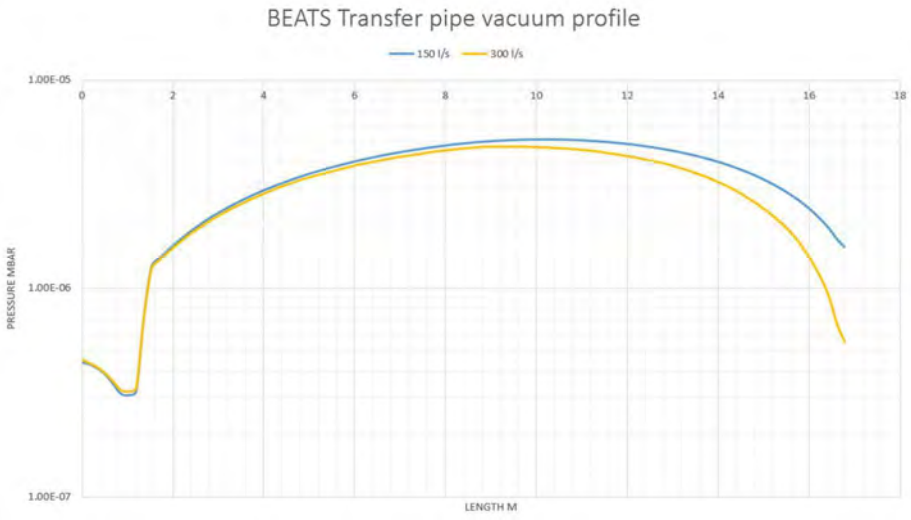

Figure 71: Vacuum level inside the transfer line with 150l/s (light blue), 300l/s (yellow) ion pumps before the gate valve in the experimental hutch. Simulations performed when the gate valve is closed (service or shutdown mode).

10.1.2 Secondary Slits

A set of 4 water cooled blades will be put in a UHV cross chamber inside the experimental hutch and at approximately 37.6m from source (Figure 70). At this location, the pink beam will have a dimension of 43.8 × 13.8 (H × V, top-hat) mm^2. The blades of the slits should sustain white beam heat load. Therefore, a calculation to determine if the blades require cooling will be performed. A pre-pumping system will be connected to the cross as well as gauges.

This slits assembly together with the second CVD window downstream will be located on a vertical translation stage (presented in Figure 70 as a 4-feet table) which will be motorized.

10.1.3 Second Window

The second window (#3 in Figure 70) will be the last component of the beamline connected to the beamline vacuum system. It will be positioned at ~37.9 m from the source and will be the last component of the secondary slits system. At this location and for a divergence of 1.0 × 0.36 (H × V) mrad, the window must be as large as 50 × 14 (H × V) mm^2 (Figure 72).

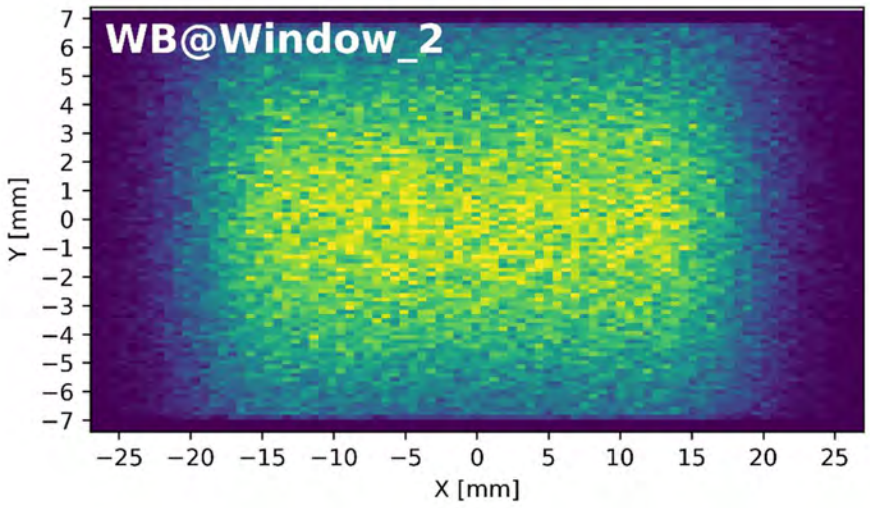

Figure 72: White beam snapshot at 37.9 m from the source.

A rectangular CVD diamond window with thickness between 0.3 and 0.4 mm will be used. This large CVD diamond window will be brazed to a copper disk and flange.

We have calculated the maximum absorbed power by the second CVD window for a thickness of 0.4 mm for the worst-case scenario (i.e. when the beamline is operated in pink beam mode). In this case the second window will absorb 6.5 W with maximum power density of 0.022 W/mm^2.

The vertical motorization system described above will allow to translate vertically the aperture of the second window and thus to adapt to the switch (up to 16 mm offset) between operation in monochromatic and pink beam.

10.1.4 Alignment System

A laser beam is required to align samples on the X-ray beam path. The alignment system (#5 in Figure 70) will be composed of a mirror installed on a standard translation stage. The mirror will be retracted automatically prior to letting the beam enter the hutch.

10.1.5 Flight pipes

Propagating the X-ray beam in air for several metres before the sample and detector has detrimental effects on the final image quality, since scattering in air reduces the effective dose of photons reaching the detector and increases image blur. A custom system of flight pipes (#6 in Figure 70) will bring the beam under vacuum from the second CVD window to the proximity of the sample. The system foreseen includes a set of aluminium pipes of different length with Kapton windows on both ends pumped to mild vacuum and positioned in the beam path after the CVD window. Alternatively, PVC pipes flushed with helium can be used. The pipe length will be customized based on the propagation distance required by the experiment. Furthermore, the position of this pipe might require vertical adjustment when switching between monochromatic and pink beam modalities.

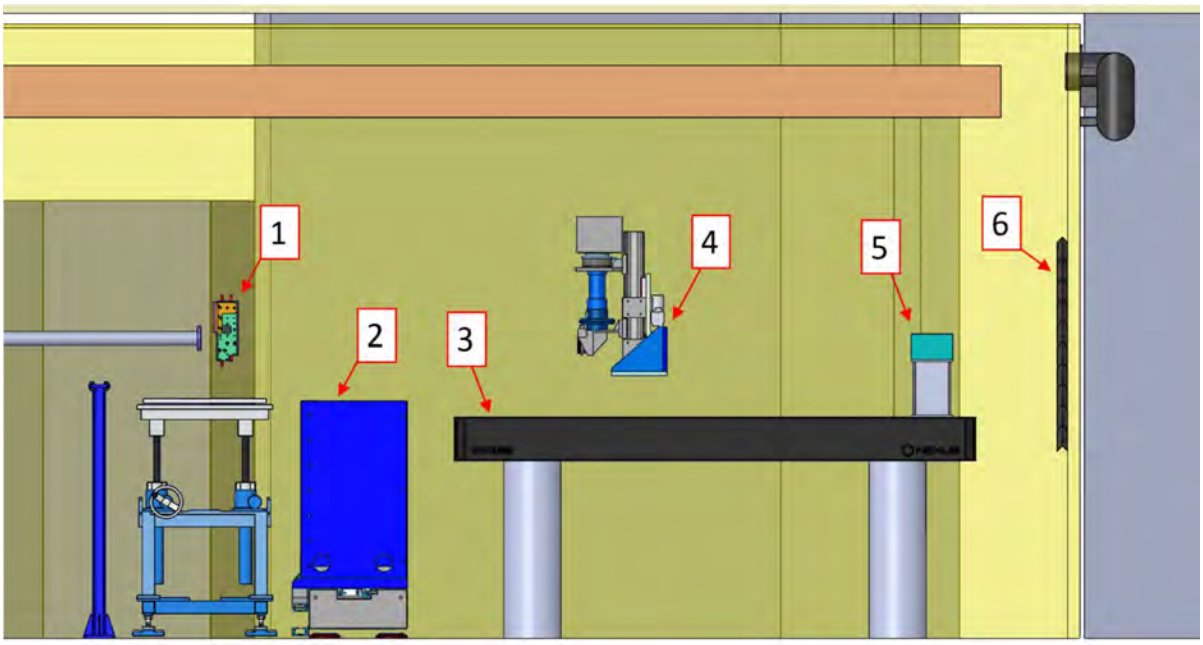

Figure 73: Side view of the BEATS experimental hutch showing the tomographic experimental station. (1) fast shutter installed on a motorized table with vertical stroke. (2) tomographic sample stage. (3) optical breadboard table. (4) detector stage with motorized translations. (5) beamstop. (6) local shielding.

10.1.6 Fast Shutter

The fast shutter (#1 in Figure 73) will be fixed rigidly to a standard optical bread board (or a granite slab) and installed on an independent motorized vertical translation stage. When switching from pink beam to monochromatic (or vice versa) or varying the DMM offset, the fast shutter can follow the vertical movement of the beam. The system could be further modified to allow the vertical translation of the flight pipe jointly with the fast shutter.

An in-air fast shutter system will be used to reduce the dose of radiation absorbed by the sample and to precisely control the exposure time. Table 11 presents the main features of this equipment. The device will be based on brushless linear motor technology. 4-mm-thick blades will be manufactured from tungsten alloy or titanium.

Exposure time (Min.)	~50 ms
Repetition rate	1 Hz
Blades speed (Max.)	200 mm/s
Hor. Aperture (Max.)	80 mm
Ver. Aperture Max.)	20 mm
Blades material	Tungsten alloy
Blades thickness	4 mm

Table 11: Technical specifications for the Fast Shutter.

Figure 74 presents the design principle of the fast shutter that will be installed at the ESRF (BM05 and ID19) and which is under development. The installation of this system is also foreseen for BEATS. Due to its weight, each blade will be actuated by 2 synchronized motors.

In order to quickly open and close the blades, the following sequence has been chosen to benefit from gravity: i) quick descent of lower blade (opening). ii) Exposure. iii) Quick descent of upper blade (closing). iv) Rise of lower blade. v) Rise of upper blade.

Fast control and synchronization are the key points of this equipment. For the development, a test bench is under construction at the ESRF (Figure 74C) onto which a laser diode and a photodiode will be fitted.

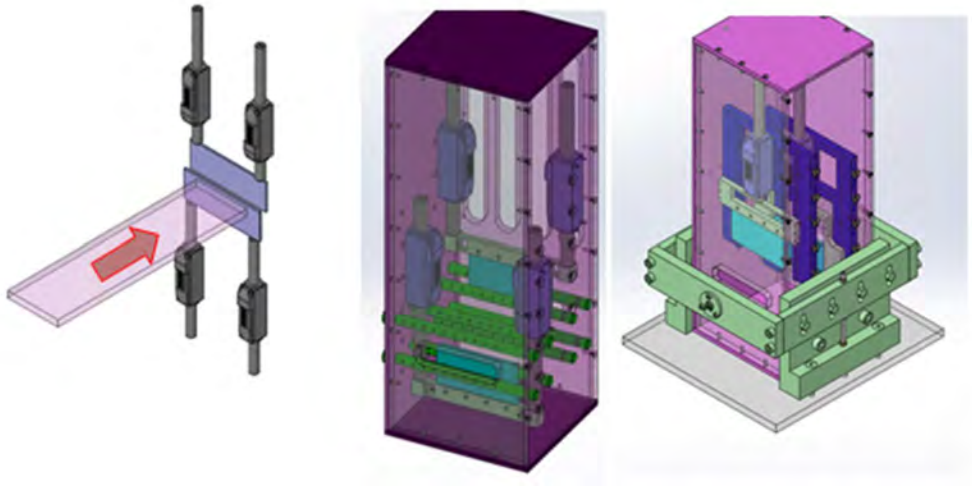

Figure 74: Principle and 3d view of the Fast Shutter, b) View of the pre-study (in green are the cooling elements to blow compressed air to the blades), c) Test bench. Courtesy: C. Muñoz Pequeño and P. Theveneau.

10.1.7 Beam stop

A cooled Cu block of 120 × 120 × 200 (Width × Height × Thickness) mm^3 is fixed in front of the lead back wall of the experimental hutch as illustrated in Figure 73 (element #5). The beam stop can be mounted directly on the optical table hosting the detector stage as shown in Figure 73, on an independent support, or fixed to the back wall of the hutch. 500 mm of extra space are foreseen between the beam stop and the back wall of the experimental hutch. At this location (45.3 m from the source), the pink beam has a dimension of 60 × 17 (H × V) mm^2 (Figure 75). After the beam stop, a further local lead shielding of 1500 × 1500 × 7 (Width × Height × Thickness) mm^3 will be installed before the back wall of the experimental hutch (#6 in Figure 73).

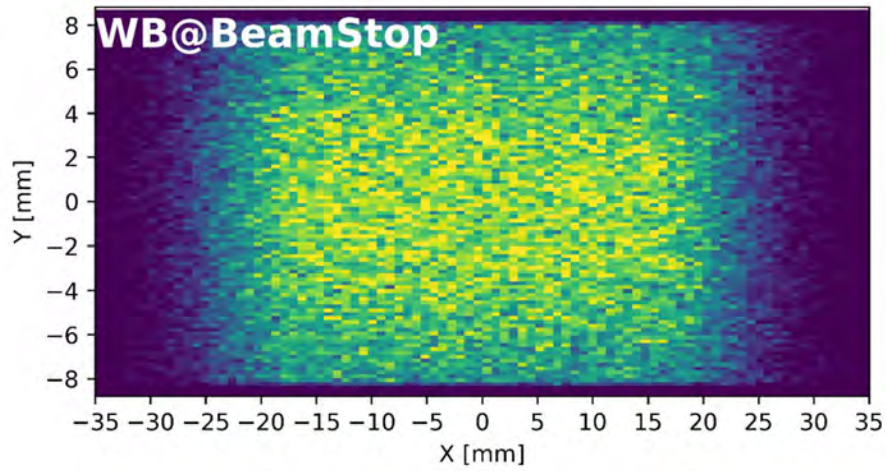

Figure 75: White beam snapshot at 45.3 m from the source.

The beam stop will intercept and attenuate the pink beam, absorbing the remaining thermal power transmitted by the 1st and 2nd CVD windows. The total power absorbed by the beam stop will be 39 W, with maximum power density of 0.084 W/mm^2. Figure 76 shows the power density of the absorbed power.

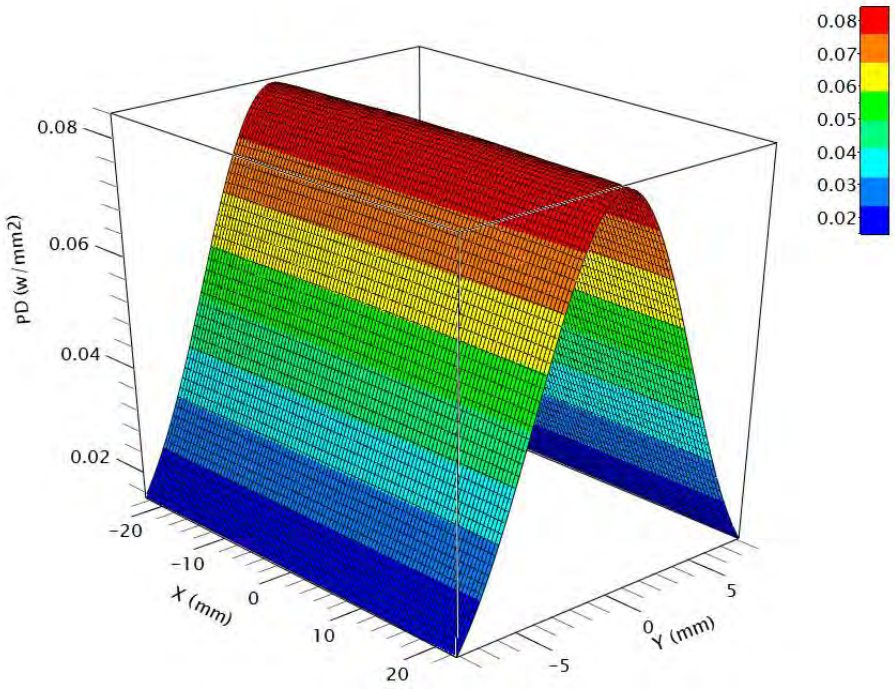

Figure 76: power distribution absorbed by the beamstop.

10.2 Sample stage

BEATS will require a robust turnkey sample stage, allowing to reduce as much as possible curative actions, if any, and downtime. The tomographic sample stage should be based, if possible, on proven solutions, keeping a good level of performance and flexibility at the same time. In this paragraph we present a sample stage for computed tomography which is currently in use at the ESRF on the ID19 and BM05 beamlines. The device shown in Figure 77, which was jointly developed by the ESRF and the

company *LAB Motion* in 2013, is a reliable solution which is versatile for multiple applications (Renier et al. 2013).

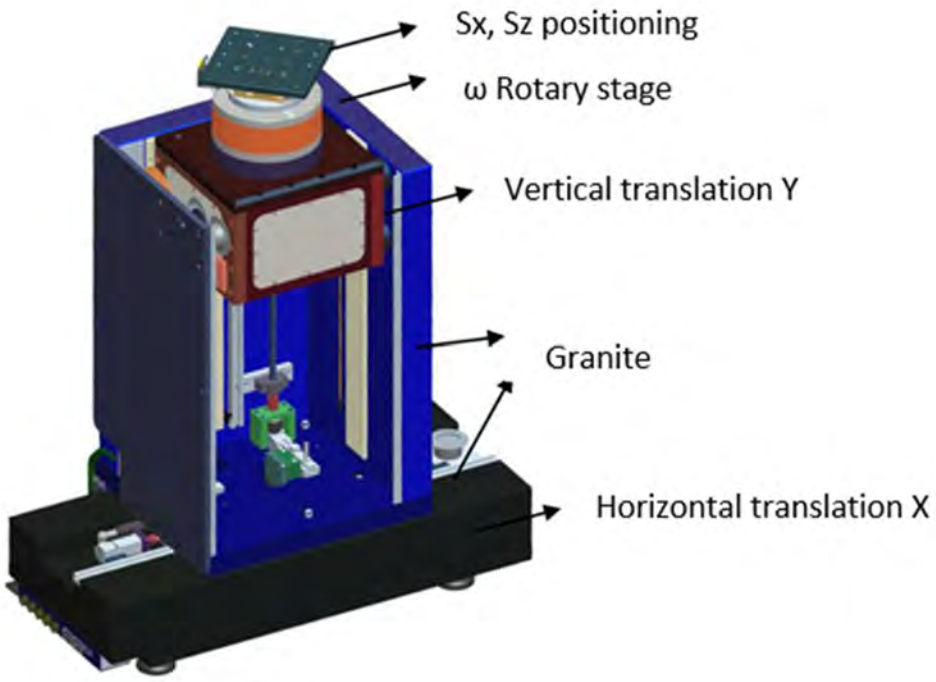

Figure 77: 3D model of the tomographic sample stage for BEATS.

The tomographic sample stage shown in Figure 77 is composed of different motorized stages mounted over a large solid stand. At the ESRF, the stage is mounted on air pads that allow the system to travel along the beam direction over a long stroke, tuning in this way the sample-to-detector propagation distance. For the experiment, the stage is locked to the selected location by releasing the pressure of the air pads. In this configuration, the path along the stroke in the experimental hutch must be paved with granite tiles with a demanding degree of planarity. When air pads are active, the stage can be displaced manually along the beam by pushing the equipment. Alternatively, the displacement of the sample stage can be automated using a friction wheel and a system of rails for linear translation. In the case of BEATS, the maximum foreseen sample-to-detector propagation distance will be 3 m (see paragraph Propagation-based phase contrast imaging at BEATS), the required flexibility can be achieved by automating the displacement of the detectors over 3 m stroke and keeping the position of the sample stage fixed. The position of the tomographic sample stage will be predisposed at the farthest point from the photon source (approximately 42m from the x-ray source). This setup remains flexible towards modifications and future upgrades, since the sample stage can be easily repositioned using the crane in the experimental hutch or a system of wheels.

The proposed sample stage is composed of high-precision, wide-range linear stages and of a high-precision rotary stage based on air-bearing technology. The linear stages can be based on ball bearing with stepper motors, linear brushless motors (BLDC) with air bearings, or a combination of the two technologies. The advantages of using air bearings and BLDC are lower parasitic error motion, better repeatability and higher speed with less vibrations. The downside is a higher cost and the need for an oil-free compressor unit. Stepper motors are cheaper and have better position stability. All motorized axes of the stage are equipped with encoders. Technical specifications of the device are reported in

Table 12: the accuracy in sample positioning (Minimum Incremental Motion or MIM, third column in Table 12) must be better than 1 µm along all the directions. When the desired sample position is reached, the translation of the linear stages is locked, and the scan is performed activating the rotary stage. Thanks to the high axial and tilt stiffness of the rotary stage, motion errors remain below 100 nm during sample rotation.

The proposed tomographic sample stage was developed specifically for samples with maximum dimensions of 400 mm in diameter and 550 mm in height, for a maximum weight of 300 N. Thanks to its large horizontal translation perpendicular to the beam, the sample stage also allows the 2D scanning of large samples over a 500 x 550 mm^2 area. The large vertical stroke allows for the automated scanning of a vertical stack of samples mounted on a common holder (Figure 78). The maximum speed of the rotary stage is 60 rpm, while the plate for sample mount is a breadboard allowing customization with different sample holders depending on the application.

	Stroke	MIM	Resolution	Accuracy	Repeatability	Straightness / flatness	Radial / axial motion error	Angular errors	Speed
X-stage (horizontal)	500 mm	0.5 µm	0.1 – 0.5 µm	± 15 µm/m	1 µm	5 µm		50 µrad	25 mm/s
Y-stage (vertical)	550 mm	0.5 µm	0.1 – 0.5 µm	± 15 µm/m	1 µm	10 µm		50 µrad	25 mm/s
Rotary stage	continuous multi turn	0.1 arcsec	< 0.1 arcsec	± 10 arcsec	0.1 arcsec		< 100 nm	1 µrad	60 rpm
S_x stage	± 20 mm	5 µm	-	50 µm	5 – 8 µm				5 mm/s
S_z stage	± 20 mm	5 µm	-	50 µm	5 – 8 µm				5 mm/s

Table 12: Main characteristics of the tomographic sample stage proposed for BEATS.

The embodiment of Figure 77 does not include motorized goniometers or a tripod for the alignment (particularly the pitch) of the tomographic rotation axis. The stage must be aligned after installation to ensure that the rotation axis remains vertical, and high repeatability can be expected afterwards thanks to the stiffness of the system. The total mass of the assembly is around 800 kg.

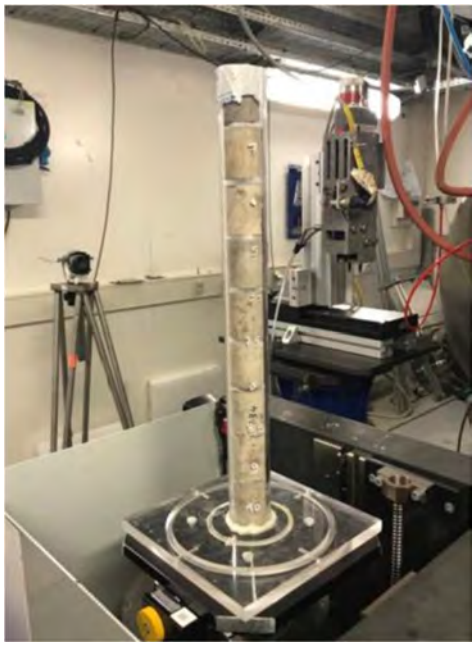

Figure 78: Sample holder for scan automation over a vertical stack of samples. Photo of ID19 of the ESRF courtesy Shiva Shirani.

10.3 Sample environment

10.3.1 Mechanical testing device

The experimental station of BEATS will be equipped with a device for in situ mechanical conditioning of samples during tomography experiments. The possibility to control the mechanical load applied on a sample while imaging its interior in 3D has wide potential for application in the fields of materials science and engineering, significantly expanding the impact of the beamline. Research on the fracture and mechanical behaviour of both artificial and biological materials will greatly benefit from this sample environment. Furthermore, the high brilliance of synchrotron X-ray sources allows to reduce scan duration and perform time resolved analysis in combination with mechanical testing (Le Cann et al. 2019; Martelli and Perilli 2018; Madi et al. 2020; Alexander Rack et al. 2020; Chen et al. 2020).

Figure 79 shows different implementations of mechanical testing rigs for application with computed tomography. Images were taken at other synchrotron or laboratory tomography stations.

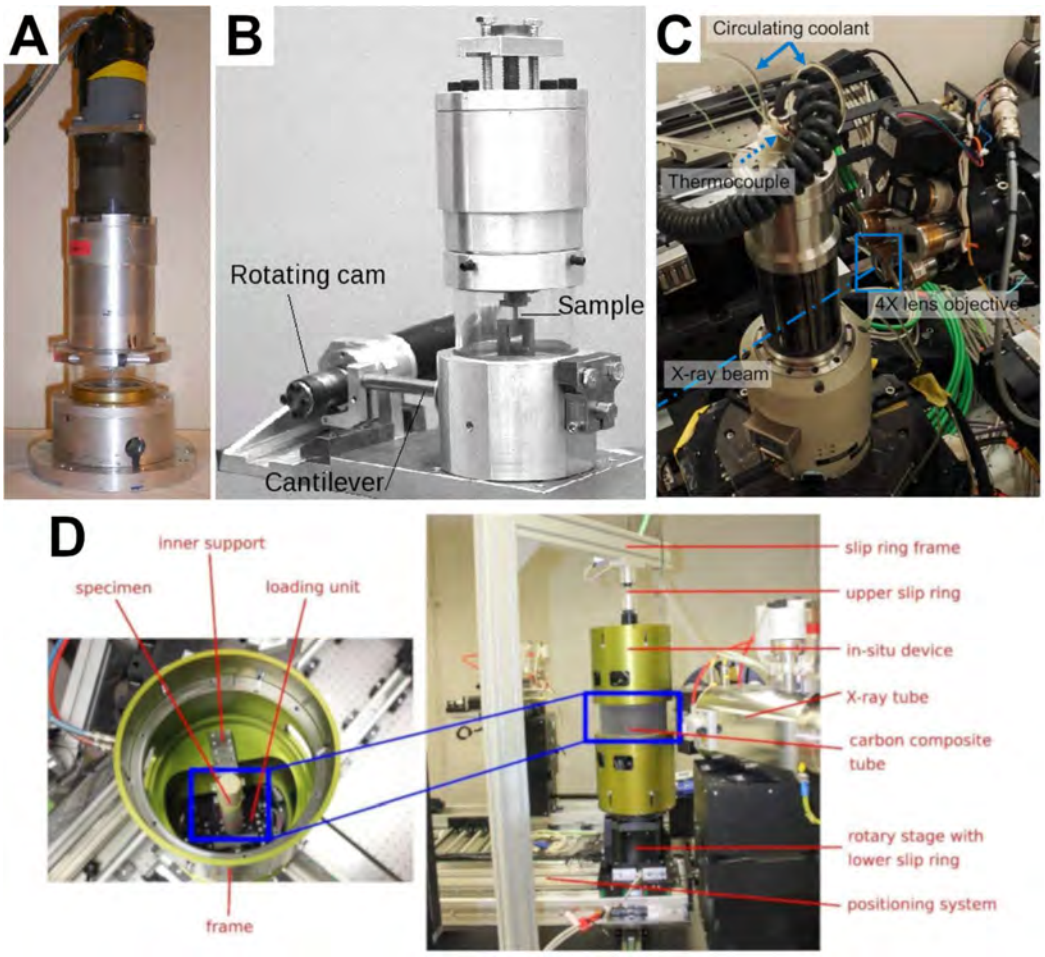

Figure 79: Testing devices for in situ synchrotron tomographic imaging of samples under mechanical load. (A) Monotonic tension/compression device installed in ID19 at the ESRF from (Buffiere et al. 2010). The load cell is at the bottom of the rig attached to the lower grip which is fixed. The displacement of the upper grip is driven by a stepper motor with appropriate reductor. The machine weights 6 kg and can apply up to 5000 N. (B) Cyclic tension/tension device. The load is applied via a cantilever and an elliptical rotating cam. In both A and B, a transparent PMMA tube transmits the load. (C) CT5000-TEC device from Deben, Bury Saint Edmunds, UK. This device is equipped with a 5000 N load cell as well as a Peltier heating system and cooling of the jaws. Picture from (Peña Fernández et al. 2018). (D) Modular device for bending testing by (Kumpova et al. 2020). In both C and D the frame of the loading chamber accommodating the specimen is built in carbon-fiber ensuring sufficient stiffness and low X-ray attenuation

The mechanical testing device of BEATS will be installed directly on the tomographic rotation sample stage and should therefore have limited weight. The system should be modular, allowing easy sample exchange and testing in tension and compression with loads up to 5000 N. The design of the device should envision the possibility to adapt the system to other loading cases (e.g. three- and four-point bending) as well as to temperature control. Since the assembly rotates jointly with the sample during the experiment, its frame must be free of elements interfering with the camera field of view during the full 180° tomographic rotation. In addition, all cabling must be installed on a slip ring. Support and load transfer can be accomplished with x-rray transparent materials such as glassy carbon or PMMA. Different grips and jaws (tension and compression) and compression plates will be provided for holding samples with different shapes and sizes. The actuator or motor driving the displacement of the jaws or plates should be equipped with encoders. The device must allow testing of samples of up to 20 mm width and must be equipped with load and displacement sensors. The load cell must respond linearly over the full-scale range with a minimum resolution of 1000:1. Displacements can be measured with a linear extensometer, allowing to perform load- as well as displacement-controlled experiments. The lower part of the equipment must be sealed allowing the testing of wet samples.

10.4 Detectors

10.4.1 Detector Stage

Downstream of the tomographic sample stage (#1 in Figure 73), a 2.5-m-long optical breadboard (or granite) table will be installed (#2 in Figure 73), hosting a motorized stage for the positioning of the detector (#3 in Figure 73). In case of a granite table, the considerable weight can increase the stiffness of the assembly. In the case of an optical breadboard table, this should be installed on a solid steel frame or on a base in reinforced concrete or granite.

Detector stages from the SYRMEP, TOMCAT and ID19 synchrotron tomography beamlines (Elettra, SLS and ESRF, respectively) are shown in Figure 80 and taken as examples for the BEATS detector stage. The design of the detector stage will allow the positioning of the detector's scintillator near the sample and without interfering with rotating parts for experiments requiring short propagation distances. Different detectors can be installed on the same support. Detector optics will be protected from scattered radiation with lead or tungsten shielding as much as possible.

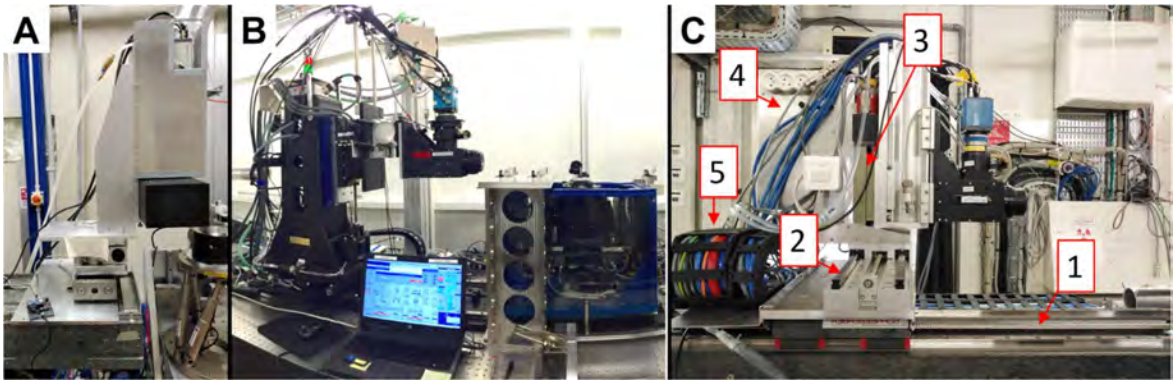

Figure 80: Detector stages for tomographic microscopy at the SYRMEP beamline of Elettra (A), TOMCAT beamline of the SLS (B) and ID19 beamline of the ESRF (C). Direction of beam propagation: right to left. In A and B the sample manipulator is visible on the right. Image in A courtesy of Dr. Diego Dreossi. B from the TOMCAT beamline webpage. C is courtesy of Dr. Alexander Rack.

The BEATS detector stage will include:

- A system of rails (#1 in Figure 80C) for the translation (Z) of the detector assembly along the beam propagation path over a stroke up to 2.5 m. The system should be motorized, allowing the remote control of the sample-to-detector propagation distance with an accuracy of few millimetres. The Z-stage can be further split into two stages acting in series as follows:
    - Belt-driven stage/slide for long travel range and coarse positioning. This removes the requirement of a 2.5-m-long spindle.
    - Precision linear stage with spindle for high precision Z positioning over a limited stroke. The high precision stage is installed on top of the coarse stage.
- A motorized stage on rails for lateral translation (X), allowing the selection and alignment of the detector (#2 in Figure 80C).
- Motorized vertical elevators (Y) for alignment and centring the beam on the scintillator screen (#3 in Figure 80C). An independent Y-stage will be installed for each detector.
- Support for controllers and utilities (e.g. flowmeters for camera cooling water) can be also included on the back of the detector stage (#4 in Figure 80C).
- Cable handling will be managed by means of one or two cable chains (#5 in Figure 80C).
- All stages will be equipped with encoders allowing to record motors positions after detector alignment and therefore to automate the detector switch.
- The detector stage will be equipped with limit switches preventing the collision of the detectors with sample and sample stage.

10.4.2 Detectors rationale

BEATS should be equipped with a portfolio of detectors offering the possibility to operate the beamline and acquire full-field tomographic images using monochromatic as well as (filtered) white X-ray beam. To cover a broad range of applications with maximum versatility, we will install a white beam microscope equipped with different lead shielded objective lenses and providing a range of image magnifications. Two magnifications at least should be available and interchangeable on a single setup. To further exploit the beam size (up to 40 mm horizontally) attainable at the sample position, a detector with lower resolution and larger field-of-view (FOV) is also proposed. Finally, a high-resolution microscope with high numerical aperture lenses for use with monochromatic beam is considered.

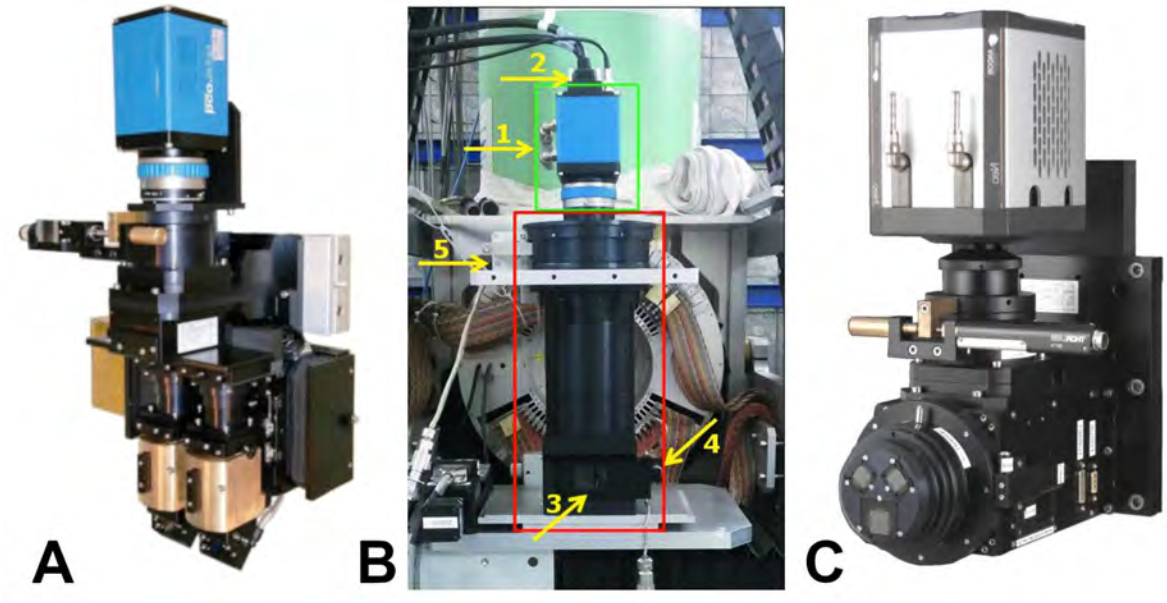

Figure 81: A) Monochromatic high-resolution revolver microscope from Optique Peter mounting Andor Neo camera. B) Optique Peter double objective white beam microscope with pco.edge camera. C) Large field of view detector with pco.edge5.5 camera installed at the biomedical beamline (ID17) of the ESRF (Mittone et al. 2017).

10.4.3 White-beam microscope

For operation with pink beam the objective lenses must remain outside of the beam propagation path. A mirror between objective and scintillator is utilized to reflect vertically the luminescent image by the scintillator out of the x-ray beam path. Figure 81A shows a double-objective white beam microscope from Optique Peter. A lead casing hosts and protects from scattered X-ray radiation two interchangeable long-working-distance objective lenses. A small format sCMOS sensor camera is directly mounted on top of the objective lenses by a movable coupling, allowing the selection of the desired optics. A single scintillator support is installed for each objective. The support allows manual regulation of the tilt and flushing of the scintillator with an inert gas. A case hosting optical filters before the camera sensor is present. In addition, each objective interface can host an individual filter between objective and camera sensor. Different lenses with radiation hardened front lens will be available, covering magnifications from 2× to 10×. Theoretical object pixel sizes for 2× and 10× objectives are 3.5 µm and 0.7 µm, respectively, with horizontal FOV of 8.32 mm and 1.66 mm, respectively (Table 13). The focus of this system is motorized and controlled by SESAME's motion control interface.

objective magnification	N.A.	object pixel size [um]	FOV	
			Hor [mm]	Ver [mm]
1x	/	6.50	16.64	14.04
2x	0.055	3.25	8.32	7.02
4x (mono)	0.16	1.63	4.16	3.51
5x (WB)	0.14	1.30	3.33	2.81
7.5x (WB)	0.21	0.87	2.22	1.87
10x (mono)	0.30	0.65	1.66	1.40
10x (WB)	0.28	0.65	1.66	1.40

Table 13: Numerical aperture (N.A.), object pixel size and field-of-view (FOV) with different objective magnifications and a 2560×2160 pixels sCMOS sensor with 6.5 µm pixel size. WB: white-beam (radiation hardened) lens. Mono: monochromatic microscope lens.

10.4.4 Low magnification detector

An indirect conversion optics with large FOV will complement the x-ray detectors of BEATS. This will allow the exploitation of the wide fan of radiation available at the sample position. We will use a system developed in-house at the ESRF (Figure 81B) and already in use for tomographic applications at ID17 and ID19. This device uses a scintillating screen, a mirror and macro lenses arranged outside of the primary beam propagation path. Two macro lenses will be available for 1× and 2× optical magnifications. Focus and detector matrix alignment can be motorized. The performance of a sCMOS pco.edge 5.5 camera when used in combination with this detector was characterized already (Mittone et al. 2017). Object pixel sizes of 6.2 µm and 3.1 µm were obtained, respectively, with the 1× and 2× lenses, for a FOV of 14.08 mm × 11.65 mm and 7.04 mm × 5.94 mm, respectively (Table 13). The study by Mittone et al. also demonstrated excellent linearity in the detector's photo-response as well as low noise levels of the system.

The combination of low magnification and microscope white beam optics can be exploited for simultaneous image acquisition on both systems, when the detectors are installed in series with the white beam microscope on the front. In this case, the bending mirror of the white beam microscope is of glassy carbon and allows part of the incident X-rays to pass through the first system for detection with the low magnification device which is positioned behind. The combination of these two detectors for simultaneous acquisition of images of the same samples at different resolutions was recently described by (Mittone et al. 2020).

10.4.5 Monochromatic, high-resolution microscope

A high-resolution microscope with interchangeable high numerical aperture objectives is considered for high sensitivity applications requiring monochromatic beam from the DMM. A monochromatic microscope of this kind is shown in

C. In this system, the objective lenses remain within the X-ray beam path and the device cannot be operated with pink beam. The microscope can mount a revolver hosting three objectives for automatic magnification selection (as in Figure 81C), or a single objective lens. In the latter case, the desired magnification must be selected and installed manually before the beamtime. In both cases, focus control is automatic. The system can host a multiple or single lightproof scintillator support allowing regulation of the scintillator's orientation. A motorized support controls the alignment of a small-format, sCMOS camera connected through F-mount and brackets. The optical configuration with higher magnification considered for BEATS is 10×, providing a theoretical object pixel sizes of 0.7 µm and a resolution limit of approximately 1 µm. Pixel sizes and fields of view of different optics are collected in Table 13. Spare objective lenses for the monochromatic microscope can be included in the initial procurement for replacement after darkening due to direct exposure to the X-ray beam.

10.4.6 Cameras

We will procure two identical cameras based on cooled, high-resolution, monochrome scientific CMOS (sCMOS) sensors providing frame rates up to 100 fps in full-area mode, low readout noise and 16-bit dynamic range at best. The ideal candidate is the pco.edge 5.5, since this camera is already in use at the TOMCAT beamline of the SLS and at the ID17 and ID19 beamlines of the ESRF, and we can rely on the know-how of these groups as well as on a data acquisition system provided by TOMCAT. A pco.edge 5.5 is equipped with a 2560×2160 pixels sCMOS sensor with a physical pixel size of 6.5×6.5 μm^2. It provides low readout noise (1.0 e- med), peak quantum efficiency > 60% and a dynamic range of 30'000:1 ("Pco.Edge 5.5 Product Data Sheet" n.d.). Rolling shutter and global shutter modalities are available. The maximum frame rate for this camera is 100 fps using a rolling shutter and the full resolution of 2560×2160 pixels (400 fps can be reached by reducing the active sensor area to 640×480 pixels). The fastest optic fibre Camera Link HS interface will be used for connecting the camera to the

data acquisition system. The cameras should be interchangeable within all detectors thanks to identical F-mounts. Snapshots of the available field of views at 43m from the photon source are shown in Figure 82, when using a pco.edge 5.5 and for detector magnifications between 2× and 10×.

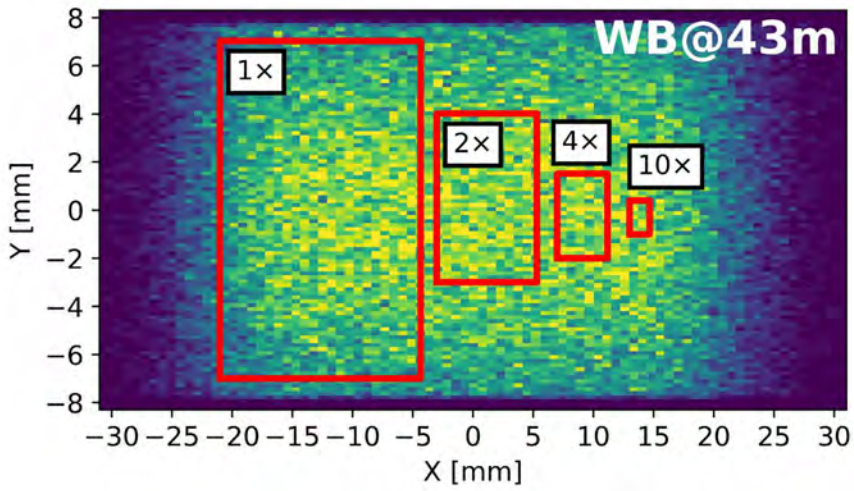

Figure 82: Field Of View (FOV) available with different objective magnifications and considering a 2560×2160 pixels sCMOS sensor with a physical pixel size of 6.5×6.5 μm². FOV of different objectives are overlapped to a white beam snapshot at 43m from the source.

10.4.7 Scintillators

Thin-film and polished single crystals are the most common choice of scintillator screens for micro tomography, providing minimum internal scattering of visible light within the crystal and minimizing the image blur (Cecilia et al. 2014; Douissard et al. 2010; A. Rack et al. 2008; Stampanoni et al. 2002). The choice of scintillating materials follows a compromise between the following aspects:

- The emission wavelength of the scintillating material should match the wavelength of maximum quantum efficiency in the visible light spectrum of the camera sensor. For the latest generation of sCMOS this is between 450 nm and 750 nm ("Pco.Edge 5.5 Product Data Sheet" n.d.).
- The absorption power (and therefore the visible light output) should be maximized for the working energy to make use of as much of the available X-ray photon flux as possible and minimize exposure times.
- The thickness of the scintillating screen should be optimized for the target image resolution on one hand, and maximum stopping power on the other.
- In case of time resolved experiments or fast acquisitions in general, the afterglow or decay times of the scintillator should be also considered.

Scintillating screens at BEATS will be acquired periodically to cope with degradation due to X-ray exposure. Cerium doped LuAG (Lu_3Al5O_{12}) crystal scintillators (LuAG:Ce) will be available from day one at BEATS applications requiring low magnification and medium to low exposure time. LuAG:Ce scintillators provide high stopping power over the range of X-ray energies utilized at BEATS, fast decay time and peak emission of light at 510 nm wavelength (Mittone et al. 2017). For high-resolution experiments (e.g. using the 10× microscope objective), thin-film scintillator crystals with a thickness between 20 and 30 μm are considered. These will be GGG:Eu ($Gd_3Ga_5O_{12}$ europium doped) or alternatively LSO:Tb (Lu_2SiO_5 terbium doped) scintillators (Cecilia et al. 2014). YAG:Ce ($Y_3Al_5O_{12}$ cerium doped) single crystal scintillators provide sharp radiographic images but have lower attenuation

power than LuAG and LSO (A. Rack et al. 2008). A station dedicated to the cleaning of scintillators should be predisposed in the control room or in the sample preparation area of the beamline.

10.5 Experimental hutch equipment and motorization

Table 14 presents a summary of the equipment in the experimental hutch and the number of motorized stages required. Motion control will be performed using the SESAME motion box (see motion standards in chapter 0). An air conditioning system is considered (last row in Table 14) for keeping a stable temperature inside the experimental hutch and prevent motion errors due to thermal excursion. Temperature stabilization will be particularly important at BEATS due to the environmental conditions (strong thermal excursion) of SESAME. The system should be dimensioned to attain stabilization of the experimental hutch temperature within ±1 degree Celsius. Air inlets should be positioned away from the position of sample and detectors and distributed evenly throughout the experimental hutch if possible. The atmosphere of the experimental hutch must be also monitored for Ozone. Ozone monitors will be interlocked with the PSS system granting access to the experimental hutch and ventilation for Ozone extraction will be installed. One or more CCTV cameras will be used to survey the position of the equipment inside the experimental hutch. Additional cameras can be installed for remote feedback on the position and alignment of the sample and of the detector. Limit switches and interlocks for equipment and personnel safety will be installed to prevent collision of and with motorized parts.

Equipment	N. of axes	Along axis	Encoder	Comment
Support and gate valve				Include ion pump
Secondary slits table	1	Y	Yes	Vertical motorization
Secondary Slits	4	X/X/Y/Y/	Yes	
Second Window				Can include cooling
Alignment System	1	X	Limit switches	
Fast shutter table	1	Y	Yes	Vertical motorization; can support flight pipe
Fast Shutter	4	Y/Y/Y/Y	No	Linear brushless motors
Tomographic sample stage	5	X/Y/ω/X/Z	Yes	
Optical table				
Detector Stage	4(5)	X/Y/Y/Z/(Z)	Yes	Step motors
White-beam microscope	5	Objective selection	Yes	Step motors
		Objective focus	No	
		Objective focus	No	
		Objective focus	No	
		Camera alignment	No	
Low magnification detector	2	Objective focus	No	Step motors
		Camera alignment	No	
	2	Objective focus	No	Step motors

Monochromatic HR microscope		Camera alignment	No	
Beamstop				
Air conditioning				
Ozone extraction system				Ozone monitors connected to PSS
CCTV cameras				

Table 14: Experimental hutch equipment with information on motorized components.

11 Beamline Control, Data Acquisition and Management

Computed tomography beamlines are among the most massive data generation beamlines in synchrotron radiation facilities, where a single experiment can generate up to 2 Terabyte of raw and processed data. Accordingly, high-end computational and network resources are required to carry out the scientific research activities on such beamline. In this chapter we describe the computational infrastructure needed to commission and operate BEATS by following well established computing infrastructure models in similar laboratories, for instance ESRF and PSI.

Experimental computed tomography data consist of large sets of raw data that need to be computed and stored in order to let users take home the fully processed data sets (reconstructed images and 3D volumes) as soon as the experiment is completed. The computing and networking infrastructure of BEATS will address the demanding handling (pre-processing, reconstruction, and storage) of computed tomography experimental data in full compliance with the SESAME Experimental Data Management Policy.

The BEATS consortium is committed to establish *Data Analysis as a Service* as one of the project's objectives. The possibility to offer data analysis as a service on a permanent basis and after the conclusion of the BEATS project depends on the installed computing infrastructure as well as on the resources (e.g. experienced staff, computing nodes) available at that time. From the day-1 of the operation of BEATS, this service should be understood as provided on a best-effort basis and for a limited period. In this sense, the possibility to extend user access to the computing infrastructure described below beyond the termination of the beamtime will depend on the resources available at the time.

11.1 Pipeline for data acquisition, processing and storage

The pipeline of the BEATS data acquisition, processing and storage infrastructure is illustrated in Figure 83.

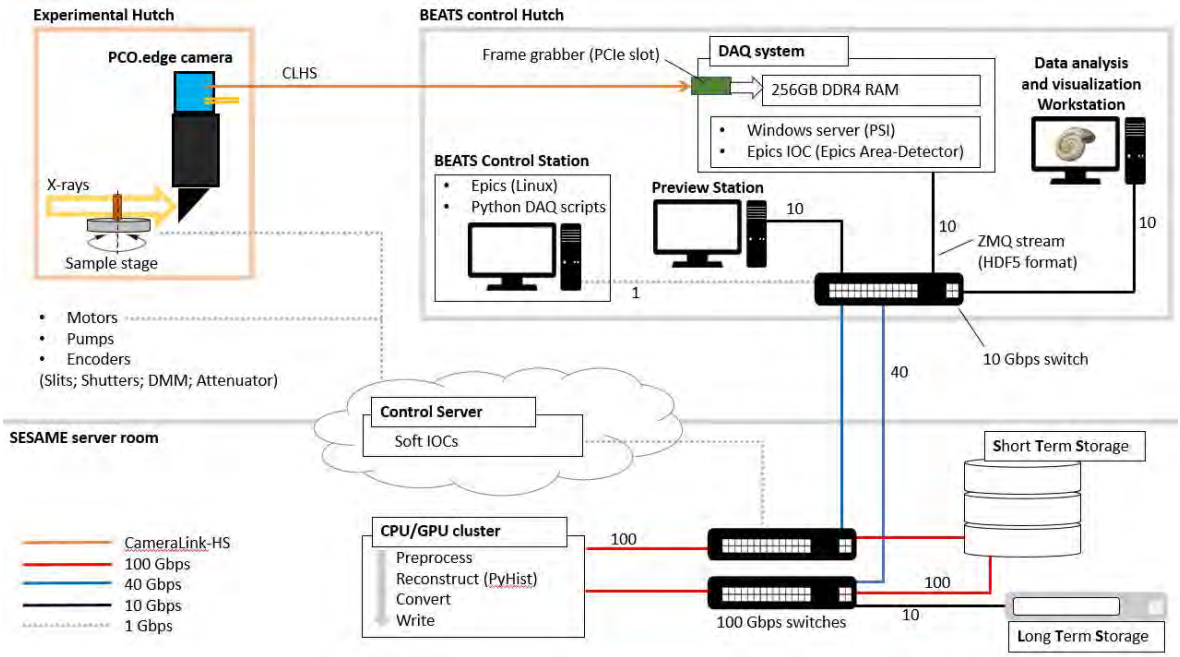

Figure 83: Computing infrastructure for the BEATS beamline control and data acquisition system.

11.1.1 Data Acquisition system

From a computational point-of-view, the tomography data acquisition process starts by collecting single frames (radiographic projections) from a high-speed sCMOS-sensor camera and transferring them to a Short Term Storage (STS) server. This process is carried out by a back-end Data Acquisition (DAQ) system located in the beamline control hutch. The DAQ system is integrated into EPICS, the Experimental Physics and Industrial Control System (Advanced Photon Source, Argonne National Laboratory, Argonne, IL 60439, USA) via a Windows or Linux server running an EPICS Input/Output Controller (IOC). Raw data is transferred from the camera to the DAQ system via a Camera Link HS (CLHS) cable interface with dedicated PCIe frame grabber. The DAQ system outputs a stream of data which is written to the Short Term Storage in one single, HDF5-format file using the ZeroMQ distributed messaging protocol ("The ZeroMQ Project" n.d.). The file written to the STS contains RAW projections as well as experimental metadata compliant with the SESAME Experimental Data (SED) internal standard. The EPICS Area-Detector framework is the primary software for detector control which includes drivers, post-processing plugins, data format manipulation libraries and data visualization.

As a tentative hardware definition, the DAQ system will be equipped with 8 cores CPU, 128 or 256 GB of RAM, 10 Gbps network card, 512 M.2 SSD and 2 TB HDD.

We have calculated the expected performance of the data acquisition system when images are streamed to the RAM of this system by a 2560×2160 sCMOS sensor camera (PCO.edge5.5) with Camera Link HS interface and operated in fast scan mode: results are reported in Table 15.

Pixels X	2560	2560	2560
Pixels Y	2160	1024	512
Dynamic range A/D	16 bit		
Fps (fast scan; rolling shutter)	100	212	422
GB/s	1.1		
GB/min	66.4		
Single scan duration [sec] (1000 projections)	10.0	4.7	2.4
max. Stream time with 128GB RAM [s]	104		
max. N. of tomographic scans with 128GB RAM	10	22	44

Table 15: Expected data stream (max. acquisition time and total number of tomographic scans) for a PCO.edge5.5 camera streaming data to a 128GB RAM data acquisition system. The table illustrates the limit case of a time resolved scan at the maximum camera frame rate.

11.1.2 Beamline Control Station

The beamline staff and users will control the experiment from the BEATS control hutch. Existing control software currently in use at the PSI's TOMCAT beamline will be adapted to BEATS. The control station will allow the control of the data acquisition system and of the equipment in the experimental as well as optics hutch and of the Front end. Hardware information and settings will be accessed and controlled through EPICS within a Linux environment. Python DAQ scripts will use PyEpics: the library for EPICS Channel Access for Python developed by the GSECARS team at Argonne ("PyEpics Overview — Epics Channel Access for Python" n.d.).

Before and during raw data acquisition, the DAQ system and the beamline control station must exchange information such as scan parameters and triggers for the start and end events of the data acquisition. The communication between DAQ system and beamline control station will occur through EPICS channel access protocol.

Beamline control station hardware definitions: Intel i7 9th gen., 16 GB RAM, 240 GB SSD, 1 TB HDD, basic graphics card and 2 x 32" screens.

11.1.3 Hybrid CPU/GPU reconstruction cluster

The pre-processing and reconstruction of the raw data (2D projections) will be performed on a dedicated hybrid CPU/GPU cluster. We will use a high performance, distributed code like PyHST2 (Mirone et al. 2014) or Nabu ("Nabu 2020.1.1 — Nabu 2020.1.1 Documentation" n.d.) for the volume reconstruction. PyHST2 and Nabu are developed by the ESRF and offer analytical and iterative approaches for tomographic reconstruction. Methods for artifact correction and phase retrieval are implemented. The interaction with these packages is command-line-based and requires some understanding of the Python programming language. We will implement several strategies to facilitate the control of the reconstruction process even by less experienced users. In order to encourage users to actively interact and perform reconstructions in Nabu, we propose to use TOMWER ("TOMWER — Tomwer 0.5 Documentation" n.d.), which provides a graphical user interface to the reconstruction workflow based on the intuitive orange toolkit (Demšar et al. 2013). For users with some experience in Python, we will provide a Wiki and a set of Jupyter notebooks illustrating the main steps of the process. Finally, software providing a dedicated Graphical User Interface will be also installed on this system. As an example of such alternative for user-friendly interaction with tomographic reconstruction is the Syrmep Tomo Project (STP) software (Brun et al. 2017).

The hybrid cluster can additionally be used for in-house as well as remote data analysis, providing a basic and appropriate set of 3D data analysis tools. By comparing the currently available technology with what might be state of the art in three years (i.e. when the beamline is in operation) and by consulting specialists in the field, we anticipate that the cluster will consist of 4 computing nodes, dual CPU sockets each, 18 actual cores for each CPU, 8 GB RAM for each core. On the other hand, for the computational GPUs computing power, two nodes will be equipped with 8 TFLOPS accelerator cards.

11.1.4 Preview and on-the-fly visualization station

Preview and on-the-fly visualization of a set of projection images during time resolved scans can be implemented on a separate system (Preview Station in Figure 83) to be hosted in the control hutch Alternatively to a dedicated system, preview functionalities can be implemented directly on the hybrid cluster and streamed to a standard workstation in the BEATS control station.

Preview system hardware estimate: 8 cores CPU, 32 GB RAM, mid-class graphics card, 10 Gbps network card, 1 x 32" 120 Hz monitor and 512 GB SSD

11.1.5 Short Term Storage server

A high-end experimental data storage will be connected to the hybrid CPU/GPU cluster over 100 Gbps interconnect. This storage will be used as a centralized Short-Term Storage to keep the raw and reconstructed data for a certain time in compliance with the SESAME Experimental Data Management Policy. The storage size and specifications for STS have been discussed during a meeting of BEATS WP4/WP7 and PSI beamline and IT experts, held in June 2019, where the size of the STS was estimated to be 0.5 PB with General Parallel File System (GPFS) or Lustre file system installed, however, PSI and ESRF recommend using GPFS. For the sake of storage space optimization, only the raw data (projections) might be archived in the STS. The beamline users will have the opportunity to reconstruct and take home after the beamtime tomographic reconstructions in Tagged Image File Format (TIFF) with the desired resolution.

11.1.6 Long Term Storage

After the initial period, all RAW data stored in the STS will automatically be archived on tapes in the Long Term Storage (LTS) pool. Tape drive archiving will allow to maintain the RAW data for a minimum of 5 years in compliance with SESAME Experimental Data Management Policy.

11.1.7 Network connection components

To connect all systems, sub-systems, components and modules, a dedicated network with adapted bandwidth is needed. Currently, the capacity of the SESAME backbone network is 10 Gbps, which is not sufficient for the BEATS data handling and evaluation. Consequently, a general network layout is proposed as shown in Figure 84: the DAQ and the data analysis work station will be connected via a 10Gbps switch. This 10 Gbps switch will be directly connected to the data centre switches over a 40 Gbps uplink interconnect. The data centre switches will mainly be used to interconnect the GPU/CPU and storage nodes at 100 Gbps speed, the beamline switch at 40Gbps speed and the rest of the SESAME network at 10Gbps speed.

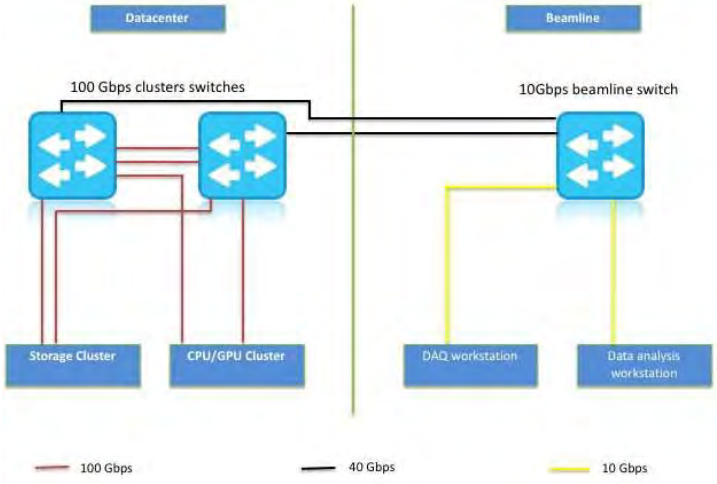

Figure 84: General network chart at beamline and data centre

11.1.8 Data analysis and visualization workstation

SESAME and The Cyprus Institute (CyI) will provide tomography Data Analysis as a Service across two different geographical locations, one at the SESAME premises (workstation situated in the beamline control hutch) and another at CyI. The analysis and post processing of microtomography datasets is computationally intense and relies on high-performance 3D visualization and rendering as well as on sophisticated analysis tools. However, the learning curve for a single, unexperienced user can lead to data processing periods of weeks or even months, substantially exceeding the time allocated for an experiment. Correspondingly, high-end data analysis workstations with big RAM, powerful CPUs and GPUs will be required. Tentative specifications of each of these systems are: 16 cores, 512 GB RAM, 1 TB M.2 SSD, 2 TB HDD, 10 Gbps network card, 6 GB pro graphics card, USB 3 ports, 2 x 32" screens. The main system will be installed in the control hutch of BEATS. A twin system of the same kind, also dedicated to the BEATS users, can be installed in the premises of the CyI. These workstations will be equipped with preinstalled 3D data analysis and visualization applications. According to the community needs, the BEATS workstation will be available for data visualization and analysis during user beamtime. At the same time and depending on the availability of resources and in a best-efforts basis, access to both systems can be granted for offline tomography data analysis from the user's home institute.

11.2 Hardware and software requirements

An estimate of the hardware and software requirements for the implementation of the data acquisition, analysis and management systems described in this chapter was prepared within the activity of the BEATS Work Package 7 (Data analysis and management). Hardware and software definitions for BEATS are described in deliverable D7.1 "Report on the required hardware and software for the tomography beamline" of this work package (Chrysostomou et al. 2020).

11.2.1 From computed tomography data to simulations with the finite element method

In addition to a sample environment for mechanical testing, BEATS will provide its users with software tools for simulating non-destructively the application of external fields (e.g. mechanical stress) to the sample. In recent years, the combination of FE analyses with high resolution computed tomography at synchrotron facilities has been applied to study a wide range of geology, materials science, biology and engineering problems. Numerical simulations can complement or substitute sample environment equipment, which is expensive, requires complex installation and often involves the damage of samples. The finite element technique was applied so far to understand failure and hardening processes in steal foams (Kaya et al. 2018), damage mechanisms of bast fibres (Guessasma and Beaugrand 2019), mechanosensation (Varga et al. 2014) and modelling (Ofer et al. 2019) of bone, gas exchange dynamics in alveolar structures (Tsuda et al. 2008) or to guide the design of cellular materials (Wan et al. 2019). As an example, Figure 85 illustrates a finite element simulation of a mechanical test of a bone sample. The simulation was obtained from a synchrotron computed tomography scan. The possibility to work with monochromatic radiation provides beam-hardening-free, quantitative images, which can be converted to accurate maps of the local tissue density (Figure 85A). This is done either by direct conversion of the attenuation coefficients to density values, or by calibration with phantoms of known materials. BEATS will provide software tools for the semi-automatic generation of finite element simulations based on 3D computed tomography datasets. Commercial FE solvers for the solution of such models will not be available at BEATS. The input file for the FE simulation will be portable, allowing the computation of FE simulations by users on clusters or workstations at their home facilities.

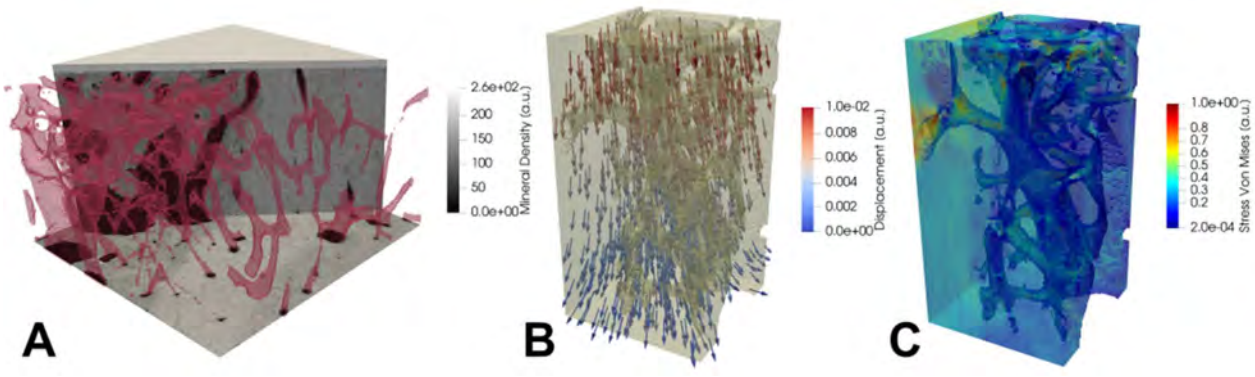

Figure 85: Finite element simulation of a rat bone sample under mechanical compression derived from synchrotron tomography data. (A) Voids (red) and open struts are segmented and removed from the model. Local X-ray attenuation coefficients are converted to mineral density and two layers of embedding material (grey) are added. Image voxels are directly converted to hexahedral finite elements whose material properties are mapped based on the local density. (B) Simulated displacement field (axial compression) through a portion of the sample. (C) Equivalent Von Mises stress field revealing stress concentration around the porous structure. ID19 (ESRF) data courtesy of Prof. Kay Raum.

11.3 Data Management and Curation

All BEATS raw data and associated metadata (experimental data) will be stored at SESAME for a minimum of 5 years, with SESAME striving to guarantee storage for up to 10 years. The actual storage period will depend on the type and volume of the experimental data as well as on the available infrastructure. Thus, SESAME reserves the right to shorten the storage periods and/or reduce the number of data sets for a high data rate instrument such as computed tomography, after consultation with the pertinent communities and with the principal investigators (PI) involved.

Access to the experimental data will be restricted to the experimental team for 3 years after the end of the experiment. After these 3 years, all available data will be openly accessible to the users registered on the SESAME database. Only the SESAME director can give permission to keep data under restricted access for an extended period on an exceptional basis.

Experimental data access will be possible via an online searchable catalogue. Access to the online catalogue will be restricted to users registered in the SESAME's database. SESAME will provide an online procedure to register as a user of its online catalogue.

Authorized SESAME staff (e.g. instrument scientists, members of the computing group) will have access to any set of SESAME-curated data or metadata for facility-related purposes. SESAME will use multiple measures to ensure and preserve the confidentiality of the data for the entire storage period. Unless otherwise authorized by the PI, access to proposals will only be provided to the experimental team and appropriate facility staff. Also, the PI will have the possibility of creating and distributing copies of the raw data.

All experimental data will be curated in well-defined formats. Tools for data read will be provided to the users for the whole lifetime of the dataset. Metadata that are automatically captured by instruments will be curated either within the raw data files or within an associated online catalogue, or both. Raw data and metadata will be migrated or copied to archival facilities for long-term curation with a unique persistent identifier. The high-level metadata such as Title, Authors, Abstract, and Beamline will be made public as soon as the experiment has been carried out. This information will be available via the persistent identifier landing page on the web.

The data curation rules described above will not apply to experimental data arising from proprietary and industrial research or from research carried out by Participatory Research Teams (PRTs).

11.4 Synergy between BEATS and The Cyprus Institute (CYI)

11.4.1 Network connectivity

The CyI currently has a direct 0.6 Gbps internet connection, with plans for an upgrade to 1.0 Gbps by the end of 2021. The CYI is part of CYNET (Cyprus Research and Academic Network), and this Cypriot NREN (National Research and Education Network) is in turn a national member of the pan-European GÉANT network. SESAME forms part of the JUNet (Jordanian Universities Research and Learning Network), and this Jordanian NREN is in turn a member of ASREN (Arab States Research and Education Network). Both networks, the GÉANT through CYNET and ASREN through JUNet will be utilized to optimize the transfer of data between the CyI and SESAME.

11.4.2 Storage and Computational Infrastructure

The CyI currently operates the CY-TERA supercomputer with peak / sustained performance of around 600 TFlop/s, and 33 nodes available. (17 nodes with two Intel Xeon Gold 6248 each and 16 GPU nodes with two Intel Xeon Gold 6248 and 4 NVIDIA Tesla V100 SXM2 32 GB each). The memory on the

compute nodes is 96GB and on the GPU nodes 192GB). The system also has a HDR100 Infiniband and 135TB of flash storage for temporary storage and more than 20PB for long term storage.

Two access modalities to the storage and computational infrastructure will be available within the BEATS project: preparatory and production access. Preparatory (on-demand) access will serve for the development and testing of codes required for the project and will be granted to CyI and SESAME staff. Production access to the computational resources will be allocated to the users of SESAME for the implementation of their scientific projects and for the analysis of data collected at BEATS. Every six months, an estimation will be established for the expected users for computational resources and storage, and the available resources will be adjusted.

More information on the two access modes can be found at: http://bit.do/cyi_access

12 Radiation Safety

12.1 Radiation protection

Appropriate radiation shielding will assure the limitation of the exposure to ionizing radiation of staff members as well as visitors, researchers and in general of the environment surrounding the SESAME premises to legally defined values. Furthermore, the technical design of the radiation shielding for any new beamline installed at SESAME (or equipment therein) must comply with the SESAME safety policy. Radiation shielding at SESAME has to be installed following the prerequisites of the Local Jordanian Law of Radiation Protection (Nuclear Safety and Security Law No. 43 for the year 2007 and its amendments). The expected dose received by staff members and users must be less than the dose limit for the general public for 2000 working hours. This necessitates shielding measures which assure reduce that the dose rate to values below a maximum of 0.5 µSv/h under normal operation conditions.

To comply with the aforementioned legal regulations and to achieve the goal of sufficiently low dose rates outside the beamline's hutches in the experimental hall of SESAME, Monte Carlo calculations using the well-established FLUKA software suite were carried out to determine the required thicknesses of the lead walls of the hutches, as well as the position and thickness of additional shielding elements like collimators or beam stops. Input parameters are the storage ring characteristics (electron energy, max. current in the machine, straight section average pressure), and the beamline overall configuration (scattering elements, vacuum levels). As both BEATS hutches may receive white beam, both are treated as optics hutches.

Particular attention was paid to the proper shielding of gas bremsstrahlung, originating from residual gas molecules in the storage ring straight section, and its scattering from, for instance, the first multilayer element of the monochromator. Precise raytracing calculations were to be carried out to determine the position and opening of collimators to prevent scattered bremsstrahlung reaching beam pipe walls etc. where further cascades could be produced. In the same sense, the calculations yielded the necessary dimension of, for instance, safety shutter and the bremsstrahlung stop at the back wall of the experimental hutch.

A report on the specifications for the BEATS radiation protection hutches based on the results of these calculations, BEATS deliverable D.4.2., was submitted on 31st July 2020. In this document, the ALBA Radiation Protection Service established the shielding requirements for BEATS in accordance with SESAME's exposure limit and geometrical constrains of the Experimental Hall and the other boundary conditions known at the time. D.4.2. as well provides a detailed description of the methodology used to establish radiation protection requirements for the BEATS hutches.

The main conclusions derived from deliverable 4.2 are:

- Radiation levels outside the enclosures are dominated by the gas bremsstrahlung contribution, produced when the SR electron beam interacts with the residual gas molecules present inside the ID straight section vacuum chamber.
- The radiation levels outside the Optic Hutch (OH) enclosure reach their maximum for the high energy monochromatic beam scenario.
- The Transfer Line (TL) shielding is limited by doses produced under a vacuum loss accidental situation only if solid scattering against the vacuum chamber pipe can be avoided. The proper thickness for the TL shielding must be derived for this scenario only if no optical elements are installed inside the TL and a proper Limiting Raytracing analysis is provided.

- Dose levels around the Experimental Hutch (EH) were characterised for the case in which the white beam reaches the beam stop placed at the end of the enclosure. A local shielding for this beam stop was designed.

Since the delivery of the document, triggered by a modification of the layout of the hutches during the month of July 2020, in addition to the necessary repetition of the aforementioned calculations, further studies have been carried out. In particular, efforts have focused on:

- Analyse with precision the beam path along the optics and produce Limiting Raytracing drawings. These drawings allow to determine if the use of additional screens, beam stops and collimators is necessary. In the case of BEATS, this is a critical work that allows ensuring that no scattered rays originating from the main scattering points inside the Optics Hutch (OH) will be able to hit the transfer line vacuum chamber, thus avoiding the possibility of solid bremsstrahlung interactions outside of the hutches that will be difficult to shield.
- Study the radiation interactions at the sample environment inside the Experimental Hutch (EH). This investigation is a critical one for any BL aiming at using white beam in air, constituting in fact the most restrictive scenario in terms of shielding for the Experimental Hutch.

In what follows we describe the final shielding design of the BEATS Optics and Experimental Hutches. The design reported below should be considered as an extension and modification of the hutches design reported in D.4.2.

12.1.1.1 Final shielding design for the Optics Hutch

The limiting raytracing drawings, see Figure 86, allow to further improve the design of the collimators initially proposed (i.e. ensure that no ray will hit the TL and reduce the total photon flux reaching the Experimental Hutch). It was found that there is no need to include a double collimation system as initially proposed, and that it is sufficient to consider one single tungsten collimator placed 29.3 cm upstream the OH back wall This single collimator should have an aperture of 22 (h) x 26 (v) mm^2 and fill the entire vacuum chamber. The use of a collimator adds a scattering element inside the OH, thus incrementing the radiation level at this hutch, but allows for a dose rate reduction of a factor 5 inside the Experimental Hutch.

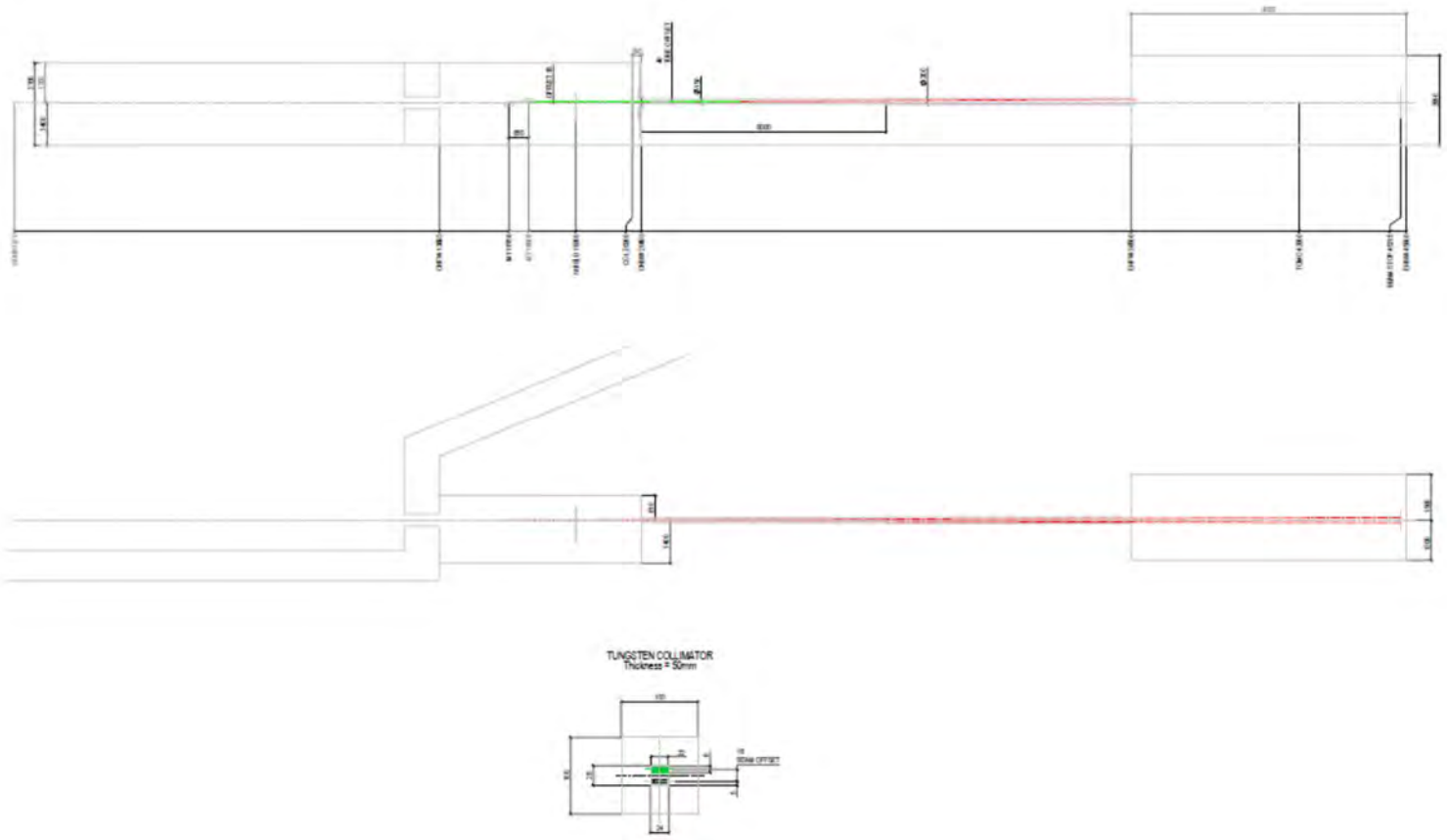

Figure 86 BEATS limiting raytracing drawing including a scheme with the internal aperture of the collimator to be used to ensure that no scattered ray hits the TL vacuum chamber

The shielding of the OH has been adjusted to cope with these increased radiation levels, and the final requirements are shown in Table 16 and Table 17. The changes are introduced mainly to cope with photon induced neutrons and can be summarised as:

- Covering the inside of both sidewalls with 100 mm PE.
- Covering the outside of the backwall with a sandwich of 100 mm PE + 5 mm Pb.
- Extending item #2 to cover the first 15 cm of the TL also with a sandwich of 100 mm PE + 5 mm Pb, placed over the already foreseen 25 mm Pb collar.

The maximum dose rate around the OH enclosure with these new requirements is 0.1 µSv/h.

12.1.2 Final shielding design for the EH

The study of the radiation interactions possible at the Experimental Hutch has been completed by including an analysis of the sample environment. The sample environment (sample + sample detector) was modelled as a Cu cubic block of 10 cm^3. Two gas bremsstrahlung white beam simulation scenarios have been run:

A. Sample placed at the beginning of the EH, next to the place where the white beam is released into air,
B. Sample placed downstream at the far end of the EH, just before the beamstop.

From the results obtained the decision was taken to move all neutrons shielding to the walls instead of shielding the beam stop locally. The modification of the shielding can be summarised as:

1. Covering the inside of both sidewalls with 50 mm PE.
2. Adding a reinforcement over the EH back wall in the form of a 1 m^2 Pb screen, 50 mm thick and centred around the projected beam impact point.
3. Covering the inside of the back wall with 100 mm PE.

The final shielding requirements for the EH are summarised in Table 16 and Table 17, the maximum dose rate under the most restrictive scenario is 0.1X µSv/h.

Element	Material and thickness (mm)
Side wall OH-I	PE 100 + Pb 25
Side wall OH-0	PE 100 + Pb 20
Back wall OH-B	Pb 60 + PE 100 + Pb 5
Roof OH	Pb 15
Front wall EH	Pb 20
Side wall EH-I Side wall EH-O	PE 50 + Pb 20
Back wall EH-B	PE 100 + Pb 60
Roof EH	Pb 15

Table 16: Summary of shielding requirements for BEATS hutches

#	Shielding Elements	Height (mm)	Width (mm)	Thickness (mm)	Material
1	Tunnel-to-OH guillotine	500	500	20	Pb
2	Local Pb screen 1 behind DMM	-	-	20	Pb
3	OH-to-TL guillotine	400	400	65	Pb
4	OH back wall central reinforcement	1000	1000	50	Pb
5	Collar around TL	-	-	25	Pb
6	Extension of the backwall neutron shield over the TL collar	Along the first 15 cm of TL		100 + 5	PE + Pb
7	Guillotines at both extremes of the TL	-	-	200	Pb
8	TL-to-EH guillotine	300	300	20	Pb
9	EH back wall central reinforcement	1500	1500	7	Pb

Table 17: List of BEATS local shielding elements with expected minimum dimensions

12.1.3 Future actions

Actions developed have been focused on providing the structural and non-structural shielding requirements needed for the tendering of BEATS enclosures that will allow minimising the ionising radiation hazard. Of course, if further changes in the BL layout are decided or the beam path is significantly changed, the requirements will have to be assessed again.

Apart from shielding requirements other ionising radiation studies are needed in the following months concerning the possible activation of the air and ozone production inside the Experimental Hutch. The handling of this activation will have no impact on the shielding itself but rather on the air ventilation system needed to evacuate the possible activations and on the control systems that regulate the access into the EH, i.e. the Personal Safety System (PSS). One may expect that some specific requirements on the PSS will be needed, for example imposing some minimum cooling time onto the access inside the EH to ensure that all activation has disappeared before allowing the entrance to the enclosure.

12.2 Personnel Safety System

Personnel safety system (PSS) operates as an access control system for the shielded enclosed areas to prevent access to dangerous levels of prompt radiation.

One of the main PSS procedures is the search of the hutches, with the purpose to make sure that all staff left before beam can enter into the hutch. To accomplish this and to make sure that all corners of the hutch in question have visited and inspected, a number of search buttons distributed in the hutch must be pressed by a person searching the hutch in a pre-defined sequence and within a minimum time, forcing the searcher to inspect the whole accessible area.. During the search procedure, the doors must remain closed, to make sure nobody enters anymore (if a door is opened during the search, the sequence has to

be restarted.). Only when the search is completed (all search buttons have been pressed, confirming that no person has been found in the respective area) and the searcher left the hutch, the Front end and subsequent beam shutters can be opened. The proposed locations of the search buttons inside the optics hutch and experimental hutch of BEATS are illustrated in Figure 87 and Figure 88, respectively.

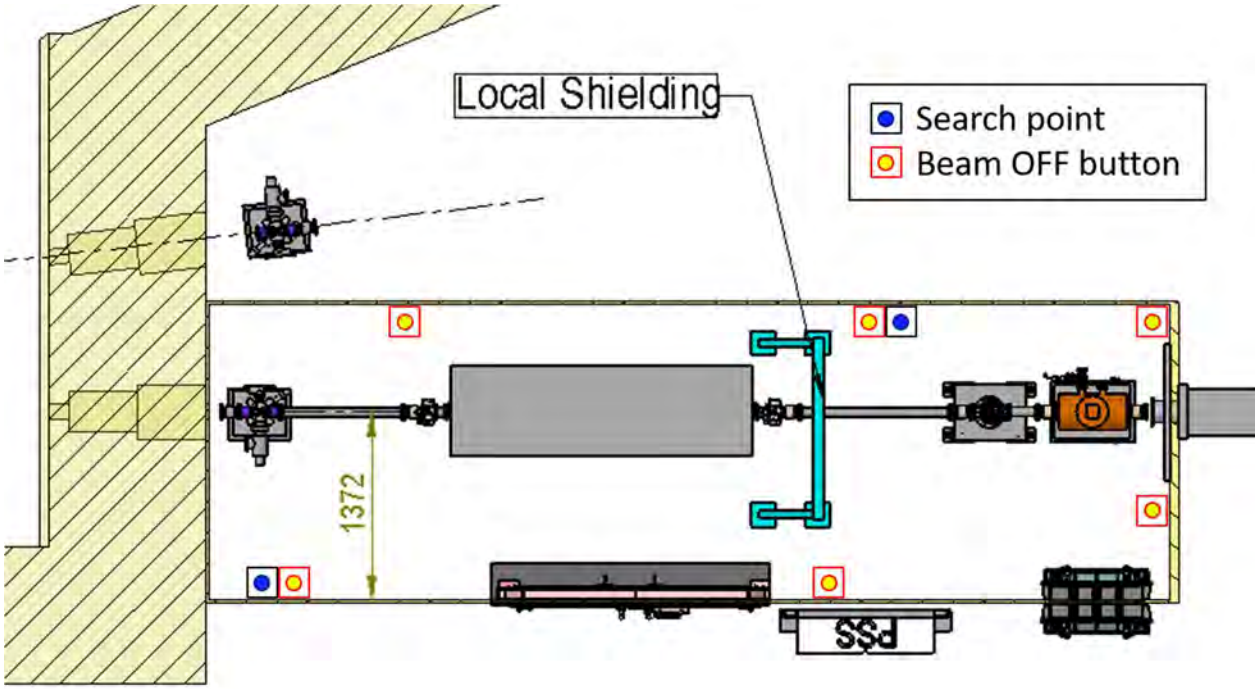

Figure 87 PSS search and beam-off buttons inside the BEATS optics hutch. Accessibility of the second search button might depend on the final size of the monochromator and other vacuum equipment as well as on the support steel frame and polyethylene shielding of the same hutch wall. Therefore, the search procedure might be reviewed after inspecting the technical offer of the radiation shielding optical hutch.

The search procedure of the optical hutch is defined as follows (the procedure for the experimental hutch will be defined following the same principles):

- STEP 1: do a pre check to make sure that there are no people inside the hutch.
- STEP 2: close the hutch door.
- STEP 3: make sure that the safety officer and coordinators keys are in ON position, then press start search button. The red warning lights in the hutch will start blinking with variable tone audible warning to notify personnel that a search is in progress.
- STEP 4: open the door, go inside the hutch then close the door. If you or someone opened the door after this step and before finishing the search, the search will fail and you have to repeat the procedure.
- STEP 5: Go to the first search point, look for people, if there are no people then press Search Button 1.
  Note: The blinking frequency of the search buttons will change and become faster after a certain time, you can then press the button.
- STEP 6: Go to the second search point, look for people, if there are no people then press Search Button 2.

- STEP 7: after searching the hutch and press all the buttons, Leave the hutch and close the door, the door will be locked automatically.
- STEP 8: Press finish search button. The audible warning changes to an intermittent tone before enabling the shutters permits.

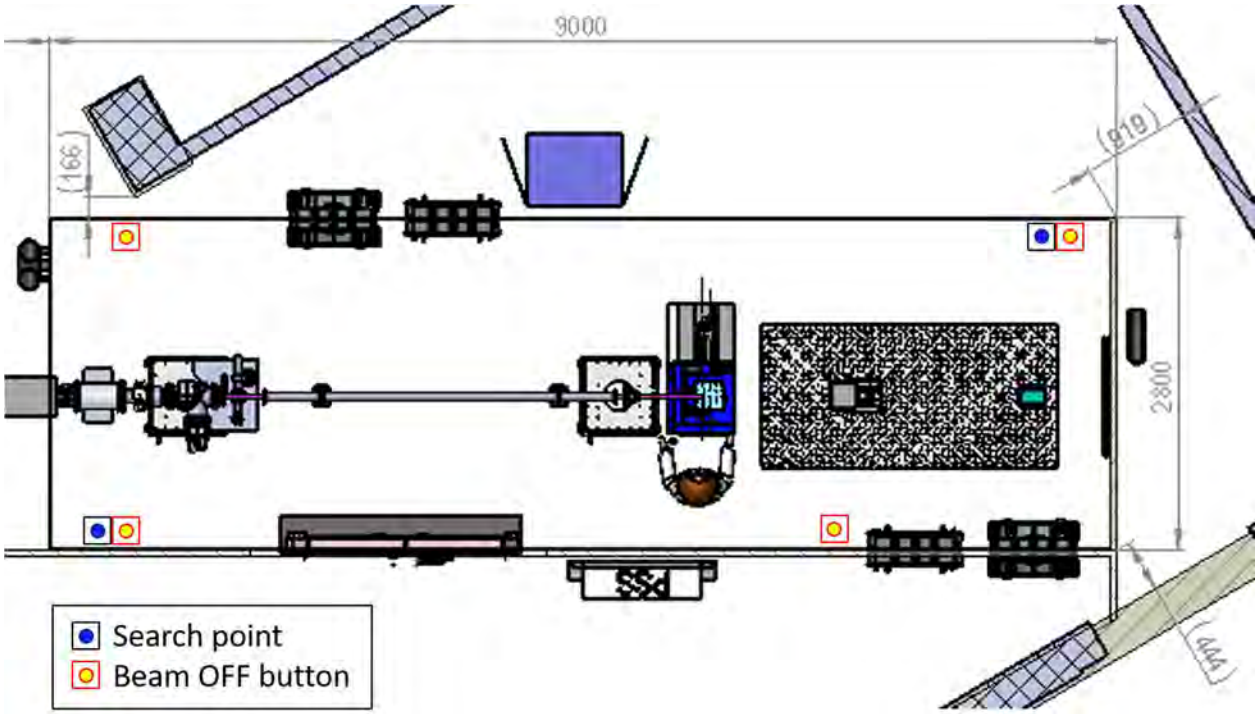

Figure 88: Proposed PSS search and beam-off buttons in the BEATS experimental hutch.

13 Risk Analysis

When the BEATS consortium applied for the H2020 grant in spring 2018, a risk analysis was carried out for the whole project. This analysis has now, as the project is running for 20 months, been thoroughly reviewed. For each identified risk, its

- likelihood and
- impact (which together indicate the risk's seriousness) as well as
- possible mitigation actions

were evaluated.

While some risk initially assumed to be of a certain importance did not materialize and were removed from the list, the pandemic situation of course added new operational risks that need to be monitored carefully during the remaining duration of the project. The mitigation measures to be taken, should these risks materialize, include calling for a prolongation of the project duration. Table 18 lists the identified risks relevant for the technical operation of the BEATS project.

	Risk	Likelihood	Impact	Score	Mitigate / accept	Mitigation measures
1	Delay in / difficulties with procurement of critical beamline components	1	3	3	mitigate	The project has established a Procurement Advisory Board, collecting experience of the leading SR facilities in Europe in procurement of SR related goods, which will assist SESAME in setting up and following up the associated Calls for Tender.
2	Delay in delivery of beamline components	2	3	6	mitigate	Most of the beamline components are standard and based on well-established technology. The aforementioned Purchasing Advisory Board will ensure that only highly experienced companies will be consulted for CfTs. The respective contracts will be closely followed up with regular visits by experts from the BEATS consortium to the suppliers.
3	Difficulties to motivate staff from European facilities to support SESAME staff in Jordan	1	2	2	mitigate	The consortium is sufficiently large to either resort to not yet identified staff from the RIs participating in the assembly and commissioning of the BEATS beamline (ALBA-CELLS, ELETTRA, ESRF, SOLARIS) or from the other RIs (DESY, INFN, PSI)
4	Delay of the whole project due to the pandemic situation: Delay of delivery of beamline components beyond risk 1	3	4	12	mitigate	Enhance even further monitoring of CfTs (keep in touch with possible suppliers and stay updated on the Corona-induced consequences for them) plus: prepare to request prolongation of the project.
5	Delay of the whole project due to the pandemic situation: travel ban prohibits active participation of BEATS partners in assembly and commissioning on site	3	3	9	mitigate	prepare assembly on BEATS partners' sites, prepare concepts for remote participation in commissioning, special training of SESAME staff
6	Partners withdrawing from the Consortium	2	2	4	mitigate	overlapping expertise within the Consortium allows for re-distribution of tasks and resources over remaining partners

7	Lack of interest by SESAME User Community	2	3	6	mitigate	Since the beginning of the project there is a well-documented strong interest from the Cultural Heritage and Archaeology Community. Several user community building events to expand the pool of potential BEATS users are planned. The outcome of a recent user community building event hold within the 45th INSC meeting in Pakistan was extremely positive, with several attendees approaching the BEATS speakers after the meeting with proposals for participation and expressing their interest in the project. This approach will be intensified with more meetings dedicated to the local communities of all SESAME members. In addition, the beamline layout allows for further upgrades to host a variety of experimental techniques other than tomography.
8	Failure to secure funding to guarantee medium- to long-term sustainable operation of the SESAME facility	2	3	6	mitigate	Active dissemination to raise awareness of the uniqueness of the SESAME facility in the region. Collaboration between the European RIs involved in BEATS as well as beyond will strengthen ties between those and SESAME, highlighting the latter.
9	Specification of major optical component (DMM, Multilayers) not met	2	2	4	mitigate	thorough technical evaluation of CfT bids, in particular experience of bidding suppliers. In case of multilayer performance: Trade in spatial resolution for flux during the first operation period.
10	SESAME site internet connectivitiy not reliable or sufficient	2	2	4	mitigate	monitor early in the project, identify alternate means of data transfer (fedex hard disks), raise awareness of network carrier
11	Establishment of beamline control system difficult	2	2	4	mitigate	EPICS being used as SESAME needs adaptation, no complete new installation, thorough training on tomography specific software at PSI

Likelihood figure:

- 1 = “rare“ (probability < 20%)
- 2 = “possible“ (20% < probability < 50%)
- 3 = “likely“ (50% < probability < 80%)
- 4 = “frequent“ (80% < probability)

Impact figure:

- 1 = insignificant
- 2 = moderate
- 3 = major
- 4 = catastrophic

Score: Likelihood x Impact. Risks showing score values equal to and larger than 9 are considered as serious and will have to be monitored closely by the overall BEATS management.

Table 18: BEATS Risk Analysis as of August 2020

14 Timeline

The original time schedule for the BEATS project was inspired by the general beamline construction project planning established at the ESRF during its recent beamline upgrade programme (ESRF EBS phase I), see Figure 89:

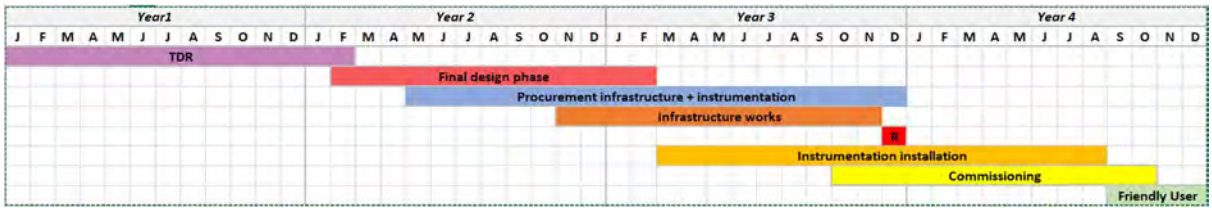

Figure 89: Original overall timeline of the BEATS project

The first year was foreseen to produce the Technical Design Report, to be followed by a "Final design phase" during the second year, concentrating mostly on the equipment of the experimental hutch. The second year would as well be dominated by the major procurement activities (Infrastructure, in particular radiation protection hutches, and instrumentation). Year three marks the installation of all equipment (with the successful radiation test at the end) and year four the commissioning and the handover of the beamline to the first users.

For BEATS it has to be noted that

- the x-ray source as well as the front end are to be included in the design phase, as no standard components are available at the SESAME site that one could make use of.
- Furthermore, all infrastructure related to the handling and analysis of the considerable amount of data generated by a tomography beamline has to be i) specified and ii) tailored to the SESAME computing infrastructure, which, at the start of the project, is not prepared to respond to the BEATS beamline's needs.
- A more general procurement strategy has to be established making use of the expertise of the BEATS partners, which can then be utilized by SESAME for later beamline projects.

It was thus decided to follow the general, more detailed timeline laid out in Figure 90

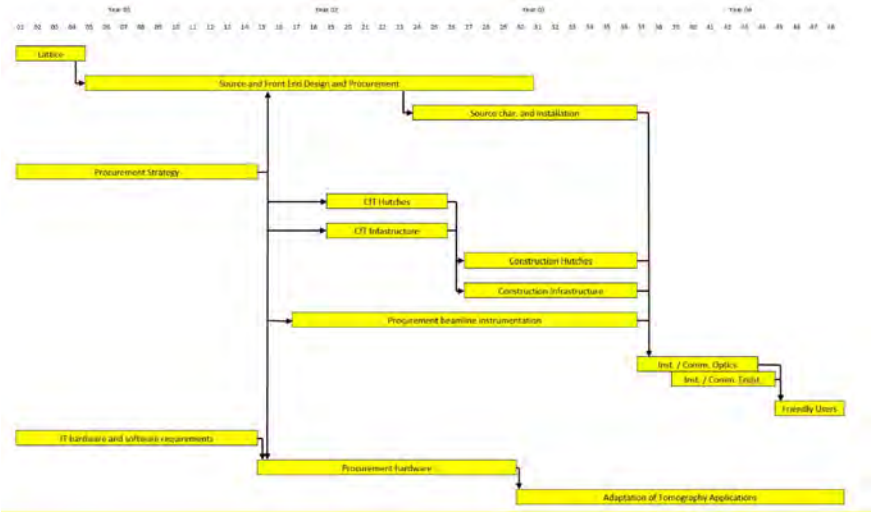

Figure 90: Interplay of BEATS procurement and installation activities

At the time of writing this document, 19 months have passed, practically all work packages (except for those dealing with the installation and commissioning) are active. The detailed planning for the upcoming BEATS activities is shown in Figure 91.

The procurement of the x-ray source was launched in May 2020, it is foreseen to place the contract by the end of October 2020.

In autumn 2020, a series of other major procurement activities will start, concerning the front end, the radiation protection hutches, the technical infrastructure, the double multilayer monochromator, and later this year, the equipment of the experimental hutch (sample and detector stages and equipment).

We expect to have the source delivered during late spring 2021 to be able to characterize the magnetic properties by June 2021 and to start commissioning on site end of 2021. The front end specifications are ready, the delivery date should allow installation during late summer 2021 to be in line with the commissioning of the source.

Similar dates are expected for the procurement and installation of the radiation protection hutches: CfT in autumn 2020, installation spring/summer 2021, successful radiation test together with the first steps of the x-ray source and front end (filtered white beam).

In parallel to these activities, the necessary technical infrastructure will be established at the SESAME site.

The delivery of the major optical element of the beamline, the double multilayer monochromator is expected by autumn 2012 at the latest, to allow start of commissioning with beam immediately after the commissioning phase of x-ray source and front end.

The last year of the project will as well see the installation and commissioning of the equipment installed in the experimental hutch, foreseen to be terminated after summer 2022. This will be the moment when the beamline will receive the first friendly users and carry out experiments that finalize the commissioning and establish the achieved day-1 performance figures.

All necessary hand- and software for the analysis and handling of the data generated by the BEATS beamline will be procured, adapted, and commissioned in parallel to the aforementioned activities.

			BEATS timeline																				Major procurements / installations						
	Date	Month	Selected Tasks and their duration																										
			T2.1 SC, UCB	T2.3 Staff training	T2.4 Stewardship	T3.2 Source and FE: design & procurement	T3.3 source charact, full installation	T4.1 TDR	T4.2 RadProtCalc, Specs hutches	T4.3 detailed TD for instrumentation	T4.4 procurement instrumentation	T4.5 Assembly b/I components	T5.1 CfT RadProtHutches	T5.2 Construction RadProthutches	T5.3 CfT Technical Infrastructure	T5.4 Construction technical Infrastructure	T6.1 Installation, comm. Optics	T6.2 Installation, comm. Exp hutch components	D7.2 Hard-Software requirements	T7.3 procurement hardware	T7.4 tomo applications and data pilelining	T7.5 DAAS	X-ray source	Front-End	Radiation Hutches	Technical Infrastructure	DMM, Optics	Experimental station	Data handling
2020	31/07/2020	19																					deadline CfT	Specs ready	Specs ready	CfTs start			finalize HW, SW specs
	31/08/2020	20																									finalize specs	finalise specs	
	30/09/2020	21																							CfT lauched	CfT launched			
	31/10/2020	22																					contract placed				CfT launched		
	30/11/2020	23																										start procurement	
	31/12/2020	24																						Contract placed					
2021	31/01/2021	25																							Contract placed	Conracts placed			
	28/02/2021	26																											
	31/03/2021	27																											
	30/04/2021	28																											
	31/05/2021	29																											
	30/06/2021	30																					Magnets characterized						HW delivered
	31/07/2021	31																											
	31/08/2021	32																											
	30/09/2021	33																									delivery		
	31/10/2021	34																											
	30/11/2021	35																							Installation done	contruction finished			
	31/12/2021	36																					start commissioning	start commissioning					
																									Radiation test				
2022	31/01/2022	37																											
	28/02/2022	38																					end commissioning	end commissioning					
	31/03/2022	39																								acceptance test		installation starts	
	30/04/2022	40																											
	31/05/2022	41																											
	30/06/2022	42																											DAaS available
	31/07/2022	43																									commissioned		
	31/08/2022	44																										end commissioning	
	30/09/2022	45																											
	31/10/2022	46																										First friendly users	
	30/11/2022	47																											
	31/12/2022	48																											

Figure 91: Detailed planning of BEATS procurement, installation, and commissioning from M19 (31/08/2020) onward

15 Budget

The overall budget estimate for BEATS is presented in Table 19. It is in line with the initial estimate established at the time of submission of the BEATS grant application. The initial figures were refined by pre-qualification visits to well established market participants and by consulting the BEATS partners for their experience with recent procurements.

Item	Budget (kEUR)
X-ray source (3-pole wiggler)	400
Front-end (incl. crotch absorber, fixed mask, XBPM, vacuum fast shutter, CVD window, primary slits, photon shutter, white beam attenuator, bremsstrahlung stopper, and corresponding UHV vessels, vacuum pumps, and electronics)	551
Lead hutches (Optics hutch and experimental hutch)	685
Optics hutch components (Double multilayer monochromator, trigger unit, wire monitor, beam viewer, secondary slits, cooled beam stop, and corresponding vacuum vessels, pumps, and electronics)	648
Experimental hutch components (sample and detector stage, sample environment)	522
Computing infrastructure (servers, storage, workstations, software)	250
General infrastructure (supply networks, personnel safety system, air condition, control hutch)	450
Grand total	**3,506**

Table 19: BEATS overall budget estimate

16 References

Abdellatief, M., L. Rebuffi, H. Khosroabadi, M. Najdawi, T. Abu-Hanieh, M. Attal, and G. Paolucci. 2017. "The SESAME Materials Science Beamline for XRD Applications." *Powder Diffraction* 32 (S1): S6–12. https://doi.org/10.1017/S0885715617000021.

Brun, Francesco, Lorenzo Massimi, Michela Fratini, Diego Dreossi, Fulvio Billé, Agostino Accardo, Roberto Pugliese, and Alessia Cedola. 2017. "SYRMEP Tomo Project: A Graphical User Interface for Customizing CT Reconstruction Workflows." *Advanced Structural and Chemical Imaging* 3 (1). https://doi.org/10.1186/s40679-016-0036-8.

Buffiere, J. -Y., E. Maire, J. Adrien, J. -P. Masse, and E. Boller. 2010. "In Situ Experiments with X Ray Tomography: An Attractive Tool for Experimental Mechanics." *Experimental Mechanics* 50 (3): 289–305. https://doi.org/10.1007/s11340-010-9333-7.

Cecilia, A., V. Jary, M. Nikl, E. Mihokova, D. Hänschke, E. Hamann, P. -A. Douissard, et al. 2014. "Investigation of the Luminescence, Crystallographic and Spatial Resolution Properties of LSO:Tb Scintillating Layers Used for X-ray Imaging Applications." *Radiation Measurements* 62 (March): 28–34. https://doi.org/10.1016/j.radmeas.2013.12.005.

Chen, Y., L. Gélébart, C. Chateau, M. Bornert, A. King, P. Aimedieu, and C. Sauder. 2020. "3D Detection and Quantitative Characterization of Cracks in a Ceramic Matrix Composite Tube Using X-ray Computed Tomography." *Experimental Mechanics* 60 (3): 409–24. https://doi.org/10.1007/s11340-019-00557-5.

Chrysostomou, Charalambos, Mustafa Alzu'bi, Basil Aljamal, Salman Matalgah, and Gianluca Iori. 2020. "D7.1 Report on the Required Hardware and Software for the Tomography Beamline." D7.1. BEAmline for Tomography at SESAME.

Cloetens, Peter. 2007. "Phase Contrast Imaging - Coherent Beams." Presented at the School on X-ray Imaging Techniques at the ESRF, ESRF, Grenoble, France, February 5. http://www.esrf.eu/files/live/sites/www/files/events/conferences/2007/xray-imaging-school/Presentations/07_Cloetens.pdf.

Demšar, Janez, Tomaž Curk, Aleš Erjavec, Črt Gorup, Tomaž Hočevar, Mitar Milutinovič, Martin Možina, et al. 2013. "Orange: Data Mining Toolbox in Python." *Journal of Machine Learning Research* 14: 2349–53.

Douissard, P.-A., A. Cecilia, T. Martin, V. Chevalier, M. Couchaud, T. Baumbach, K. Dupré, M. Kühbacher, and A. Rack. 2010. "A Novel Epitaxially Grown LSO-Based Thin-Film Scintillator for Micro-Imaging Using Hard Synchrotron Radiation." *Journal of Synchrotron Radiation* 17 (5): 571–83. https://doi.org/10.1107/S0909049510025938.

Gianluca Iori. 2020. *Gianthk/BEATS_raytracing: BEATS Technical Design Report - Raytracing*. Zenodo. https://doi.org/10.5281/zenodo.3988604.

Guessasma, Sofiane, and Johnny Beaugrand. 2019. "Damage Kinetics at the Sub-Micrometric Scale in Bast Fibers Using Finite Element Simulation and High-Resolution X-ray Micro-Tomography." *Frontiers in Plant Science* 10: 194. https://doi.org/10.3389/fpls.2019.00194.

Kaya, Ali Can, Paul Zaslansky, Mehmet Ipekoglu, and Claudia Fleck. 2018. "Strain Hardening Reduces Energy Absorption Efficiency of Austenitic Stainless Steel Foams While Porosity Does Not." *Materials & Design* 143 (April): 297–308. https://doi.org/10.1016/j.matdes.2018.02.009.

Kumpova, Ivana, Tomáš Fíla, Petr Koudelka, Iva Rozsypalová, Zbyněk Keršner, Dan Kytyr, Michal Vopálenský, and Daniel Vavrik. 2020. "CHARACTERISATION OF THERMAL-LOADED CEMENT-BASED COMPOSITES BY COMBINED TIME-LAPSE TOMOGRAPHY AND THE FOUR-POINT BENDING TEST." *Stavební Obzor - Civil Engineering Journal* 29: 124–34. https://doi.org/10.14311/CEJ.2020.01.0011.

Le Cann, Sophie, Erika Tudisco, Mikael J. Turunen, Alessandra Patera, Rajmund Mokso, Magnus Tägil, Ola Belfrage, Stephen A. Hall, and Hanna Isaksson. 2019. "Investigating the Mechanical Characteristics of Bone-Metal Implant Interface Using in Situ Synchrotron Tomographic

Imaging." *Frontiers in Bioengineering and Biotechnology* 6. https://doi.org/10.3389/fbioe.2018.00208.

Lorentz, Kirsi, Gianluca Iori, Alexander Rack, Michael Krisch, Alberto Mittone, Andrea Lausi, Axel Kaprolat, and Frank Lehner. 2020. "D2.1 Report on Scientific Case for Micro-Tomography Beamline." D7.1. BEAmline for Tomography at SESAME.

Madi, Kamel, Katherine A. Staines, Brian K. Bay, Behzad Javaheri, Hua Geng, Andrew J. Bodey, Sarah Cartmell, Andrew A. Pitsillides, and Peter D. Lee. 2020. "In Situ Characterization of Nanoscale Strains in Loaded Whole Joints via Synchrotron X-ray Tomography." *Nature Biomedical Engineering* 4 (3): 343–54. https://doi.org/10.1038/s41551-019-0477-1.

Martelli, Saulo, and Egon Perilli. 2018. "Time-Elapsed Synchrotron-Light Microstructural Imaging of Femoral Neck Fracture." *Journal of the Mechanical Behavior of Biomedical Materials* 84: 265–72. https://doi.org/10.1016/j.jmbbm.2018.05.016.

Mirone, Alessandro, Emmanuel Brun, Emmanuelle Gouillart, Paul Tafforeau, and Jerome Kieffer. 2014. "The PyHST2 Hybrid Distributed Code for High Speed Tomographic Reconstruction with Iterative Reconstruction and a Priori Knowledge Capabilities." *Nuclear Instruments and Methods in Physics Research Section B: Beam Interactions with Materials and Atoms*, 1st International Conference on Tomography of Materials and Structures, 324 (April): 41–48. https://doi.org/10.1016/j.nimb.2013.09.030.

Mittone, Alberto, Luca Fardin, Francesca Di Lillo, Michela Fratini, Herwig Requardt, Anthony Mauro, Roberto Arturo Homs-Regojo, et al. 2020. "Multiscale Pink-Beam MicroCT Imaging at the ESRF-ID17 Biomedical Beamline." *Journal of Synchrotron Radiation* n/a (n/a). https://doi.org/10.1107/S160057752000911X.

Mittone, Alberto, Ilja Manakov, Ludovic Broche, Christophe Jarnias, Paola Coan, and Alberto Bravin. 2017. "Characterization of a SCMOS-Based High-Resolution Imaging System." *Journal of Synchrotron Radiation* 24 (6): 1226–36. https://doi.org/10.1107/S160057751701222X.

Morawe, Ch. 2020. "SESAME BEATS Tomography Beamline DMM Design."

Morawe, Christian. 2019. "Multilayer Based X-ray Optics at the ESRF." *AIP Conference Proceedings* 2054 (1): 060002. https://doi.org/10.1063/1.5084633.

"Nabu 2020.1.1 — Nabu 2020.1.1 Documentation." n.d. Accessed August 27, 2020. https://tomotools.gitlab-pages.esrf.fr/nabu/.

Ofer, Lior, Mason N. Dean, Paul Zaslansky, Shiri Kult, Yulia Shwartz, Janna Zaretsky, Shelley Griess-Fishheimer, Efrat Monsonego-Ornan, Elazar Zelzer, and Ron Shahar. 2019. "A Novel Nonosteocytic Regulatory Mechanism of Bone Modeling." *PLOS Biology* 17 (2): e3000140. https://doi.org/10.1371/journal.pbio.3000140.

"Pco.Edge 5.5 Product Data Sheet." n.d. Accessed May 11, 2020. https://www.pco.de/fileadmin/user_upload/pco-product_sheets/pco.edge_55_data_sheet.pdf.

Peatman, W. B., and K. Holldack. 1998. "Diagnostic Front End for BESSY II." *Journal of Synchrotron Radiation* 5 (3): 639–41. https://doi.org/10.1107/S0909049597017068.

Peña Fernández, Marta, Enrico Dall'Ara, Alexander P. Kao, Andrew J. Bodey, Aikaterina Karali, Gordon W. Blunn, Asa H. Barber, and Gianluca Tozzi. 2018. "Preservation of Bone Tissue Integrity with Temperature Control for In Situ SR-MicroCT Experiments." *Materials* 11 (11): 2155. https://doi.org/10.3390/ma11112155.

Pogany, A., D. Gao, and S. W. Wilkins. 1997. "Contrast and Resolution in Imaging with a Microfocus X-ray Source." *Review of Scientific Instruments* 68 (7): 2774–82. https://doi.org/10.1063/1.1148194.

"PyEpics Overview — Epics Channel Access for Python." n.d. Accessed July 1, 2020. https://cars9.uchicago.edu/software/python/pyepics3/overview.html.

Rack, A., T. Weitkamp, S. Bauer Trabelsi, P. Modregger, A. Cecilia, T. dos Santos Rolo, T. Rack, et al. 2009. "The Micro-Imaging Station of the TopoTomo Beamline at the ANKA Synchrotron Light

Source." *Nuclear Instruments and Methods in Physics Research Section B: Beam Interactions with Materials and Atoms* 267 (11): 1978–88. https://doi.org/10.1016/j.nimb.2009.04.002.

Rack, A., T. Weitkamp, M. Riotte, D. Grigoriev, T. Rack, L. Helfen, T. Baumbach, et al. 2010. "Comparative Study of Multilayers Used in Monochromators for Synchrotron-Based Coherent Hard X-ray Imaging." *Journal of Synchrotron Radiation* 17 (4): 496–510. https://doi.org/10.1107/S0909049510011623.

Rack, A., T. Weitkamp, I. Zanette, Ch. Morawe, A. Vivo Rommeveaux, P. Tafforeau, P. Cloetens, et al. 2011. "Coherence Preservation and Beam Flatness of a Single-Bounce Multilayer Monochromator (Beamline ID19—ESRF)." *Nuclear Instruments and Methods in Physics Research Section A: Accelerators, Spectrometers, Detectors and Associated Equipment*, National Synchrotron Radiation Instrumentation conference in 2010, 649 (1): 123–27. https://doi.org/10.1016/j.nima.2010.11.069.

Rack, A., S. Zabler, B. R. Müller, H. Riesemeier, G. Weidemann, A. Lange, J. Goebbels, M. Hentschel, and W. Görner. 2008. "High Resolution Synchrotron-Based Radiography and Tomography Using Hard X-rays at the BAMline (BESSY II)." *Nuclear Instruments and Methods in Physics Research Section A: Accelerators, Spectrometers, Detectors and Associated Equipment* 586 (2): 327–44. https://doi.org/10.1016/j.nima.2007.11.020.

Rack, Alexander, Johannes Stroebel, Tatjana Rack, Yves Dabin, Christine Knabe, Michael Stiller, Paola Coan, and Pierre Bleuet. 2020. "TomoPress—In Situ Synchrotron-Based Microtomography under Axial Load." *Instruments* 4 (2): 11. https://doi.org/10.3390/instruments4020011.

Rebuffi, L., and M. Sánchez del Río. 2016. "ShadowOui: A New Visual Environment for X-ray Optics and Synchrotron Beamline Simulations." *Journal of Synchrotron Radiation* 23 (6): 1357–67. https://doi.org/10.1107/S1600577516013837.

Rebuffi, Luca, and Manuel Sanchez del Rio. 2017. "OASYS (OrAnge SYnchrotron Suite): An Open-Source Graphical Environment for x-ray Virtual Experiments." In *Advances in Computational Methods for X-ray Optics IV*, 10388:103880S. International Society for Optics and Photonics. https://doi.org/10.1117/12.2274263.

Renier, M, P Bernard, W Van de Vijver, K Smets, and P Tafforeau. 2013. "A Large Size Sample Stage for High Resolution 2-D and 3-D X-ray Imaging." *Journal of Physics: Conference Series* 425 (21): 212008. https://doi.org/10.1088/1742-6596/425/21/212008.

Sanchez del Rio, M., and O. Chubar. 2014. "Advances in Computational Methods for X-ray Optics III." BNL-107140-2014-CP. Brookhaven National Lab. (BNL), Upton, NY (United States). https://www.osti.gov/biblio/1165955.

Stampanoni, Marco, Gunther Borchert, Peter Wyss, Rafael Abela, Bruce Patterson, Steven Hunt, Detlef Vermeulen, and Peter Rüegsegger. 2002. "High Resolution X-ray Detector for Synchrotron-Based Microtomography." *Nuclear Instruments and Methods in Physics Research Section A: Accelerators, Spectrometers, Detectors and Associated Equipment* 491 (1): 291–301. https://doi.org/10.1016/S0168-9002(02)01167-1.

Tanaka, Takashi, and Hideo Kitamura. 2001. "SPECTRA: A Synchrotron Radiation Calculation Code." *Journal of Synchrotron Radiation* 8 (6): 1221–28. https://doi.org/10.1107/S090904950101425X.

"The ZeroMQ Project." n.d. GitHub. Accessed June 27, 2020. https://github.com/zeromq.

"TOMWER — Tomwer 0.5 Documentation." n.d. Accessed August 27, 2020. http://www.edna-site.org/pub/doc/tomwer/latest/.

Tsuda, A., N. Filipovic, D. Haberthür, R. Dickie, Y. Matsui, M. Stampanoni, and J. C. Schittny. 2008. "Finite Element 3D Reconstruction of the Pulmonary Acinus Imaged by Synchrotron X-ray Tomography." *Journal of Applied Physiology* 105 (3): 964–76. https://doi.org/10.1152/japplphysiol.90546.2008.

Varga, Peter, Bernhard Hesse, Max Langer, Susanne Schrof, Nils Männicke, Heikki Suhonen, Alexandra Pacureanu, Dieter Pahr, Françoise Peyrin, and Kay Raum. 2014. "Synchrotron X-ray Phase Nano-Tomography-Based Analysis of the Lacunar–Canalicular Network Morphology and Its

Relation to the Strains Experienced by Osteocytes in Situ as Predicted by Case-Specific Finite Element Analysis." *Biomechanics and Modeling in Mechanobiology*, July. https://doi.org/10.1007/s10237-014-0601-9.

Wan, Xiong, Kai Zhu, Yanjin Xu, Baoshuai Han, and Tao Jing. 2019. "Early Compressive Deformation of Closed-Cell Aluminum Foam Based on a Three-Dimensional Realistic Structure." *Materials (Basel, Switzerland)* 12 (11). https://doi.org/10.3390/ma12111792.

Weitkamp, T., D. Haas, D. Wegrzynek, and A. Rack. 2011. "ANKAphase: Software for Single-Distance Phase Retrieval from Inline X-ray Phase-Contrast Radiographs." *Journal of Synchrotron Radiation* 18 (4): 617–29. https://doi.org/10.1107/S0909049511002895.

Willmot, Philip. 2019. *An Introduction to Synchrotron Radiation: Techniques and Applications*. John Wiley & Sons.

Table of figures

17 APPENDIX: Location of equipment and distances

07/06/2020 17:05

	COMPONENT		LENGTH	FLANGE TYPE	INPUT FLANGE	ION PUMP	COMMENTS
			mm	conflat	mm	l/s	
				Fixed Rotat.	4246		distance between source and exit flange
	Bellow DN63 edge welded		150.0	F 63 R	4246		
	Tube DN63		150.0	F 63 R	4396		
	Pneumatic valve		75	F 63 F	4546		
	Pumping Unit		**257**	**F 63 R**	**4621**		
		4 way cross	257				
		ion pump 75 single ended				75 l/s	Agilent Vaclon
		CF 100 flange blank					
	Tube DN63		615	F 63 R	4878		
	Pumping Unit		**613.0**	**F 63 R**	**5493**		
		bellow DN63 edge welded	150.0	F 63 R	5643		
		vacuum chamber	313.0	F 63 R			
		tee DN40 CF		40			
		Pirani gauge		40			
		Penning gauge		40			
		ion pump 300 single ended		150		300 l/s	Agilent Vaclon
		bellow DN63 edge welded	150.0	F 63 R			
	XBPM		**441**	**F 63 R**	**6106**		
		vacuum chamber					
		bellow DN63 edge welded L=160					
	Tube DN63		869	F 63 R	6547		
	Fixed Mask		**25**	**F 63 F**	**7416**		
	Photon Shutter		**543**	**F 63 R**	**7441**		
		vacuum chamber		F 63 R			
		shutter assy		150			
		ion pump 300 single ended		150		300 l/s	Agilent Vaclon
		tee DN40 CF		40			
		Pirani gauge		40			
		Penning gauge		40			
		Pressure burst disc		40			
		blank flange CF40		40			
		pneumatic valve CF63		63			
	Tube CF63		320	F 63 R	7984		
	Vacuum Fast Shutter		60	63	8305		
	Primary Slits		**635**	**F 63/40 F**	**8365**		
		bellow CF63 / CF40	150		8515		
		vacuum chamber	460				
		bellow CF100 / CF 150		100/150			
		ion pump 300 single ended		150		300 l/s	
		Zero length flange	24	40/63			
	First Window		**60**	**F 63 F**	**9000**		
	Tube CF63		542	F 63 R	9060		

	Pumping unit		**611.0**	**F 63 R**	**9602**		
		bellow DN63 edge welded L=150	149.0	F 63 R	9751		
		vacuum chamber	313.0	F 63 R			
		tee DN40 CF		40			
		Pirani gauge		40			
		Penning gauge		40			
		ion pump 300 single ended		150		300 l/s	Agilent Vaclon
		bellow DN63 edge welded	150.0	F 63 R			
	Tube CF63		542.0	F63 R	10213		
	Zero length flange		25	63/100	10755		
	Attenuator		**860**	**F 100 R**	**10780**		
		Vacuum chamber	860				
		ion pump 300 single ended		150		300 l/s	
	Zero length flange		25	100/63	11640		
	Bellow DN63 edge welded L=150		149	F 63 R	11665		
	Tube CF63		150	F 63 R	11814		
	Bremsstrahlung Shutter		**655**	**F 63 R**	**11964**		
		pneumatic valve CF63	75	63			
		vacuum chamber	430	63			
		bellow DN63 edge welded	150	63			
		ion pump 300 single ended		150		300 l/s	
		bellow DN150/100 edge welded	250	100/150			
		tee DN40 CF		40			
		Pirani gauge		40			
		Penning gauge		40			
	Tube CF 63		**1375**	**F 63 R**	**12619**		**TROUGH CONCRETE WALL**
	Trigger Unit		**439**	**63**	**13994**		
		bellow DN63 edge welded L=150	150	F 63 R			
		vacuum chamber		F 63 R			
		ion pump 230 single ended		150		230 l/s	
		tee DN40 CF		40			
		Pirani gauge		40			
		Penning gauge		40			
	Tube CF63		897	F 63 R	14433		
	bellow DN63 edge welded L=150		150	F 63 R	15330		
	Gate valve pneumatic		**75**	**63**	**15480**		
	Tube CF63		100	63	15555		
	DMM		**2250**	**F63 R**	**15655**		
		ion pump 300 single ended		150		300 l/s	
		ion pump 300 single ended		150		300 l/s	
		tee DN40 CF		40			

		Pirani gauge		40			
		Penning gauge		40			
	Tube CF63		100	63	17905		
	Gate valve pneumatic		75	63	18005		
	bellow DN63 edge welded L=150		150	F 63 R	18080		
	Tube CF63		1250	F 63 R	18230		
	Beam Viewer		260	F 63 R	19480		
	Tube CF63		220	F 63 R	19740		
	Combined Stopper		**800**	**F 63 R**	19960		
		bellow DN63 edge welded L=150	150	F 63 R	20110		
		vacuum chamber	500	63			
		bellow DN63 edge welded L=150	150	F 63 R			
		ion pump 300 single ended		150		300 l/s	
		tee DN40 CF		40			
		Pirani gauge		40			
		Penning gauge		40			
		Pressure burst disc		40			
	Long Pipe		**10965**	**F 63/100 R**	**20760**		
		zero length flange	24	63/100			
		tube CF100	10941	F 100 R			Shielded
		ion pump 300 double ended				300 l/s	
	Gate valve pneumatic		**85**	**100**	**31725**		**Entrance Experimental Hutch**
	Bellow DN100 edge welded L=200		200	F 100 R	31810		
	Secondary Slits		**388**	**F 100 R**	**32010**		
		vacuum chamber	388	100			
		bellow DN150 edge welded L=210		F 150 R			
		ion pump 300 single ended		150		300 l/s	
	Zero length flange		24	150/100	32398		
	Second Window		60	100	32422		
	Fast Shutter		102		32518		
	Alignment System				32646		
	Tomographic Sample Stage (Pos. A)				33220		
	Tomographic Sample Stage (Pos. B)				43220		
	Detector Stage				43600		
	Beamstop				45315		

18 APPENDIX: Beamline functional layout

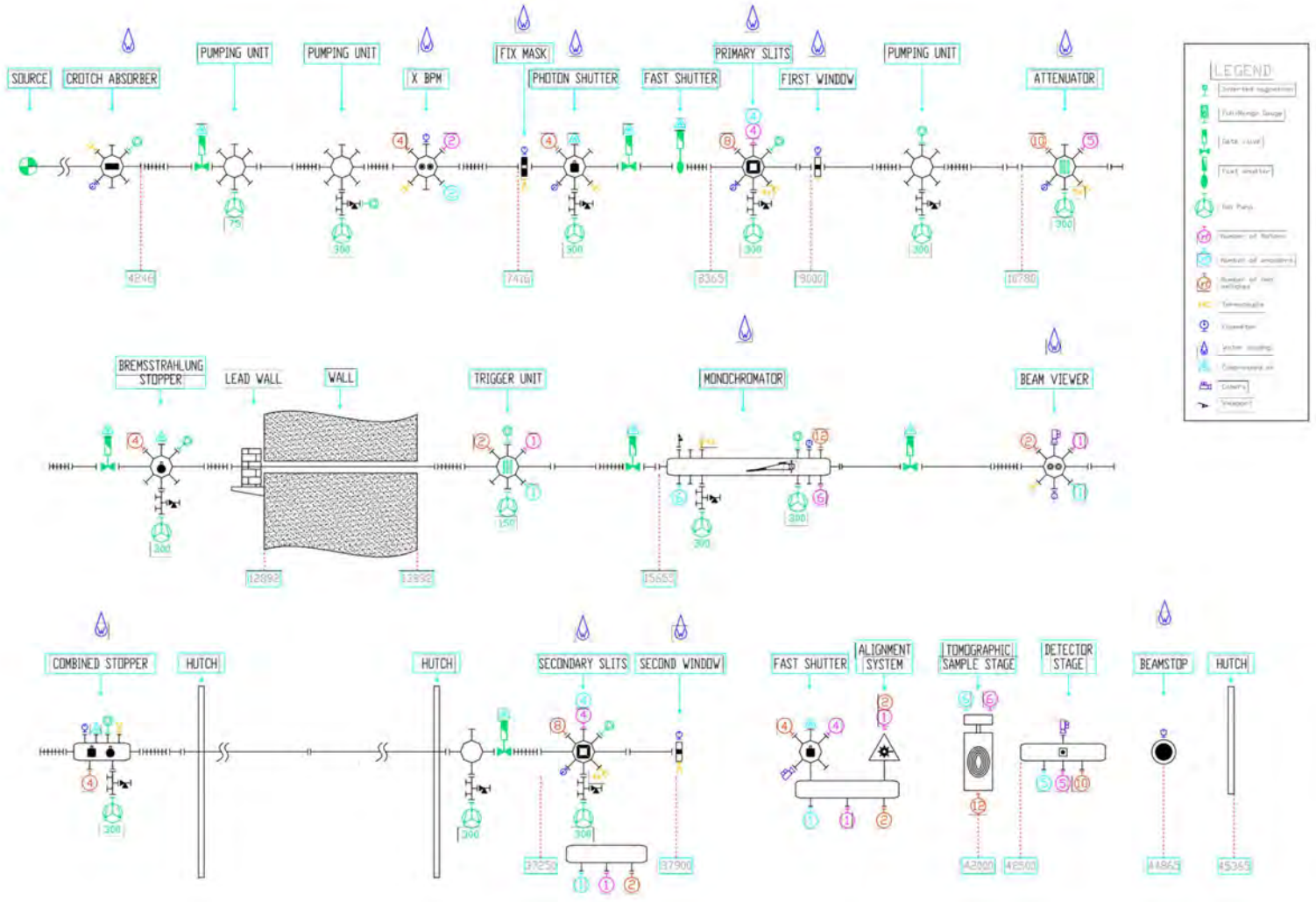

19 APPENDIX: SESAME motion standards

Motion Control System Standard

01/04/2017

Authored by: ---------- Yazeed Momani ----------

Reviewed by: ----------

Approved by: ----------

Distribution: ----------

Access: ----------SESAME.SC----------

SESAME, P.O. Box 7, Allan, 19252, Jordan,
Tel: (+962) 5 351 1348 ext. 203,
Fax: (+962) 5 351 1423

REVISION HISTORY

Revision	Date	Description	Author
0.1	01-04-2017	First Draft	Yazeed Momani
1.0	23-04-2017	Version 1.0	Yazeed Momani
1.1	14-06-2017	Added Motion Direction	Yazeed Momani
1.2	19-12-2018	Added Auxiliary Encoder	Yazeed Momani
1.3	05-02-2019	Added BiSS Encoder	Yazeed Momani
1.4	17-06-2020	Added Wires and Cables	Yazeed Momani

19.1 Introduction

Complex machines such as light sources require precise and highly repeatable motion systems, A typical beamline makes use of over fifty motors that are used to position the optical elements as well as sample and detectors. This precise motion is implemented using motion control systems.

This document defines SESAME standards for motion control systems. Technologies, vendors, and products have been selected to meet most of SESAME's motion applications needs.

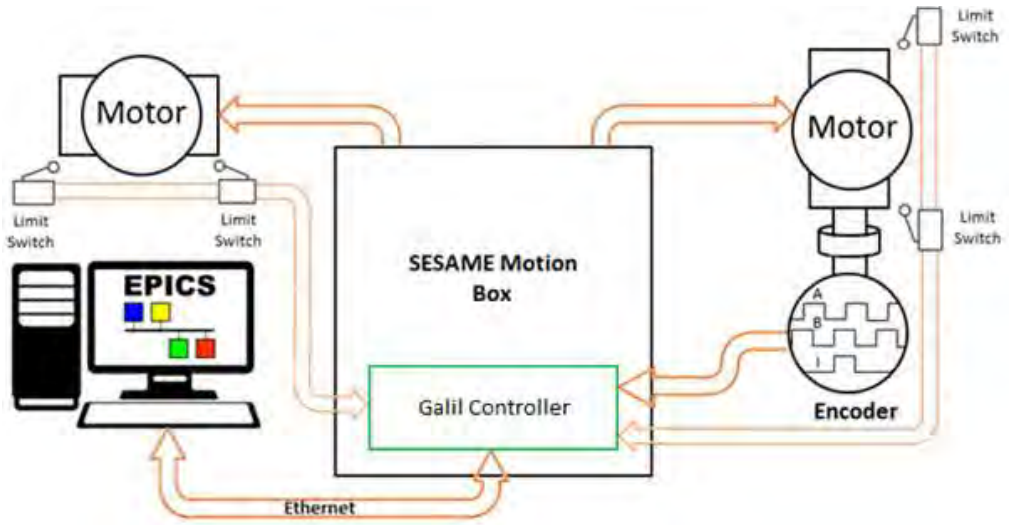

19.2 Motors

SESAME has selected stepper motors as the standard type of motors that should be used in all its motion applications.

Stepper motors were selected because of their reliability, ease of implementation, and excellent position stability.

For certain applications, DC-Servo motor may be used, but their use should be justified and must remain marginal.

19.3 Stepper Motors

SMB can drive any stepper motors with the following specifications:

Type	2-Phase Bipolar
Step Angle	1.8° and 0.9°
Configuration	Series and parallel windings
Current	0.1 to 10A (in increments of 0.01A)
Voltage	48VDC
Microstep Resolution	200 to 51200 steps/rev (in increments of 2 steps/rev)
Idle current reduction	Adjustable, up to 90% of set current.

19.4 DC Servo Motors

For certain applications, DC-Servo motor may be used, but their use should be justified and must remain marginal.

SMB can drive DC-servo motors with the following specifications:

Type	BDC and BLDC
Current	Up to 10A
Voltage	48VDC

As motors are manufactured by several companies and to limit the types of motors used and to ensure the quality and availability, the products of the following companies will be preferred :

- McLennan
- Oriental Motor
- Applied Motion
- Phytron
- Portescap
- Slo-Syn

In case of doubt selecting a motor for your application don't hesitate to contact SESAME Electronics and Instrumentation Group.

19.5 Encoders

SMB accepts two encoders (main and auxiliary) for each servo motor and only one for each stepper motor (main).

The main encoder can be an incremental, absolute SSI or absolute BiSS encoder while the auxiliary encoder can only be an incremental encoder.

SMB can supply the encoder with 5VDC or 12VDC (for pin assignment go to encoder connector).

Preferred Brands Heidenhain, Renishaw, TR-Electronic, Kübler & US Digital.

19.5.1 Incremental Encoders

SMB accepts quadrature differential TTL encoders.

The input frequency to the controller must not exceed 3,000,000 full encoder cycles/second (12,000,000 quadrature counts/sec).

Encoders can be with or without an index pulse. The minimum index pulse width is 80 ns.

19.5.2 Absolute Encoders

SMB accepts absolute encoders with SSI and BiSS Interfaces, both, Single-turn or multi-turns with a total number of 31 SSI bits.

Total number of SSI bits = multi-turn bits + single-turn bits + status bits

The SSI/BiSS absolute position encoder must meet the following specifications:

- The power supply in 5VDC or 12VDC.
- SSI clock frequency 370 kHz up to 2 MHz
- The SSI position value must be encoded in either binary or Gray code.
- The status bits can be prepended or appended to the data bits.

19.6 Limit Switches

All motorized stages should be equipped with at least two limit switches; one at the start of the travel range and one at the end of it.

SESAME Standard limit switches must be a dry contact, normally-closed switches.

Forward Limit (Pin F) and Reverse Limit (Pin G) are normally-closed to GND (Pin M) in the motor connector.

The use of non-standard limit switches such as inductive, capacitive, photoelectric, and magnetic proximity sensors should be first discussed and justified with the E&I group and it should be stated clearly in the documentation.

When it's not possible to equip a motorized stage with limit switches, or when extra switches are needed, this should also be discussed and justified with the E&I group and it should be stated clearly in the documentation.

Limit switches should be selected based on the application requirements, therefore, it is expected that the limit switches characteristics, such as temperature rating, repeatability and accuracy/ precision will meet the minimum requirements of that application.

19.7 Home Switch

Whenever it is possible, it is highly recommended to equip all motorized stages with at least one home switch at a known reference point within the travel range.

SESAME Standard Home switches must be a dry contact, normally-closed switches.

The Home (Pin H) is normally-closed to GND (Pin M) in the motor connector.

The use of non-standard home switches such as inductive, capacitive, photoelectric, and magnetic proximity sensors should be first discussed and justified with the E&I group and it should be stated clearly in the documentation.

When it's not possible to equip a motorized stage with Home switches, or when extra position-switches are needed, this should also be discussed and justified with the E&I group and it should be stated clearly in the documentation.

Home switches should be selected based on the application requirements, therefore, it is expected that the limit switches characteristics, such as temperature rating, repeatability and accuracy/ precision will meet the minimum requirements of that application.

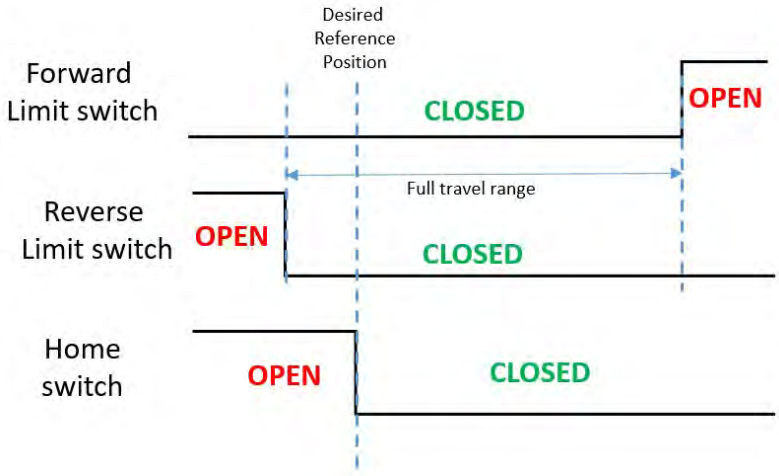

19.8 Brakes

For certain applications, a motor brake could be used, both electromagnetic and friction brakes are accepted, brake will be connected to and powered by PLC, brake voltage should not exceed 24VDC with maximum current of 500mA.

19.9 Linear Motion

Regardless of the motor rotation itself being clockwise or counterclockwise, any linear motorized stage is moving in the positive (forward) direction based on the Right-Hand rule where (cf. Figure 19);

- The Thumb points toward SESAME Roof
- The Index finger with the direction of the beam
- and Middle finger towards the Storage-ring

19.10 Rotational Motion

For rotational motion, the stage is moving in the positive (forward) direction also based on the Right-Hand rule where the Thumb points in the positive direction of the axis of rotation, and the fingers curl along the positive direction of the rotation.

Encoders should be configured/wired accordingly.

19.11 Homing

Homing should be performed in one of the following three scenarios:

1. When the motorized stage is equipped with an Encoder, the Encoder Index should be used as Home, the Encoder Index will be approached in the forward direction starting from the reverse limit switch.
2. When there is a Home switch but no Encoder, the home switch should be used as Home, the home switch will be approached in the forward direction starting from the reverse limit switch.
3. When there is neither an Encoder Index nor a home switch, the reverse limit switch will be used as home.

19.12 Connectors

19.12.1 Motor

Connector Type	**Industrial Circular Connector**
Mounting Type	Flange Receptacle
Shell-size	14
Pin-count	12
Reference	Amphenol RT001412PNH SOURIAU UT001412PH
Contacts Type	Machined Crimp Male
Reference	Amphenol MP16M23F SOURIAU RM16M23K
Pin Assignments	see table below
Mating Part	Amphenol RT061412SNH SOURIAU UT061412SH

The motor connector should be mounted on the equipment body or on a junction box attached to the equipment and as close as possible to the motor.

Pin	Stepper Motor	Brushed DC Motor	3-Phase BLDC Motor
PIN A	Phase A+	Phase +	Phase U
PIN B	Phase A-	Phase -	Phase V
PIN C	Phase B+	*Not Used*	Phase W
PIN D	Phase B-	*Not Used*	*Not Used*
PIN E	*Not Used*		
PIN F	Forward Limit Switch		
PIN G	Reverse Limit Switch		
PIN H	Home Switch		
PIN J	*Not Used*		

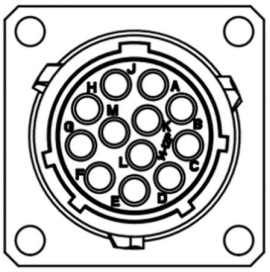

PIN K	*Not Used*
PIN L	*Not Used*
PIN M	GND
Body/Shell	Shield/PE

19.12.2 Main Encoder

Connector Type	**D-Sub Connector**
Mounting Type	Flange Receptacle
Size	DA-15
Pin-count	15
Reference	Amphenol L777-RRA-15P PHOENIX CONTACT 1688939
Contacts Type	Machined Crimp Male
Reference	PHOENIX CONTACT 1597862
Pin Assignments	see table below

Figure 92 D-Sub 15 Connector Male

The Encoder connector should be mounted on the equipment body or on a junction box attached to the equipment and as close as possible to the Encoder.

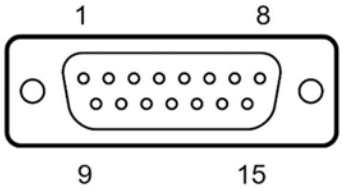

Pin	Incremental Differential Quadrature	Absolute SSI	Absolute BiSS
PIN 01	12VDC		
PIN 02	CHA-	*Not Used*	
PIN 03	CHB-	*Not Used*	
PIN 04	Index+	*Not Used*	

PIN 05	GND		
PIN 06	*Not Used*	Data+	SLO+
PIN 07	*Not Used*	Clock-	MA-
PIN 08	*Not Used*		
PIN 09	5VDC		
PIN 10	CHA+	*Not Used*	
PIN 11	CHB+	*Not Used*	
PIN 12	Index-	*Not Used*	
PIN 13	GND		
PIN 14	*Not Used*	Data-	SLO-
PIN 15	*Not Used*	Clock+	MA+
Body/Shell	Shield/Earth		

19.12.3 Auxiliary Encoder

Connector Type	**D-Sub Connector**
Mounting Type	Flange Receptacle
Size	DA-15
Pin-count	15
Reference	Amphenol L777-RRA-15P PHOENIX CONTACT 1688939
Contacts Type	Machined Crimp Male
Reference	PHOENIX CONTACT 1597862
Pin Assignments	see table below

The Encoder connector should be mounted on the equipment body or on a junction box attached to the equipment and as close as possible to the Encoder.

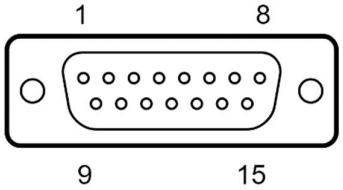

Pin	Incremental Differential Quadrature
PIN 01	12VDC
PIN 02	CHA-
PIN 03	CHB-
PIN 04	*Not Used*
PIN 05	GND
PIN 06	*Not Used*
PIN 07	*Not Used*
PIN 08	*Not Used*
PIN 09	5VDC
PIN 10	CHA+
PIN 11	CHB+
PIN 12	*Not Used*
PIN 13	GND
PIN 14	*Not Used*
PIN 15	*Not Used*
Body/Shell	Shield/Earth

19.13 Wires and Cables

- Only shielded cables may be used, with the shields connected to the ground at both ends with a distance between shield and mechanics less than 25 mm (the use of EMC clips will be strongly appreciated).
- No wires may be unshielded for a distance longer than 50 mm.

19.14 Documentation and Manuals

The manufacturer shall provide full documentation, manuals and datasheets for all the motors, encoders, limit and home switches that will be used/installed.

In addition, the manufacturer shall provide for each motorized stage a table with at least the following information:

- Type, make and model number for all the Motors, Encoders, Gearboxes, Brake Couplers, Clutches, Limit, and Home switches.
- FULL-STEP resolution (FULL-STEP/rev) and (EGU/FULL-STEP).

- Encoder counts per revolution (count/rev), and (count per motor rev) for linear Encoders.
- Encoder count resolution (EGU/count).
- Motor and gearboxes backlash in (EGU) and the recommended producers to overcome/eliminate the backlash.
- Full travel range between the upper and lower limit switches in (EGU) and (FULL-STEP) and/or (count).
- Homing method, direction, and Home value in (EGU).
- Distance between both Limit Switches and Home switch in (EGU) and (FULL-STEP) and/or (count).
- Recommended upper and lower soft limits in (EGU).
- Operational velocity and maximum velocity (EGU/s).
- Operational acceleration and deceleration (EGU/s^2).
- Limit and Home switches repeatability/hysteresis in (EGU) and (FULL-STEP) and/or (count).

Yazeed MOMANI
+962 (0) 535 113 48, Ext. 289
yazeed.momani@sesame.org.jo
Electronics & Instrumentation Engineer

Farouq OMARI
+962 (0) 535 113 48, Ext. 234
farouq.alomari@sesame.org.jo
Electronics& Instrumentation Technician

Synchrotron-light for Experimental Science & Applications in the Middle East

20 APPENDIX: Micro tomography at SOLARIS

20.1 Introduction

Two beamlines are considered for microtomography experiments at SOLARIS. Firstly, an already constructed PolyX beamline will enable microtomography experiments at relatively low X-ray energies up to 15 keV for small and/or weakly absorbing samples. Secondly, a future extension of the experimental hall of SOLARIS will enable to construct a dedicated long microtomography beamline at a 3-pole wiggler for higher X-ray energies. The locations of these two beamlines in the SOLARIS experimental hall are shown in Figure 93. This document briefly describes SOLARIS and both beamlines in the context of the BEATS project.

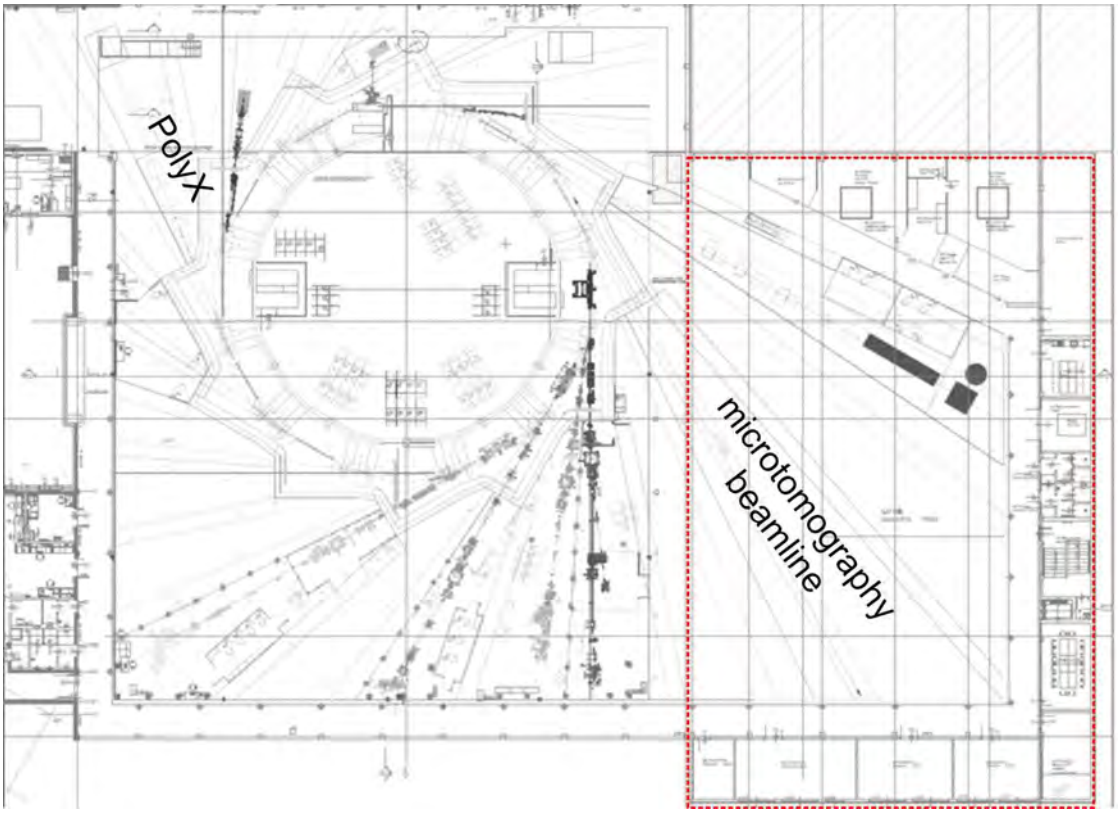

Figure 93: Beamlines at SOLARIS suited or dedicated to microtomography. The experimental hall is shown with the extension area (right hand side, marked with a red rectangle).The POLYX beamline with a length of <20 m will be a general purpose bending magnet beamline at the BL09 section. The dedicated microtomography beamline is considered to be constructed in the marked area with a source (3-pole wiggler) installed in third straight section. The maximum length of this beamline is > 45 m.

20.2 Brief description of SOLARIS

SOLARIS is a 1.5 GeV photon source dedicated to low and medium photon energy experiments composed of twelve double bend achromat (DBA) cells (main parameters of SOLARIS storage ring are presented in Table 20 and Table 21) (Wawrzyniak et al. 2017A, Wawrzyniak et al. 2017B, "MAXIV Detailed Design Report", n.d.). However, there is a strong user community in Poland and its surrounding area that would appreciate the ability to conduct their research at higher photon energies. Therefore, SOLARIS is also actively searching for the best possible technology that can be applied to increase the photon beam energy to reach the hard X-ray range. There are twelve 3.5 m long straight sections in the storage ring. Two of them are completely occupied with diagnostic

instruments, a vertical pinger, the injection septum magnet (1st straight), two 100 MHz RF cavities and two Landau cavities (12th straight). All the other straight sections are fully dedicated for insertion devices (IDs).The interest is to develop an insertion device that could fulfil the requirements regarding the best performance for both SESAME and SOLARIS machines. SOLARIS is willing to combine its efforts and share its experience with SESAME to find the best technological solutions (in terms of performance and cost effectiveness) to meet the requirements of its hard X-ray user community. Moreover, SOLARIS is also acquiring experience during the construction of the SESAME BEATS beamline taking active part in the procurement procedures and the design phase – staff from SOLARIS is taking part in the trainings organised for SESAME staff on tomography techniques, raytracing, radiology, etc.

Moreover, during the installation and commissioning of the BEATS beamline SOLARIS staff will be present at SESAME sharing with their experience in installation and alignment process of the beamline components and helping and learning at the same time during the commissioning phase

Parameter	**Designed**	**Measured**
Energy	1.5 GeV	1.45 ±0.05 GeV
Max. Current	500 mA	500 mA
Harmonic number	32	32
Natural emittance (bare lattice)	5.982 nmrad	6.5 nmrad
Coupling	1 %	0.83 %
Tune ν_x, ν_y	11.22, 3.15	11.22, 3.15
Corrected chromaticity ξ_x, ξ_y	+2,+2 ; +1, +1	+1.4, +1.6;+0.9,+0.9
Energy loss/turn	114.1 keV	103.7 ±12.3 keV
Momentum acceptance	4%	3.7± (0.3)%
Synchronous phase	168°	167.4° ± 2.7°
Synchrotron tune	0.00239	0.00228
Physical acceptance horizontal/vertical	18 /4 mmrad	15.68/3.77 mmrad
Lifetime	13h	10h

Table 20: SOLARIS storage ring parameters

	theoretical	measured
Emittance x	6 nmrad	8.05 nmrad
Emittance y	60 pmrad	65pmrad
Beta x; betay	5.697 m; 2.82m	5.84m; 2.75m
Alpha x; alpha y	0.0038; 0.0058	0.0038; 0.0058
Eta x; eta y (dispersion)	0 ; 0	-6 um; -3 um
Beam size sigmax; sigmay	183um; 13um	215.9um 13.42um
Beam div sigmax'; sigmay'	32urad;4.7urad	36.98urad; 4.9 urad

Table 21: Theoretical and measured Solaris storage ring parameters in the mid of straight section

20.3 The PolyX beamline

20.3.1 General description

Thanks to the decision of the Polish Ministry of Science and Higher Education, a new beamline (**POLYX**) will be designed and constructed at SOLARIS (2019-2022, cost 2.8M Euro) ("POLYX@SOLARIS: a synchrotron beamline for multimodal X-ray imaging, grant proposal", 2018). The POLYX beamline will be a short (18 – 21 m) bending magnet beamline intended for multimodal microimaging and microspectroscopy experiments and for general/test purposes in the X-ray range of 4 keV – 15 keV. The use of **POLY**chromatic **X-ray**s and achromatic **POLY**capillary **X-ray** optics (MacDonald 2017) will compensate for the relatively low flux of the SOLARIS in the hard X-ray energy range. The localisation of PolyX in the SOLARIS hall is shown in Figure 93.

PolyX will be operated in three different modes: (i) white/pink beam, (ii) higher flux mode using a double multilayer monochromator with bandwidth of 2—3 % and (iii) high energy mode with a Si(111) double crystal monochromator. Depending on the operation mode, PolyX, will deliver a collimated beam with a flux from 10^9 to 10^{13} photons/s/mm^2. Polycapillary optical elements with transmission from 2-20% will enable the production of focused beams with sizes from 5 µm to 50 µm. In future, a compact KB mirror system or monocapillary focuser is planned for generation of a sub-micron beam.

Main experimental techniques will be µXRF, µXAFS and µCT. A dedicated experimental area will be designed for non-standard user experiments.

The layout of PolyX and its operational modes are shown in Figure 94. Most important parameters are listed in Table 22.

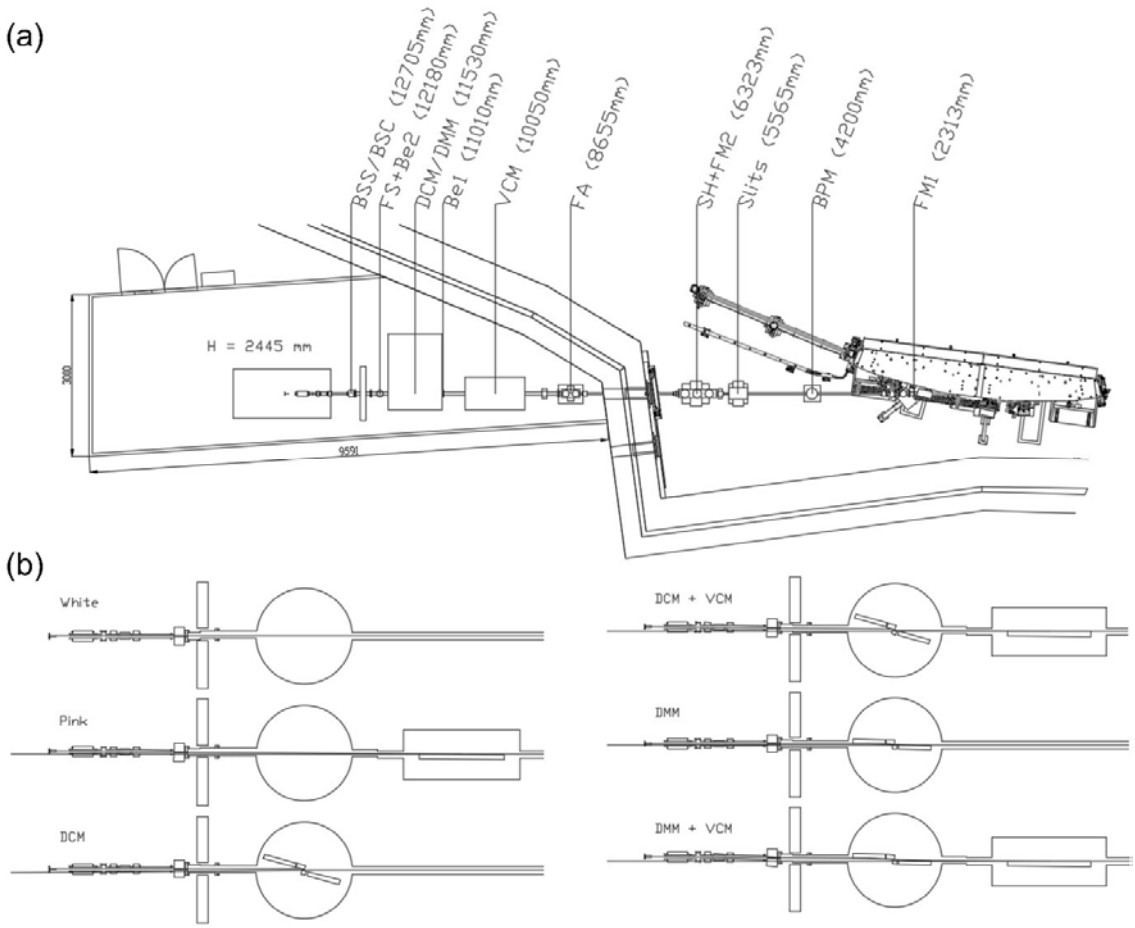

Figure 94: The PolyX beamline. (a) Layout. (b) Experimental geometries. The DMM/DCM will be a hybrid device.

Source	bending magnet			
Source size	44 µm, 30 µm			
Sample position	13 – 18 m			
Energy range	4 – 16 keV			
Flux	DCM - Si(111) - 10^9 ph/s/mm^2 (@8 keV) DMM - 10^{11} ph/s/mm^2 (@8 keV) White beam – 10^{13} ph/s/mm^2			
Energy resolution	DCM: 1.5×10^{-4} DMM: 2.5×10^{-2}			
Optics/focal spot/ Input aperture/transmission	polycapillary optics	30 µm	8×4 mm^2	30%
		12 µm	4x3 mm^2	10%
		5 µm	2x2 mm^2	2%
	Compact KB or monocapillary	<1 µm	0.5x0.5 mm^2	90%
Detectors	FAST SDD 50mm^2 x 4, hybrid pixel detector, x-ray camera, ionization chambers, photodiodes,			
Conditions	air, He, LV, cryo-stream			
Experimental techniques	µXRF (+ confocal, tomography),µXAFS, µCT			

Table 22: Parameters of the PolyX beamline

20.3.2 Micro tomography at PolyX

Micro tomography at PolyX will be restricted to rather low X-ray energies (<15-17 keV). Tomographic experiments will be possible for small or low-Z materials. This energy range is lower than energy ranges of typical micro tomographic beamlines. However, it is well suited for combination of micro tomography with x-ray fluorescence tomography, which will be also possible at PolyX.

Two variants of micro tomography geometry will be possible at PolyX. Parallel beam tomography (white beam or DMM) will enable resolution at the level of 1-2 microns and field-of-view of 2-4 mm.

At PolyX, a unique version of cone-beam tomography at deep-submicron resolution will be implemented using polycapillary optics (Sowa and Korecki, 2020). Single exposure plenoptic-like depth-resolved X-imaging will make it possible to study larger planar samples (Sowa et al. 2018, Sowa et al. 2020).

Almost thirty experimental groups from Poland end Central Europe sent a user questionnaire for the purpose of the preparation of the project for the Polish Ministry of Science and Higher Education. The main applications of POLYX will be: biosciences, cultural heritage, catalysis, earth & environmental science as well as functional materials.

The micro tomography setup at PolyX will greatly benefit from the design of the experimental instrumentation (x-ray camera, sample stages) during the BEATS project.

20.4 The micro tomography beamline

In the future, it is planned also to construct the high energy micro-tomography beamline with the strong insertion device as a source. The considered localisation of the micro tomography beamline would be 3rd straight section in SOLARIS storage ring constructed in the experimental hall extension that is now under design (Figure 93).

First calculations of the impact of the three pole wiggler which was selected for the BEATS project on the SOLARIS storage ring optics were carried out.

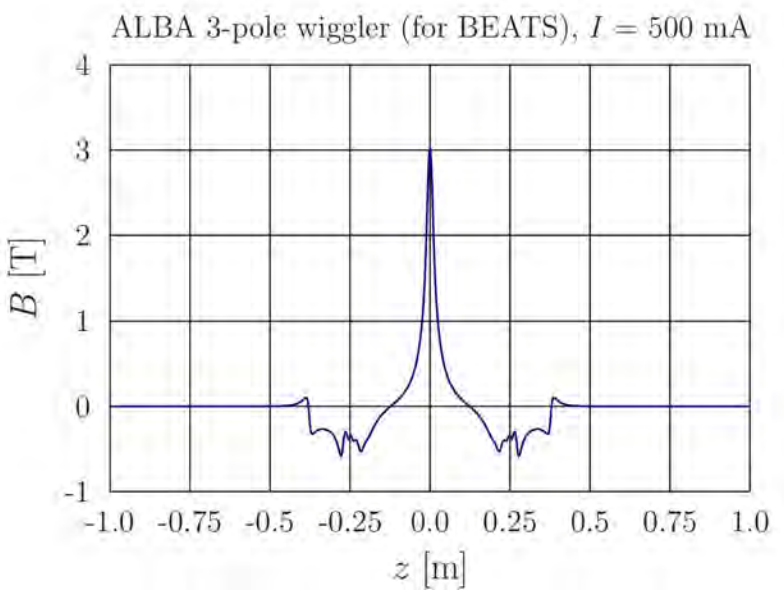

Figure 95: Magnetic field distribution along the longitudinal space from the 3PW

Strong insertion devices have a non-negligible impact on the beam optics through vertical focusing which results in a vertical tune shift according to:

$$\Delta\nu_y \approx \frac{\pi L\langle\beta_y\rangle K^2}{2\lambda_u\gamma^2} \quad (1)$$

where ν_y is the vertical tune, L the length of the undulator, K the ID strength parameter, λ_u the period length and γ *is* the relativistic energy. A strong planar ID inserted into the lattice also generates a vertical beta beat:

$$\frac{\Delta\beta_y}{\beta_y} \approx \frac{2\pi\Delta\nu_y}{\sin(2\pi\nu_y)}. \quad (2)$$

In order to correct for these effects proper optics matching has to be performed and the working point needs to be restored. For the Solaris storage ring lattice the local matching can be done either by installing two extra quadrupole doublets upstream and downstream of the ID or by locally changing the gradient of the flanking focusing quadrupoles *SQFo* and the gradient in the flanking bending magnets. The second approach can be executed by adding extra power supplies on the flanking *SQFo* as well as on the pole face strips of the flanking dipoles.

The insertion of the 3T 3PW has an impact on the vertical and horizontal plane as it is seen in Figure 96. The vertical tune is shifted from 3.15 up to 3.1625, a change of 0.0125. The horizontal tune is shifted from 11.22 down to 11.2012. It is possible to properly adjust the flanking quads and pole face strips in order to restore the nominal optics. The 3PW also has a detrimental impact on the dynamical aperture. However, proper adjustment of the harmonic sextupoles helps to increase the dynamic aperture of SOLARIS storage ring. More beam dynamics studies have to be conducted in the future to optimse the storage ring optics with a 3PW device.

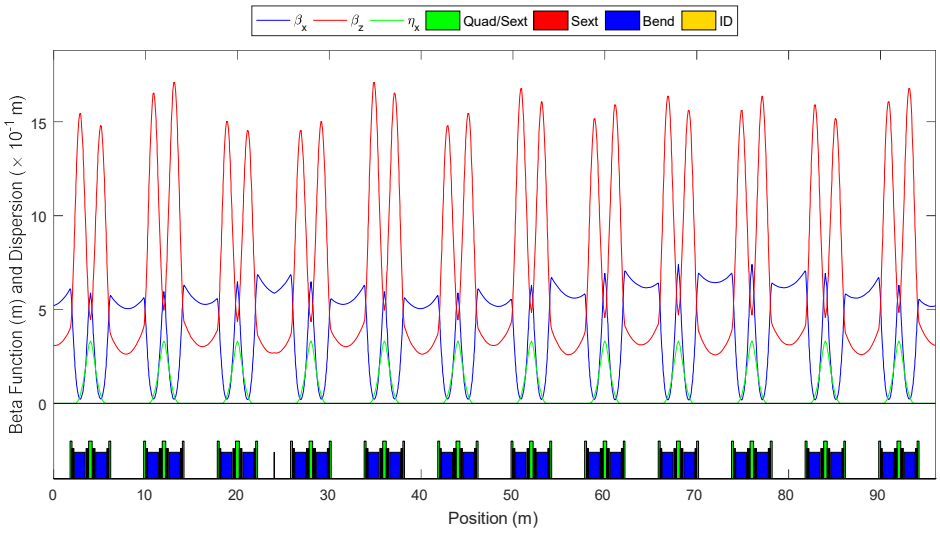

Figure 96: Betatron function distorsion after inserting the kick maps

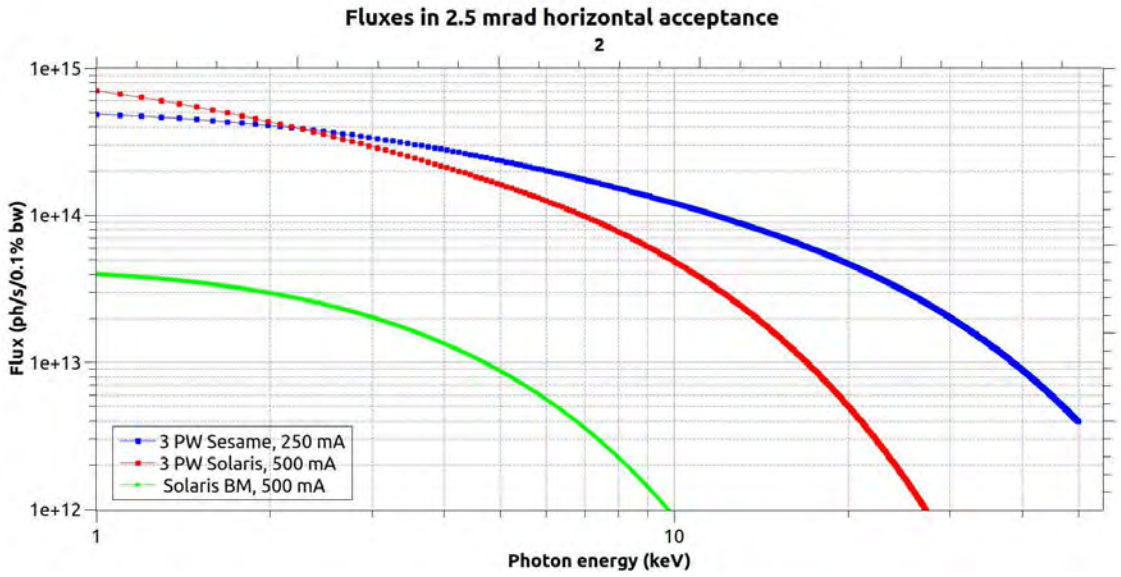

Figure 97: Photon flux calculated from the bending magnet (BM) and 3PW for SOLARIS and the SESAME storage ring

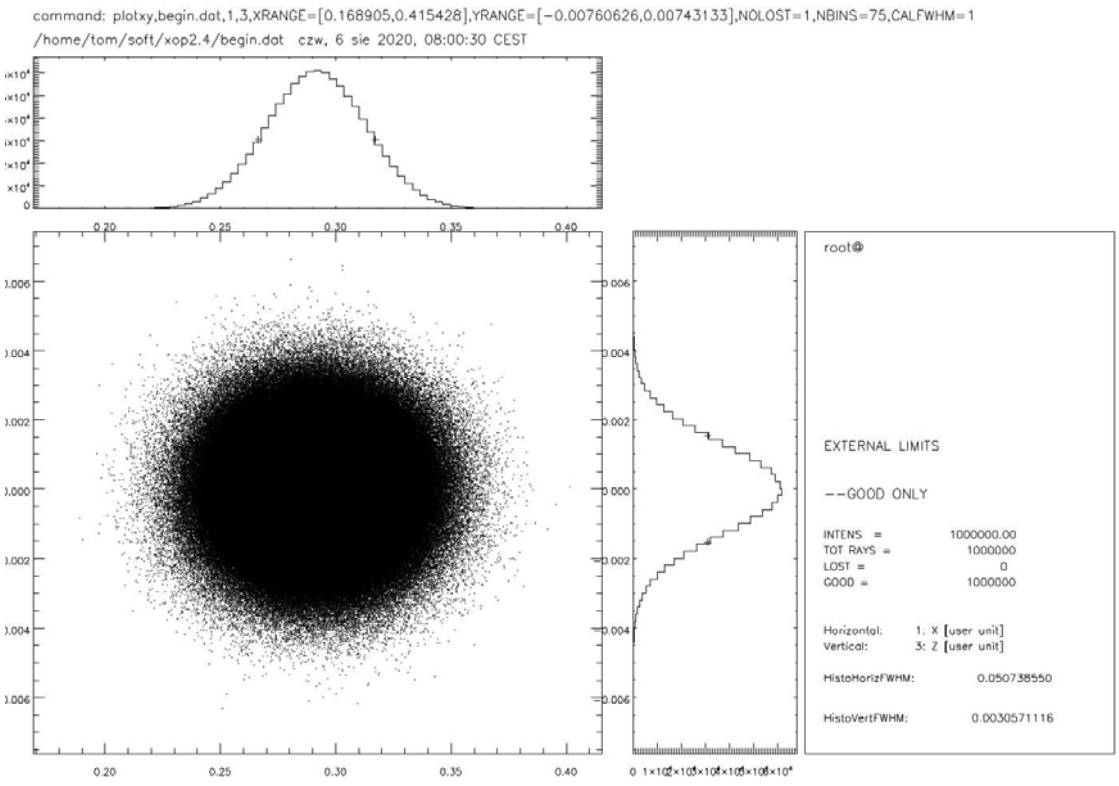

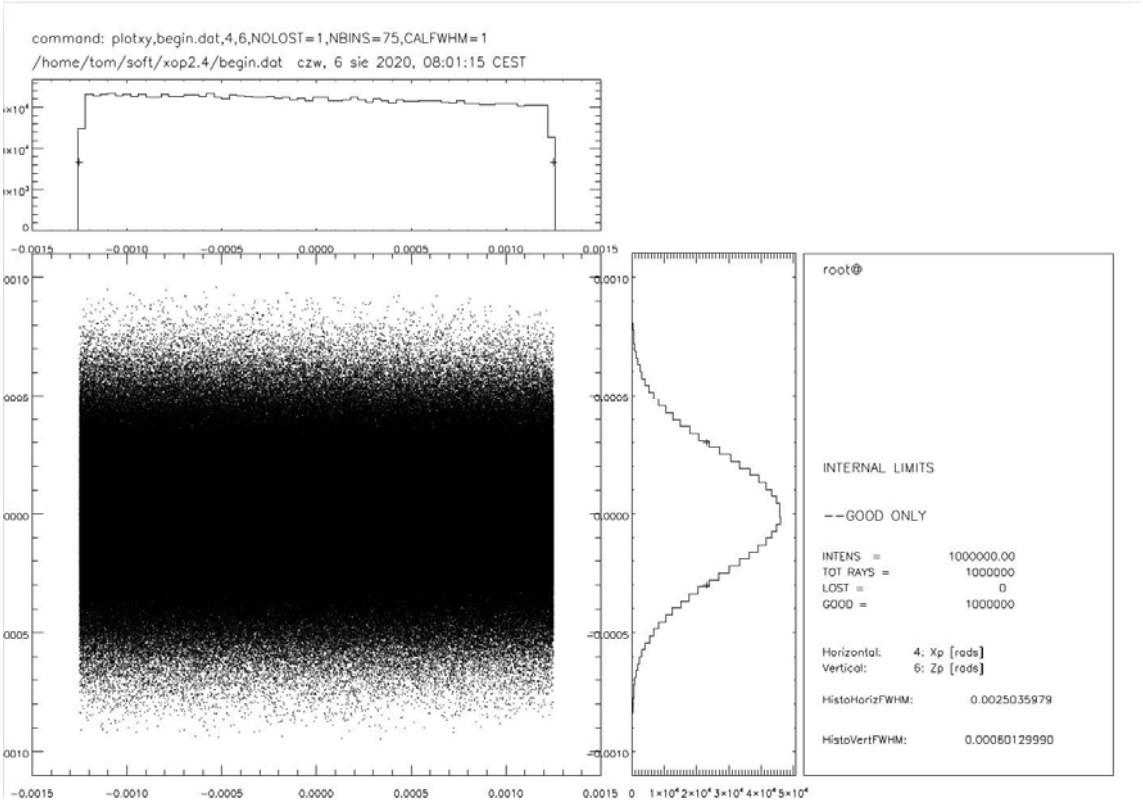

Figure 98: Beam size 507 x 30.5 µm2 (FWHM) and divergence 2.5x 0.6 mrad2 (FWHM) of the photon beam in SOLARIS

The photon flux calculated for the SOLARIS storage ring with the three pole wiggler (3PW) as a source is one order of the magnitude higher than flux produced by a SOLARIS bending magnet (BM) as seen in Figure 97. Moreover, the critical energy is shifted to 4.45 keV. The calculations were performed for an electron current of 500 mA. Figure 97 also shows the comparison between the flux from a 3PW at SOLARIS and at SESAME. The photon beam size and divergence calculated for the SOLARIS storage ring with a 3PW as a source are presented in Figure 98.

20.5 Summary

The microtomography beamline with high flux and high spatial resolution is of high interest for the SOLARIS user community. Currently, the PolyX beamline that is under construction, will give the opportunity for micro tomographic experiments within the energy range up to 15 keV for small and/or weakly absorbing samples.

In the future the tomography beamline for higher x-ray energies is planned to be constructed based on the SESAME tomography beamline design. The construction of this beamline is foreseen in the the course of the extension of the experimental hall which is now under construction and will be ready in 2022. SOLARIS' participation in the BEATS project creates the opportunity for the SOLARIS team to successful design, construct and commission the high quality microtomography beamline in the future.

20.6 References:

A.I. Wawrzyniak, A. Kisiel, A. Marendziak et al.,"Solaris Storage Ring Performance" Proceedings of IPAC2017, WEOCA01, Copenhagen Denmark (2017), 2490.

A.I. Wawrzyniak et al., "Solaris a new class of low energy and high brightness light source", Nuclear Inst. and Methods in Physics Research, B 411, (2017) 4

MAXIV Detailed Design Report, https://www.maxiv.lu.se/acceleratorsbeamlines/accelerators/accelerator-documentation/max-iv-ddr/

POLYX@SOLARIS: a synchrotron beamline for multimodal X-ray imaging, grant proposal IA/SP/0010/2019, June 2018, in polish

C.A MacDonald, Structured X-ray Optics for Laboratory-Based Materials Analysis, Annu. Rev. Mater. Res. 47, 115 (2017)

K. M. Sowa, P. Korecki, X-ray tomography with multiple ultranarrow cone beams , Optics Express 28, 23223 (2020)

K. M. Sowa, M.P. Kujda, P. Korecki, Plenoptic X-ray microscopy, Applied Physics Letters 116, 014103 (2020)

K. M. Sowa, B.R. Jany, P. Korecki, Multpoint-projection X-ray microscopy, Optica 5, 577 (2018)

21 APPENDIX: Tomography at ALBA

21.1 Introduction

Over the last decades, important progress has been achieved in several research fields by taking advantage of the development of three-dimensional (3D) characterization techniques. These techniques allowing the 3D visualization of the object morphology at the microscopic scale led to a better understanding of the microstructure in materials, animals, fossils, etc. In order to cope with an increased demand for these techniques, several imaging beamlines are currently under development at different synchrotron radiation facilities, as for example FaXToR (ALBA_CELLS) and BEATS (SESAME). FaXToR will be a versatile hard x-ray imaging beamline at ALBA-CELLS with an important focus on fast x-ray tomography and radiography. Similar to the BEATS beamline, FaXToR is foreseen to operate in both the absorption and the phase-contrast regime. These two classes of techniques allow retrieving the 3D distribution of the x-ray absorption and refraction properties of the object under investigation. Possible applications include 3D and 4D investigation of samples at the microscopic scale in the fields of material science, life science, palaeontology and cultural heritage.

FaXToR will be a short beamline (~38 m) and is foreseen to operate in the hard x-ray regime, with an energy range between 8 keV and 50 keV (in monochromatic mode), which is very similar to the one expected at the BEATS beamline, and energies up to 80 keV in case of filtered white beam. The availability of the white beam is of particular importance for FaXToR for time resolved studies. As x-ray source, FaXToR will make use of a 5-pole wiggler; contrary to BEATS, where a wavelength shifter is foreseen. A double multilayer monochromator will be used to select a monochromatic beam both for FaXToR and BEATS. This kind of monochromator is used whenever a high flux and monochromatic beam are required. The expected energy bandwidth will vary between 2% and 4%. For both BEATS and FaXToR this monochromator will represent the main optical element of the beamline.

FAXTOR will have one single experimental station dedicated to 4D Computed Tomography (CT) and radiography. A high performance tomography setup together with several detection systems, the latter composed of scintillator screen, visible light optics and high speed cameras, will be part of the equipment available. Similar instrumentation is expected to be available at BEATS.

Because of the increased technical improvements, high performing tomographic beamlines need to deal with a high data throughput. High speed network connections, fast storage with large capacity and computational power are required to optimize the performanc of the beamline. Together with an appropriate IT infrastructure, highly optimized software must be available in order to reconstruct and process the data produced. Different commercial and open-source solutions are foreseen to be accessible for this purpose to the users and to the staff of the beamline.

21.2 Insertion Device source design

ALBA Insertion Devices and Front Ends Section staff from the Accelerators Division has wide experience in the design, construction, characterisation and operation of Insertion Devices and Front Ends. They have been responsible of the design of both BEATS and FaXToR Insertion Devices in accordance with the requirements established by both beamline scientists and adapted to both the ALBA and SESAME storage ring.

The final design for the FaXToR Insertion Device (ID) consists of a Five-pole-Wiggler, MPW50, the total emitted power (400 mA) is 3.64 kW. The main design parameters considered for the model are:

- Minimum gap: 5 mm
- Maximum field: ~2.5 T
- Magnetic length: < 1 m.
- Spectral range with flux > 10^{11}[ph/s.mm^2.mrad^2.0.1%BW] : 20-50 keV

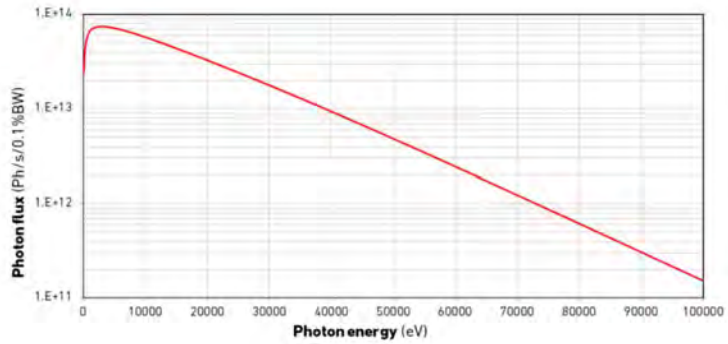

Figure 99: MPW50 Spectrum at minimum gap, aperture of 4 mrad H x 1 mrad V and 100 mA in SR

In the case of BEATS, three different ID proposals were submitted for consideration. The final design consists of a Three-pole-wiggler (hereafter 3PW). The main design constraints considered for the model are:

- Minimum gap: 11 mm
- Maximum field: ~3 T
- Magnetic length: < 1 m.
- Spectral range achieved with flux > 10^{11}[ph/s.mm^2.mrad^2.0.1%BW] : 20-50 keV

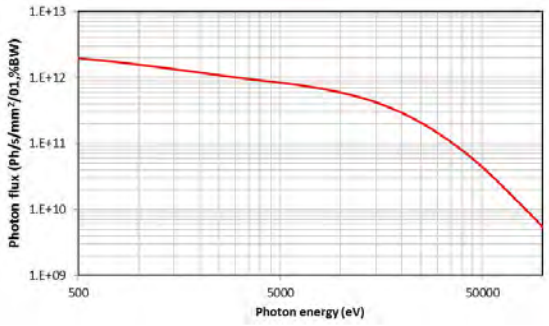

Figure 100 Emission spectrum of 3-pole-wiggler at minimum gap through an aperture of 4 mrad H x 1 mrad V.

21.3 Front End design

ALBA Insertion Devices Section staff has also a wide experience in the design, installation, operation and maintenance of Front Ends (FEs). They have been the responsible for the design of the FaXToR Front End, and they have lead the design of BEATS Front End in collaboration with the other project partners (ELETTRA, ESRF, SESAME). In both cases the FE design has been adapted to the characteristics of the ID source, the particularities of the accelerator tunnel layout and environment, and the specific requirements from the beamline scientists. A comparison of some of the relevant parameters for both FEs is shown in the following table:

	Total power @400mA [kW]	Peak power density @ 400 mA [kW/mrad^2]	Horizontal user aperture [mrad]	Vertical user aperture [mrad]
FaXToR	3.64	5.31	1.0	0.4
BEATS	0.99	0.25	1.0	0.36

In the case of the FaXToR FE, we have tailored the ALBA baseline design for FEs to the power load and angular acceptance characteristics of the beamline. As an innovation with respect to previous FEs at ALBA, we foresee the installation of a second X-ray Beam Position Monitor (XBPM) in order to obtain information regarding the angle of the photon beam. The proposed layout for FaXToR FE is shown in Figure 101

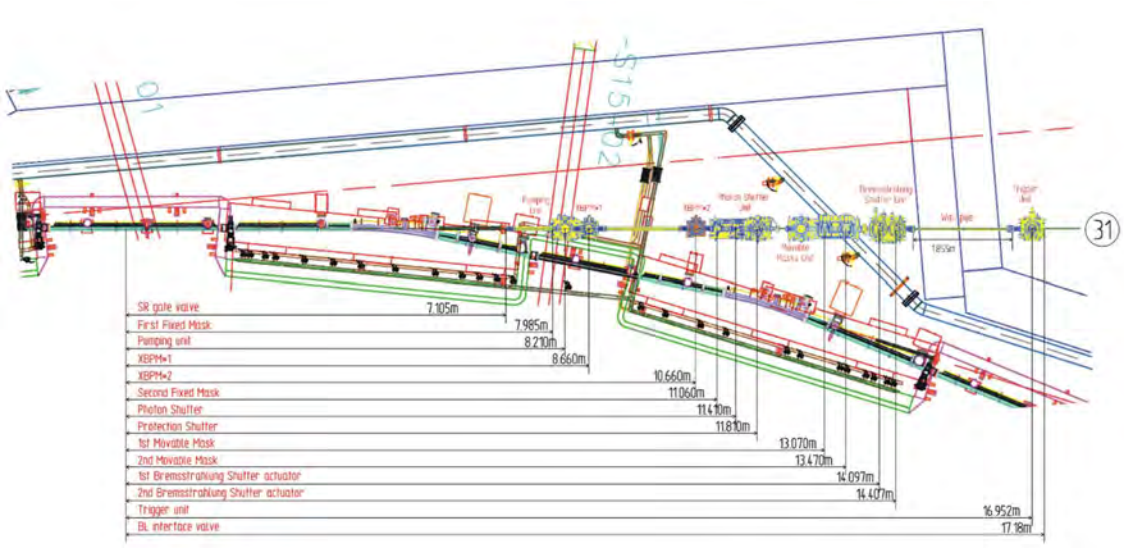

Figure 101 Proposed layout for FaXToR FE at ALBA.

In the case of the BEATS FE we have also taken the ALBA baseline design as a starting point, but there are some relevant deviations from it due to either (i) different standards at SESAME, (ii) particular requirements from the beamline or (iii) the input from other partners from BEATS collaboration. The main differences with respect to the FaXToR FE are:

- Due to ray tracing considerations, a Fixed Mask in front of the XBPM is not required.
- In order to save costs, only one XBPM has been foreseen. On top of this, and taking into consideration that the photon beam distribution from the 3-pole wiggler is very wide along the horizontal direction, we have proposed using a Staggered Pair Monitor (SPM) configuration for the XBPM blades (this configuration is only sensitive to the vertical position of the photon beam).
- The Fixed Mask in front of the Photon Shutter will be manufactured according to a design provided by Elettra.
- Due to the relatively small power delivered by the ID at BEATS, we have proposed to adopt for the Photon Shutter the design which is used at ALBA for those FEs with a bending magnet as a source.
- As for the Primary slits (Movable Masks in ALBA terminology), it is foreseen to reuse the slits from the imaging beamline ID19 at the ESRF.

- A CVD window to separate the vacuum of the storage ring from that on the beamline is required.
- A second pumping unit similar to the one installed at the beginning of the Front End has been required downstream from the Primary Slits in order to provide extra pumping capacity.
- An attenuator unit to tailor the photon beam energy spectrum and heat load will be installed inside the tunnel, following a design provided by the ESRF.
- The Bremsstrahlung Stopper will consist of a single tungsten block, as it is the case for the other FEs at SESAME (at ALBA FEs a double Bremsstrahlung Stopper is used).

The resulting layout for BEATS FE is shown in Figure 102. Elements highlighted in yellow have been specified following designs used at ALBA; elements highlighted in green will make use of designs provided by the ESRF and ELETTRA; elements highlighted in magenta (Primary Slits) will be reused from other facilities; finally, unmarked elements correspond to either commercial components or components which are outside of the scope of the Front End design.

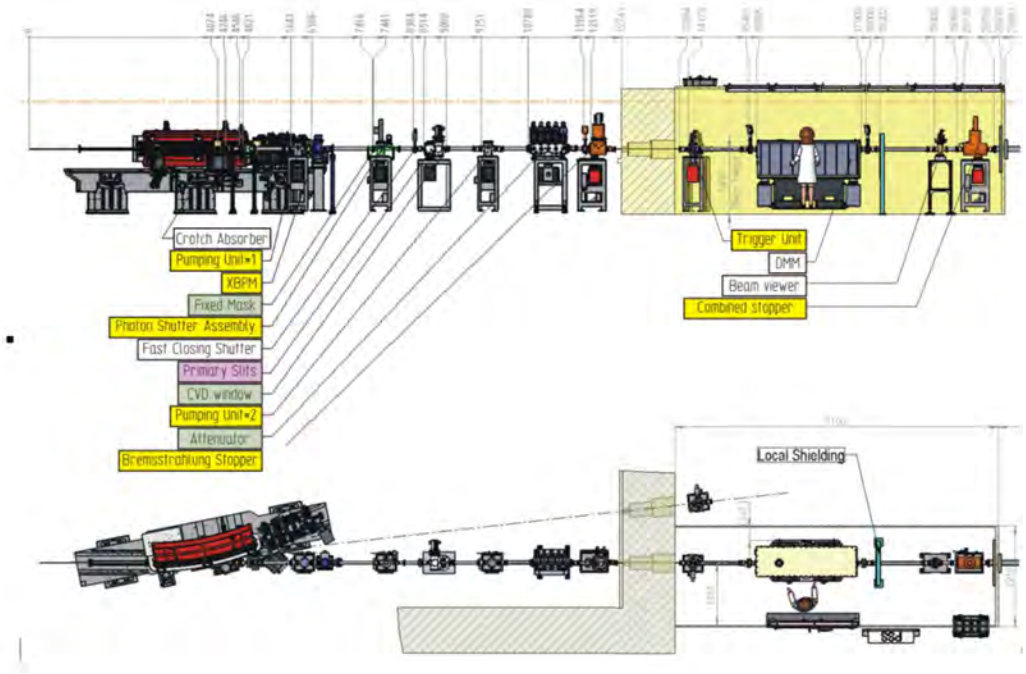

Figure 102 Proposed layout for BEATS FE at SESAME.

21.4 Radiation Protection enclosures design

The ALBA Radiation Protection Service has experience in the design, construction and commissioning of radiation shielding and their interlocking systems. They are responsible of the establishment of the shielding requirements for both BEATS and FaXToR in accordance with SESAME and ALBA exposure limits and geometrical constrains of their Experimental Halls.

The main factors affecting the shielding requirements are the following:

- Storage Ring (SR) electron beam energy and current,
- X-ray source type (Dipole or Insertion Device)
- Characteristics of the FE and optics
- Vacuum levels and composition inside the chambers
- Dose limits to be respected
- BL operation modes (White beam or not)

A summary of these key parameters for BEATS and FaXToR are given in Table 23.

Parameter	BEATS	FaXToR
SR electron beam energy	2.5 GeV	3 GeV
SR max. current	400 mA	400 mA
X-ray source type	Insertion Device	Insertion Device
Optics	DMM at OH Slits at EH Sample on air	Slits and DMM at OH Slits at EH Sample on air
Vacuum level	5.0×10^{-9} mbar	5.0×10^{-9} mbar
Limit dose rate	0.5 µSv/h	0.5 µSv/h
BL operation mode	White beam at OH and EH Monochromatic beam 8keV-50keV	White beam at OH and EH Monochromatic beam 8keV-50keV

Table 23: Summary of key parameters for the establishment of BEATS and FaXToR shielding requirements

The radiation levels around the enclosures of Insertion Device beamlines are dominated by the gas Bremsstrahlung contribution coming from the interaction of the SR electrons with the residual gas present in the straight section vacuum chamber where the ID is inserted. This is true for both BEATS and FaXToR, thus the initial shielding requirements have been the same.

Monte Carlo simulations with FLUKA code are then run to reproduce the radiation levels produced around the hutches under different conditions representing the different operation modes and significant accidental situations. The geometry entered into the input files reflects the layout restrictions and include all significant optical elements. The initial shielding estimations are then modified as necessary until the dose rate limit is observed outside the enclosures for all scenarios and geometric possible layouts. The Monte Carlo simulations also allow designing screens, beam stops and collimators, whose position is optimised through a graphical analysis of the beam path all along the optics. This analysis is known as the Limiting Raytracing, and the drawings produced for FaXToR and BEATS are shown in Figure 103 and Figure 86.

Regarding operation modes both beamlines aim at producing synchrotron beams for tomography techniques in two main operation modes:

1. White beam or mirrorless mode: under which the full beam emitted by the ID source can reach the sample in the Experimental Hutch,
2. Monochromatic beam or mirrored mode: during which a Double Multilayer Monochromator (DMM), placed inside the Optics Hutch, allows filtering the ID source beam so that the sample is analysed under a monochromatic beam of selectable energy in the Experimental Hutch.

Consequently the list of simulation scenarios for both beamlines is the same:

1. White beam operation mode scenarios – mirrorless configuration.
2. Monochromatic beam operation mode scenarios – mirrored configuration with MM1 and MM2 of the DMM inserted at the two extremal positions, representing the minimum and maximum monochromatic selectable energies. In the case of FaXToR both MM1 and MM2 are placed at a fixed distance and the energy is selected by varying the offset among them and the incidence angle. For BEATS, the selection of the energy is done by changing the distance between MM1 and MM2 and the incidence angle, keeping the offset fixed.
3. Bad vacuum conditions inside the transfer line- accidental situation.

A final set of shielding requirements are then established for both beamlines by using the same calculation methodology and adapted to the geometrical particularities of each of them.

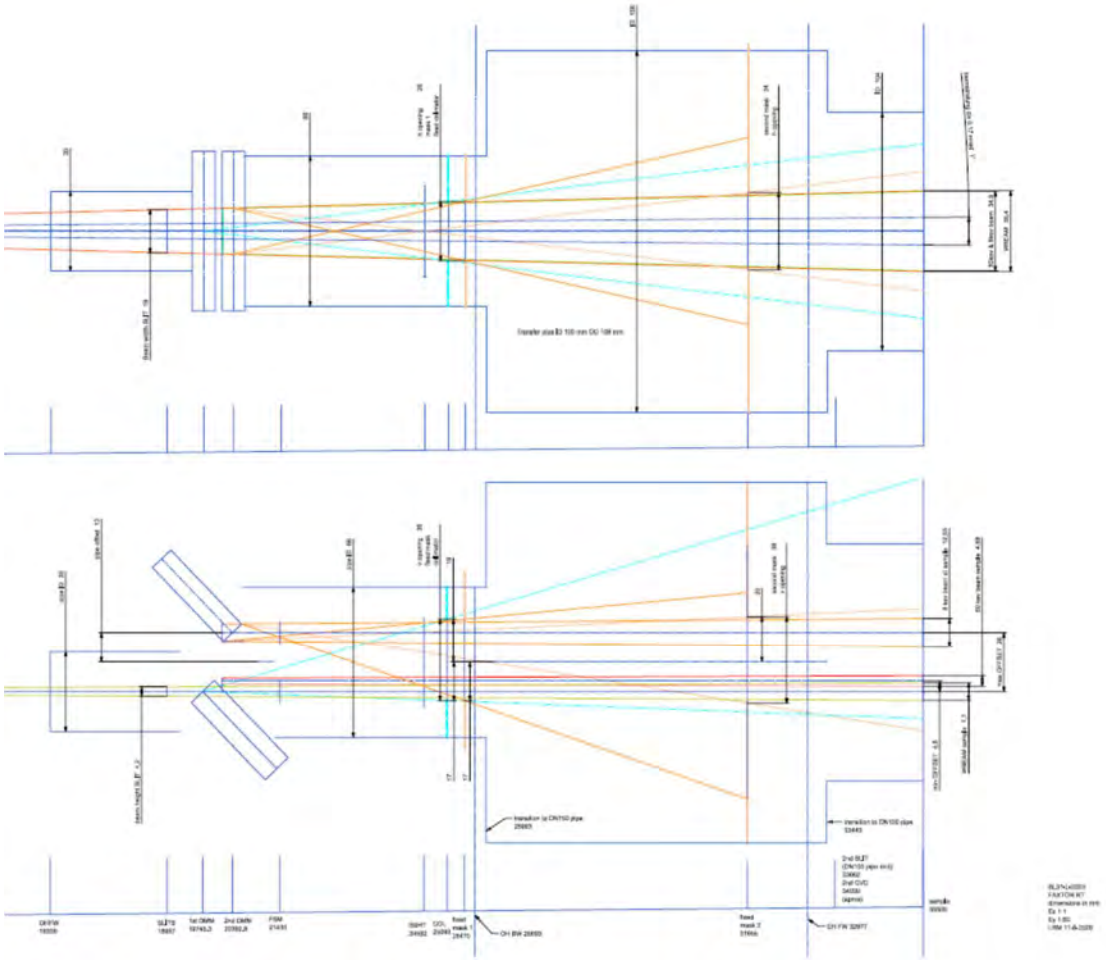

Figure 103 FaXToR limiting raytracing drawing including the internal aperture of the collimator to be used to ensure that no scattered ray hits the TL vacuum chamber

21.5 Training and "know how" transfer for BEATS

SESAME's relation with ALBA has been developing for some years now, well before the start of the BEATS project, and many SESAME staff members spent time at ALBA, almost in all divisions and sections. In continuation of the brother-hood established in the past years, fruitful discussions have been carried out between ALBA and the BEATS team concerning aspects related to the beam coherence properties and on several technical aspects linked to the end station. Mutual efforts have been carried out in order to focus on the possible fields of application of BEATS, in order to tune certain technical specifications for the end station. New topics, for instance regarding scientific software will for sure be a matter of future discussions.

This collaboration climate has extended into the more technical issues like the ID and FE designs. In particular, the Front End responsible at ALBA has been in contact with the Diagnostics responsible at SESAME (Omar Kailani), answering his questions about the usage of XBPMs at ALBA and sharing technical notes and documentation developed at ALBA. ALBA has also provided information regarding the expected cost of XBPMs and associated electronics.

A huge effort is also being done to train SESAMEs staff and transfer ALBA's know-how regarding Radiation Protection matters. In fact, SESAME's new safety engineer Dr. Zahran, who was hired after the BEATS project begun, is under training right now by the ALBA Radiation Protection Service. A 40 days stage at the ALBA facility was planned and started after the 2020 General meeting. The training topic was: "Radiation Protection procedures and commissioning at ALBA". The stage had to be interrupted due to the COVID-19 Spanish lockdown, which started on the 12th of March, but the training has continued online and Dr. Zahran is participating actively in the shielding calculations ongoing for BEATS and will continue during the whole duration of the project as we move into the construction and commissioning phases, during which ALBA will keep an active role.

The scientific and technical interactions between ALBA and BEATS are expected to last during all the duration of the project and beyond.

22 SESAME beamline vacuum standards

22.1 General

This document defines the technical terms of delivery and acceptance as well as general specifications for design, construction, and handling of UHV Components for the SESAME beamlines

22.2 Standard components:

Items	Company
Valves	VAT
Ion Pumps	GAMMA VACUUM
Ion pumps controllers	Agilent
NEG Pumps	SAES
Gauges And gauges controllers	Pfeiffer
Standard vacuum parts (otherwise specified)	VACOM
Edge welded bellows	COMVAT

22.3 Preliminary remarks

The **U**ltra **H**igh **V**acuum (UHV) section of a beam line (i.e., the front end) will be connected to the vacuum system of the SESAME storage ring. The end pressure to be achieved is to be less than 1 x 10^{-9} mbar. The helium leak rate must be below 1 x 10^{-10} mbar.l/s.

In the **H**igh **V**acuum (HV) section, the end pressure shall be less than 1.10^{-7} mbar. Leak rate shall be $<1.10^{-7}$ mbar.l/s.

The required all-metal UHV components must be bakeable up to the suitable temperature depending on the application and the materials used.

In this annex, the requirements for commercially and non-commercially available vacuum components are outlined.

22.4 Design

The materials used and design and fabrication of all parts must be in compliance with UHV requirements.

Narrow gaps and clearances (unvented holes etc.) within vacuum components must be avoided in order to exclude virtual leaks.

Steel and stainless steel ball bearings must be avoided in vacuum.

Welding between cooling fluid enclosures and parts exposed to vacuum must be avoided.

The surface properties of the sheet metal used in vacuum sections must be in accordance with DIN EN 10088-2, Table 6, "2B". Grinding traces, scratches, oxidation or corrosion marks are not allowed.

CF flanges with a Brinell hardness of 170 to 300 in the range of the sealing knife edge must be used. The flanges are sealed by OFHC copper gaskets with a HV hardness of 50-85 ±8.5 kp.mm-2.

The screws used for UHV assemblies shall be vented and silver plated.

The surface finish of Flat Seal Flanges should be N4.

The contractor/supplier has to include a reasonable fraction of rotatable flanges, the position of which has to be agreed upon with the customer during preliminary inspection.

The quality of the welds must be according to the ISO standards: ISO 13919-1, ISO 5817, quality level B: Stringent.

The supplier must qualify the welders for each process according to ISO standards: 9606-1.

22.5 Preliminary Inspection

The contractor/supplier has to submit the following documents for each vacuum component for preliminary inspection prior to the manufacturing of the vacuum system:

- Data sheets with all technical information, e.g., bakeability, leak tightness, technical characteristics etc.
- Calculations
- Cleaning plan.

Procurement has to be started only after inspection and release of the above documents by the customer.

Manufacturing of the vacuum components has to start only after the customer has inspected and approved the above documents.

22.6 Materials

In principle, the materials usually utilized by the respective manufacturer of the components have to be used, provided that they comply with the UHV requirements. The material's compatibility within the vacuum requirements depends on the material's vapour pressure at the operating temperature, permeability for gases and the porosity.

For stainless steel materials forming part of the vacuum chamber walls, the contractor shall supply SESAME with material certificates in accordance with ISO 404 confirming the material specification, chemical analysis and room temperature mechanical properties.

For the absorbers, oxygen-free copper, material no. 2.0040 (OFHC-Cu) according to DIN 1787 (UNS C10200), has to be used. GlidCop dispersion-strengthened copper may also be considered as an option.

22.7 Handling and cleaning

For the assembly to be completely compatible with the UHV environment, a high degree of cleanliness will be necessary at all stages of production to guarantee an acceptably low outgassing rates and weld integrity.

All machining work is to be carefully controlled to ensure that no foreign material is embedded in the surface of the material.

All mechanical cold working operations must exclude the use of heavy organic lubricants since these can be retained to some extent in the surfaces after the process.

During and after final assembly the components must be handled in special clean and dust-free areas only. This especially applies to the final inspection.

Machining coolants shall be water soluble and sulphur free and shall be subject to SESAME approval.

During any unavoidable work on the inner and sealing surfaces of the chambers and when handling the components, wearing of clean, lint-free gloves is required to prevent contamination of the vacuum-facing surfaces.

To prevent re-contamination of the vacuum-facing surfaces by hydrocarbons, only appropriate pumps and leak detectors may to be used for evacuation of the chambers and leak detection. Turbo molecular pumps with hydrocarbon-free pre-pumps are considered suitable.

The plate material is to be cleaned before any cutting or forming operation commences. It will be sufficient to swab with acetone or any similar solvent. If a guillotine or press is to be used, the blades should also be cleaned with this solvent.

The tenderer is requested to submit a detailed description of the proposed cleaning procedure (with the cleaning agents to be used) with the tender.

After cleaning the vacuum surfaces must be protected against accidental contamination.

22.8 Identification

Each component must be provided with a heat-resistant identification at an appropriate and visible point, e.g., on external surfaces of a flange. The identification must contain the following information: Name of the manufacturer, year of manufacture, type of material, serial number.

22.9 Acceptance at the Manufacturer's Workshop

The results from acceptance tests at the manufacturer's workshop have to be documented by the contractor/supplier in a test record. This record is to be added to the documentation.

22.10 Testing, Shipping and Packaging

The sequence of operations for the factory acceptance test on each completed and cleaned component shall be as follows:

- Visual internal and external inspection.
- Vacuum leak test and desorption test after the bakeout of the component up to a temperature compatible of the material treated. A He-leakage rate of $< 1 \cdot 10^{-10}$ mbar.l/s, Visual inspection of the sealing surfaces of flanges immediately prior to protective packing for dispatch.
- Coolant flow tests (for blockage, pressure drop, water leaks…etc.)
- The vacuum components and in particular the flanges and their sealing edges have to be subjected to visual inspection prior to packaging. Any defect on the knife edge of any flange of a vacuum chamber results in rejection of the vacuum component. An inspection record has to be provided.

For shipping, the sealing surfaces of the flanges must be covered by a reliable protection to prevent damage.

For storage and shipping each vacuum chamber must be backed filled with dry pure nitrogen at a slightly above atmospheric pressure, according to the standards of UHV practice.

These tests must be performed, documented and submitted to SESAME for all the components under UHV conditions.

Upon submission of the documentation including the confirmation of the acceptance test at the manufacturer's workshop, the incoming goods will be inspected at the customer's site.

22.11 Leak Tightness

The ultra-high vacuum components have to be submitted to an integral leak test using the Helium vacuum leak test method (leak rate <1.10^{-10} mbar.l/s included background). The leak test is to be carried out by spraying all surfaces, welds, and flange seals with helium.

Specific desorption rate < 1*10-12 mbar l/s cm2 after cool down from a 24-hour bake-out at 250°C. (unless otherwise stated elsewhere or agreed in writing).

The leak detection shall be done with a suitable helium leak detector; the roughing system of the leak detector must be composed of dry (oil free) pumps.

In above tests, the sensibility of the measurement setup shall be determined with an external calibration leak.

22.12 RGA Scan Analysis

Test records with RGA scans. In these tests, the sensitivity of the measurement setup must be determined with an external calibration leak. This calibration must be carried by a certificated company.

Total and partial pressure (residual gas analysis RGA from 1-200 AMU) must be performed after cooling down to room temperature from a 24h bake out at the suitable temperature.

The residual gas analysis of each vacuum vessel must show that hydrocarbons contamination defined by the total partial pressure of all masses greater than 28 (with exception of mass 44) is less than 1% of the total pressure